
Masters Theses

Student Theses and Dissertations

2009

Inductance modeling and extraction in EMC applications

Clint Matthew Patton

Follow this and additional works at: https://scholarsmine.mst.edu/masters_theses



Part of the [Electrical and Computer Engineering Commons](#)

Department:

Recommended Citation

Patton, Clint Matthew, "Inductance modeling and extraction in EMC applications" (2009). *Masters Theses*. 5422.

https://scholarsmine.mst.edu/masters_theses/5422

This thesis is brought to you by Scholars' Mine, a service of the Missouri S&T Library and Learning Resources. This work is protected by U. S. Copyright Law. Unauthorized use including reproduction for redistribution requires the permission of the copyright holder. For more information, please contact scholarsmine@mst.edu.

INDUCTANCE MODELING AND EXTRACTION
IN EMC APPLICATIONS

by

CLINT MATTHEW PATTON

A THESIS

Presented to the Faculty of the Graduate School of the
MISSOURI UNIVERSITY OF SCIENCE AND TECHNOLOGY

In Partial Fulfillment of the Requirements for the Degree

MASTER OF SCIENCE IN ELECTRICAL ENGINEERING

2009

Approved by

James Drewniak, Advisor
David Pommerenke
Mehdi Ferdowsi

ABSTRACT

Inductance has become a challenging problem for EMC engineers in many applications. Regardless of the application at hand, the first step remains the same; return to the physics and trace the current paths.

IGBTs have become an important part in the design of power electronics because of their ability to switch fast and with stand high currents. Modules used for three phase motor drives often create problems when neglected parasitic components show themselves and interfere with the performance of the desired operation of a system. Many manufactures of these modules do not give out equivalent circuit modules and therefore leave a black box for this part of the designers schematic used in simulations. When these systems include motors, other problems can arise which may require their own consideration.

Pre-emphasis is a method used to reduce the attenuation of a signal as it travels from one end of a transmission line to another by boosting frequency components of a signal. In order for this method to work, it is important to know how the impedance changes across the board. Working with the capacitances is relatively easy, while revealing the inductance and pin pointing it on the geometry often creates a challenge.

Strong magnetic fields are desired for high energy delivering systems where full-wave modeling plays a crucial role in the design of superior systems. The inductance associated with the geometry must be distributed properly for the development of a system that maximizes the fields. This is accomplished by following the current paths and focusing on the physics involved.

ACKNOWLEDGMENTS

I would like to express my up most gratitude to my advisor, Dr. James Drewniak, for the time he spent developing my skills in EMC applications. From the day I stepped into his office looking for an undergraduate research project, he influenced my decisions and research helping me gain confidence in my knowledge. I am also in debt to Dr. David Pommerenke for the measurement and electronics training I received from him. Although he was very busy, he was always willing to help me with my project. Dr. Jun Fan and Dr. Daryl Beetner were always willing to sacrifice their time to help answer my questions and for that I am grateful.

I am thankful for the students in the lab that helped me with projects. Hemant helped me learn Quartus and Allegro when it would have taken me weeks to do so otherwise. Matteo started teaching me how to use CST Microwave Studio when I was still an undergraduate student. I want to thank the senior design students, Igor, Jason, and Matt, who I mentored and trained as well as the senior design team and Dr. Edward Wheeler from Rose-Hulman. They spent much time working on the Rockwell Automation project which is a major section of my thesis.

I appreciate the funding I received from the Missouri University of Science and Technology EMC Laboratory as a Graduate Research Assistant as well as the funding from the Electrical Engineering Department while serving as a Teacher's Aide.

I must also thank my parents, Rick and Theresa, and my brother, Kevin, for always supporting me while I worked on my degree. I am appreciative of my other relatives and friends who helped me out while living in Rolla. I am in debt to my wife, Amber, who has tolerated my devotion to the lab, classes, and research and has supported me even though much of my time has been given to things other than her.

TABLE OF CONTENTS

	Page
ABSTRACT	iii
ACKNOWLEDGMENTS	iv
LIST OF ILLUSTRATIONS	vii
LIST OF TABLES	xi
SECTION	
1. INTRODUCTION	1
2. PARASITIC COMPONENTS OF IGBT MODULES	3
2.1. INDUCTANCE	4
2.1.1. Inductance Measurements	5
2.1.2. Inductance Simulations	6
2.2. CAPACITANCE	14
2.2.1. Capacitance Measurements	14
2.2.2. Capacitance Simulations	18
3. FBGA PARASITIC INDUCTANCES	21
3.1. IMPEDANCES SEEN AT PORTS ONE AND THREE	23
3.1.1. Measurements	23
3.1.2. Simulations	23
3.1.3. Analytical Calculations	30
3.2. IMPEDANCES SEEN AT PORT TWO	37
3.2.1. Simulations	37
3.2.2. Analytical Calculations	37
4. LOCATING PARASITIC CIRCUIT ELEMENTS IN MOTOR DRIVES	39
4.1. CURRENT PROBE EFFECTS ON MEASUREMENTS	39
4.1.1. Copper Strap	39
4.1.2. Current Probe Transfer Impedance	41
4.2. MEASURED IMPEDANCE OF MOTOR DRIVE TO CABLES	44
4.2.1. Measurements Performed from Inside IGBT	45
4.2.2. Input Impedance Looking into the IGBT Module	48
4.2.3. IGBT Module to Cable Transfer Impedance	48
4.2.4. Transfer Impedance Outside the IGBT Module	49
5. ENERGY DELIVERING SYSTEMS	54

5.1. PROTOTYPE.....	55
5.1.1. Simulations.	55
5.1.2. Manufacturing the Printed Circuit Board.	62
5.2. NEW ONE LAYER DESIGN	63
5.2.1. Changes Made to PCB to Eliminate Electrostatic Discharge.	63
5.2.2. CST Simulations Made for New Design.	65
5.2.3. Current Calculations Performed in Matlab.	68
5.2.4. Manufacturing New PCB Coil Design.	72
APPENDIX.....	74
BIBLIOGRAPHY.....	130
VITA.....	131

LIST OF ILLUSTRATIONS

	Page
Figure 2.1. IGBT Geometry.....	3
Figure 2.2. IGBT Labeled Area Fills.....	4
Figure 2.3. Current Paths for All Three Phases.....	5
Figure 2.4. Current Path of Phase 1.....	6
Figure 2.5. Measurement Setup for Phase One.....	6
Figure 2.6. Simulation Model for Phase One.....	7
Figure 2.7. Phase One Impedance Comparison.....	8
Figure 2.8. Labeled Sections of Simulation Model.....	9
Figure 2.9. Phase One ADS M2 Model.....	9
Figure 2.10. Phase One ADS M2 Model Results.....	9
Figure 2.11. Q3D Model Used to Calculate the Inductance of the Probe.....	10
Figure 2.12. Q3D Model Used to Calculate the Inductance of Two Bond Wires.....	11
Figure 2.13. Q3D Model Used to Calculate the Inductance of Four Bond Wires.....	11
Figure 2.14. Q3D Model for Self Inductance Calculation of Area Fill A.....	12
Figure 2.15. ADS Model Using Q3D Calculated Values.....	13
Figure 2.16. Comparison of ADS Results and Measured Values.....	13
Figure 2.17. Substrate Capacitance Measurement Setup for Center Conductor Connection.....	14
Figure 2.18. Substrate Capacitance Measurement Setup for Outer Conductor Connection.....	15
Figure 2.19. Substrate Capacitance Measurement Results.....	15
Figure 2.20. Substrate Dimensions.....	16
Figure 2.21. The Bond Wires were Removed from the IGBT Module to Measure the Capacitance of the Major Area Fills.....	16
Figure 2.22. Measurement Setup for Area Fill B Capacitance.....	17
Figure 2.23. Measurement Results for Area Fill B Impedance.....	17
Figure 2.24. CST Model for Area Fill B.....	19
Figure 2.25. CST Simulation Results for the Input Impedance at Port One.....	19
Figure 2.26. Q3D Capacitance Simulation Model.....	20
Figure 3.1. Geometry of FBGA Test Board.....	22
Figure 3.2. Dimensions and Placement for Measurements and Simulations.....	22

Figure 3.3. Altera Stratix II PCB Stack-Up	24
Figure 3.4. ADS Simulation for No Power Supplied to Board.....	26
Figure 3.5. Magnitude of the Input Impedance at Port 1	26
Figure 3.6. Magnitude of the Transfer Impedance Between Ports 1 and 3	27
Figure 3.7. Magnitude of the Input Impedance at Port 3	27
Figure 3.8. ADS Model.....	28
Figure 3.9. Magnitude of Z_{13} ADS and EzPP Simulation Results vs. Measurements.....	29
Figure 3.10. Initial Schematic Used for Analytical Calculations	30
Figure 3.11. Simplified Circuit for Z_{13} Calculations	31
Figure 3.12. Z_{13} Magnitude Comparison	32
Figure 3.13. Schematic Including Higher Mode Inductance Used in Analytical Calculations.....	33
Figure 3.14. Z_{13} Magnitude Comparison with Higher Mode Inductance Added into the Model	33
Figure 3.15. Schematic Including Higher Mode Inductance and Parallel Resistance	34
Figure 3.16. Z_{13} Magnitude Comparison with Higher Mode Inductance and Parallel Resistance Added into the Model	34
Figure 3.17. Input Impedance for Port 1	36
Figure 3.18. Input Impedance Seen at Port 3.....	36
Figure 3.19. ADS Simulation Results for Port Two Impedances	37
Figure 4.1. Copper Strap.....	40
Figure 4.2. Copper Strap Wrapped in Electrical Tape.....	40
Figure 4.3. Input Impedance of Current Strap	41
Figure 4.4. Equivalent Circuit Model for Transfer Impedance Measurement Setup.....	41
Figure 4.5. Current Probe Transfer Impedance Measurement Setup.....	42
Figure 4.6. Transfer Impedance of the Three Current Probes Tested.....	43
Figure 4.7. Manufacture's Transfer Impedance Plot for the F-61	43
Figure 4.8. Manufacture's Transfer Impedance Plot for the F-62.....	44
Figure 4.9. Manufacture's Transfer Impedance Plot for the F-65.....	44
Figure 4.10. IGBT Schematic	45
Figure 4.11. IGBT Pin and Component Locations	45
Figure 4.12. Probe Connection Across IGBT Shown on the Schematic	46
Figure 4.13. Probe Connection to IGBT Module	47
Figure 4.14. Setup for Transfer Impedance from IGBT to Cables Leading to the Motor.....	47
Figure 4.15. Input Impedance Seen from Inside the IGBT.....	48

Figure 4.16. Transfer Impedance from IGBT to Cables	49
Figure 4.17. Copper Triangle Used to Connect the Center Conductor to the Three Phases and Reduce Inductance	50
Figure 4.18. Copper Tape Was Used for Connection of Outer Conductor of the Probe to the Heat Sink	51
Figure 4.19. Measurement Setup for the Impedance Measured Outside the IGBT Module	51
Figure 4.20. Transfer Impedance Magnitude Taken Outside of the IGBT Module	52
Figure 4.21. Transfer Impedance Phase Taken Outside of the IGBT Module	53
Figure 5.1. CST Model Used for Single Layer of Serpentine Coil.....	55
Figure 5.2. CST Model Used for Two Layers of Serpentine Coils	56
Figure 5.3. CST Model Using Two Coil Layers and Larger Vias	57
Figure 5.4. Two Layer Model's Magnetic Fields Seen with a Cut Plane Placed in Model.....	58
Figure 5.5. Two Layer Model's Magnetic Fields Seen at an Inch Away from the Coils.....	59
Figure 5.6. One Layer Model's Magnetic Fields Seen from an Inch Away from the Coils.....	59
Figure 5.7. PSPICE Model.....	60
Figure 5.8. PSPICE Results for Two Coils Comparing the Values of C1 and L1 Over Time.....	61
Figure 5.9. Comparison for One and Two Layers of Coils	61
Figure 5.10. Back Side of Manufactured PCB	62
Figure 5.11. Front Side of Manufactured PCB	63
Figure 5.12. Change in Model without the Turn of 90 degrees	64
Figure 5.13. Solution to the Electrostatic Discharge Problem from the Power Connection to the Return Trace	64
Figure 5.14. Return Trace Changes	65
Figure 5.15. CST Model Used for Simulation of New Design.....	66
Figure 5.16. Modified Coils Field Distribution at an Inch Away from Coils with 240 mil Separation Between Coils and Return Plane	66
Figure 5.17. H-field Distribution at an Inch Away from Coils with a Separation of $\frac{3}{4}$ of an Inch Between Layers	67
Figure 5.18. H-field Distribution at an Inch Away from Coils with a Separation of an Inch Between Layers.....	68
Figure 5.19. Equivalent Circuit.....	68
Figure 5.20. Current Through Coils vs. Time.....	70

Figure 5.21. Current Through Coils vs. Frequency70
Figure 5.22. New PCB Design.....73
Figure 5.23. New Setup73

LIST OF TABLES

	Page
Table 2.1. Self and Mutual Inductance Results for Phase One.....	11
Table 2.2. Simulation and Measurement Results.....	18
Table 2.3. Q3D Calculated Capacitances in pF.....	20
Table 3.1. TM_z Modes	25

1. INTRODUCTION

Today's world is driven by the fastest and smallest electronics. Therefore, the market is in the hands of the designers who can not only meet these requirements, but surpass the rest of their competitors at the lowest cost. Many limits face engineers when designing such a system, such as current, power, and heat dissipation. This thesis digs into the challenges seen when dealing with high currents and power. It is broke up into four different sections along with an appendix. However, it focuses in on three major areas; motor drives, FBGA package parasitics, and high energy delivering coil development.

Motor drives designed with IGBTs may operate with a switching speed up to around 30 kHz and support large currents of 200 to 1000 A. Switching speeds at low frequencies while driving large amounts of current makes these systems not only involve the drive but the motor and cable as well. A senior design project evolved and three students attending Missouri Science and Technology worked with four senior design students at Rose-Hulman Institute of Technology. The project was broke into two teams where two students from each school worked on characterizing the IGBTs inside the motor drive, while one student from Missouri Science and Technology and two students from Rose-Hulman worked with the motor and cables. As a mentor to the students, I helped them with measurements, simulations, and calculations. The students were required to include all of their findings in a report for Rockwell Automation. This report has been added to this thesis as an appendix. Section 2 shows much of the IGBT modeling and measurements, while the appendix shows some extra parts dealing with the IGBT and all of the motor and cable documentation. Section 4 deals with a larger motor drive from the same company having similar problems and was analyzed using the same setup for the motor and cables. When analyzing devices with large currents, the first step is to trace all the current paths. The current being transferred from the drive to the cables becomes the concern. In the process of analyzing these currents, current probes were used. Characterizing current probes and the effect they have on measurements proved to be a large part of this project and is also shown in detail in Section 4.

Although negligible in previous generations of products, these parasitic elements become an issue when increasing the speed of operation and decreasing the size. A PCB with crowded traces on each layer requires designers who optimize the performance of the device to call upon special tricks and techniques. Operating at frequencies which impose substantial dispersion on a signal may be corrected by applying pre-emphasis on the signal. This method involves boosting those frequency components that are attenuated by the transmission line. Understanding the impedance the signal encounters as it travels across the board is an important part of this method. Section 3 discusses the measurements, simulations, and analytical calculations involved when finding these impedances.

The ability to transfer large amounts of energy between systems has been around for many years. Although most of these devices are large and bulky, the design analyzed and constructed in this thesis is all about size, weight, and performance. Section 5 discusses how to achieve large amounts of magnetic fields transferred to other devices while keeping the coils light weight and small. Dealing with these high currents and voltages generate other problems which are not as much of a concern when dealing with low voltage circuits, such as Electrostatic Discharge (ESD). However, the physics remains the same and is the driving point of this subject just as it is with the other subjects discussed in this thesis.

2. PARASITIC COMPONENTS OF IGBT MODULES

Insulated Gate Bipolar-junction Transistors (IGBT) are used much of the time in power electronic circuits for motor controls, because they can with stand large currents. Changing the frequency these IGBTs switch and the amplitude of the input signal allows the circuit to control the motor. The module's inductance and capacitance was examined to see what effect it played in the overall impedance of the motor drive, since it was reported by users that the drive radiated emissions around 30 MHz. The IGBT module studied was used in a three phase motor drive and is shown in Figure 2.1. To eliminate confusion and keep organization, the larger copper area fill of the IGBT were assigned a letter.

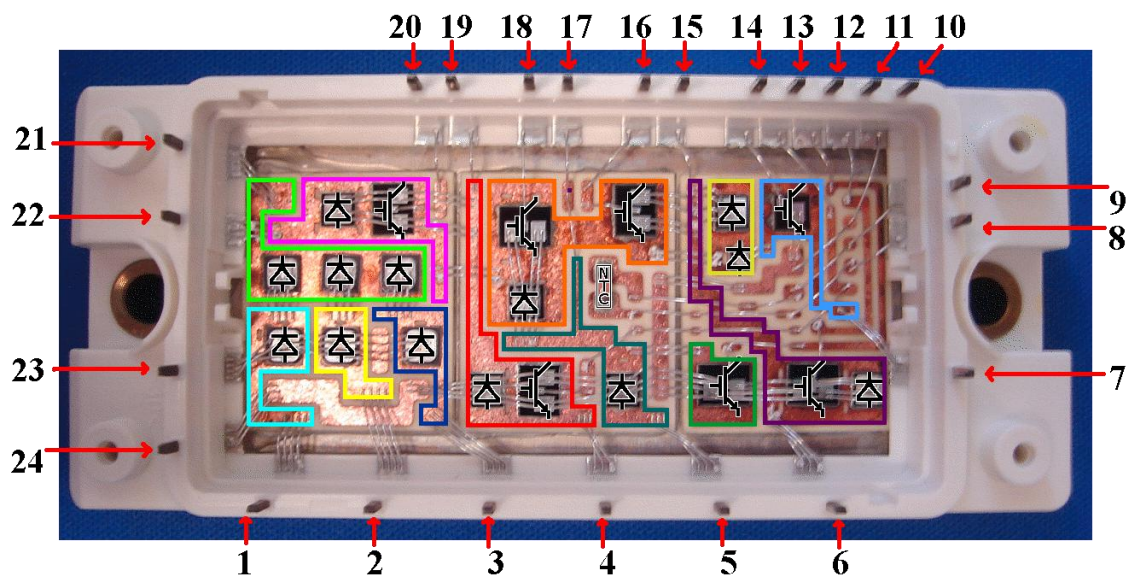


Figure 2.1. IGBT Geometry

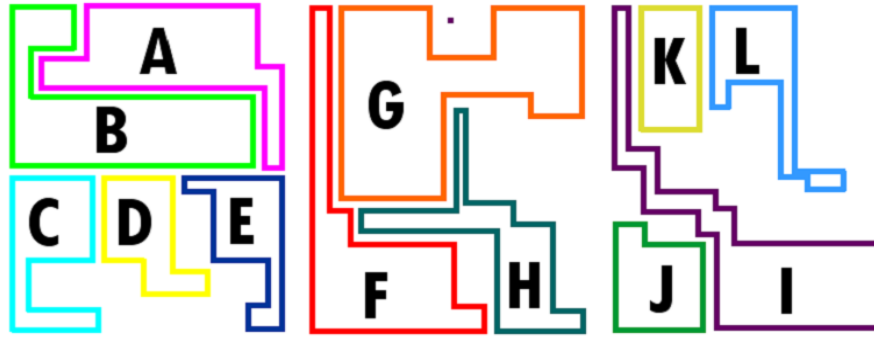


Figure 2.2. IGBT Labeled Area Fills

2.1. INDUCTANCE

Inductance shows up all over the IGBT module expressing itself as self and mutual inductance. For a complete circuit model of the IGBT module, both of these must be examined. Self inductance is defined in equation 1 as the ratio of the magnetic flux linkage to the current flowing through the geometry. The magnetic flux linkage for one loop is expressed in equation 2

$$L = \frac{\Phi}{I} \quad (1)$$

$$\Phi = \int_S \mathbf{B} \cdot d\mathbf{s} \quad (2)$$

Current paths are the sole key to finding the parasitic inductances buried in this module. Therefore, each possible path had to be traced and shown in Figure 2.3. The actual value for the total inductance of each path is obtainable only by measurements, but would prove to be difficult when trying to split up all of the self and mutual inductances of the module. Therefore, simulations were also performed. Each path was modeled in a full-wave simulation tool, and the simulation results were compared to measured results. Once these results matched, the model was able to be broke apart to find self and mutual inductances of the bond wires and area fills. The calculated inductance values gained from simulating parts of the model were used to create an equivalent circuit model.

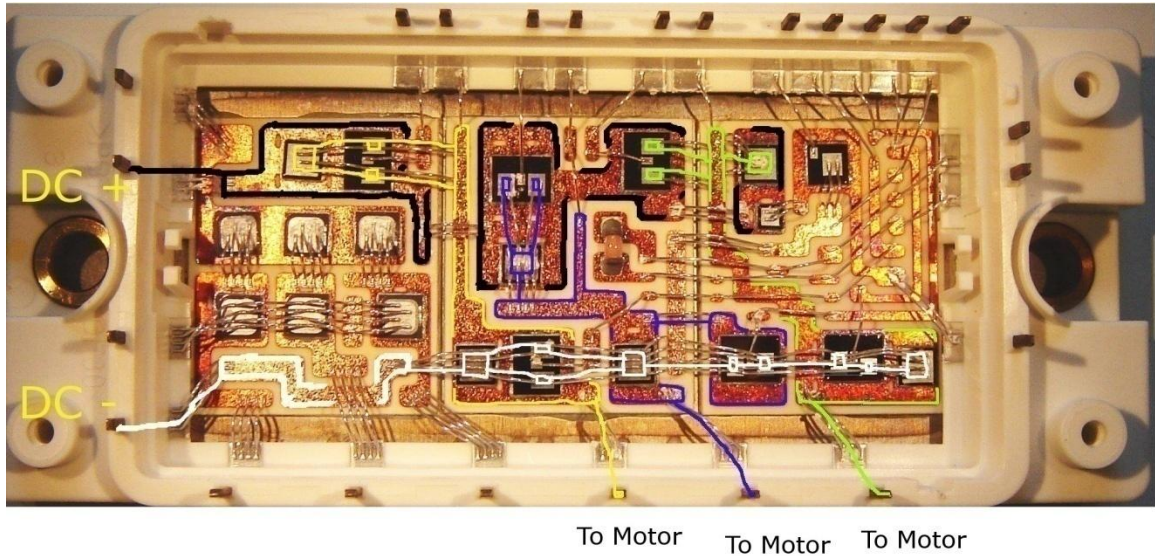


Figure 2.3. Current Paths for All Three Phases

2.1.1. Inductance Measurements. The first path analyzed was phase one whose current path is shown in Figure 2.4. The measurement was performed using a semi-rigid coaxial probe. The outer shield of the coax was soldered to the heat sink, and the center conductor was soldered to the location where the DC rail connected to area fill A from pin 22. This was the input of the intended current path of phase one. Bond wires that were not part of this phase leg were removed. Where the intentional current path of phase one would exit to the motor through bond wires from area fill I to pin six, a strap of copper tape was used to short area fill I to the heat sink as shown in Figure 2.5. The measurement was taken with a Vector Network Analyzer (VNA) to obtain scattering parameters. The impedance for this path was found by using equation 3.

$$Z_{11} = Z_0 \frac{(1+S_{11})}{(1-S_{11})} \quad (3)$$

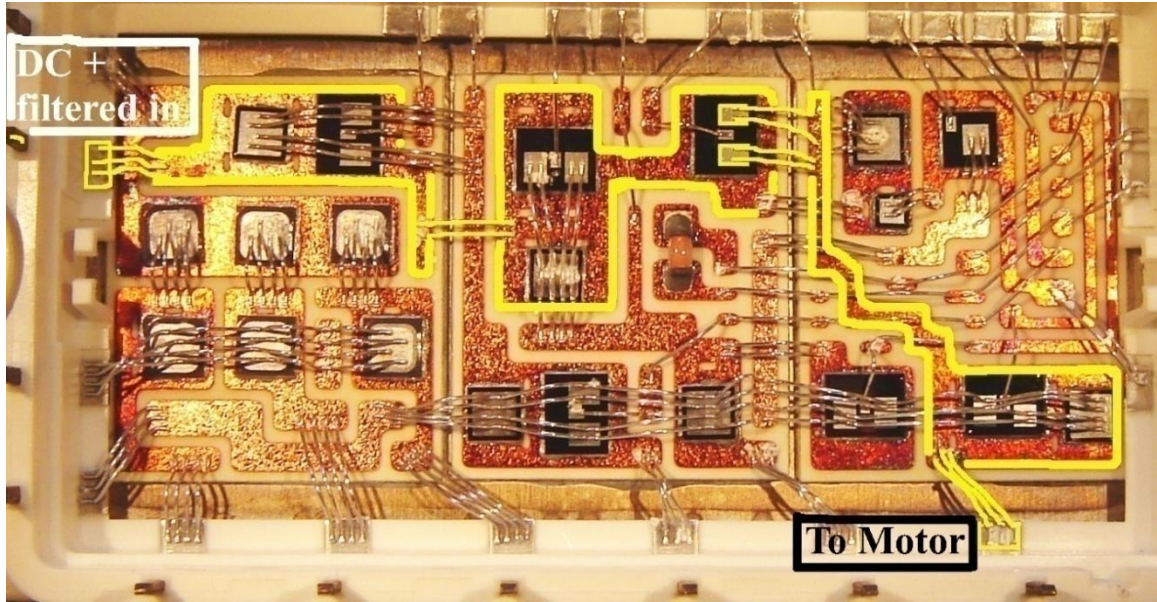


Figure 2.4. Current Path of Phase 1



Figure 2.5. Measurement Setup for Phase One

2.1.2. Inductance Simulations. Simulations were performed to validate the measurements. These simulations were completed using the two full-wave modeling tools CST Microwave Studio and Ansoft's Q3D. While Microwave Studio calculates the field distributions and the impedance associated with the module, Q3D calculates the inductance, resistance, and capacitance matrices needed to generate a SPICE model. The Microwave Studio and Q3D model created is shown in Figure 2.6.

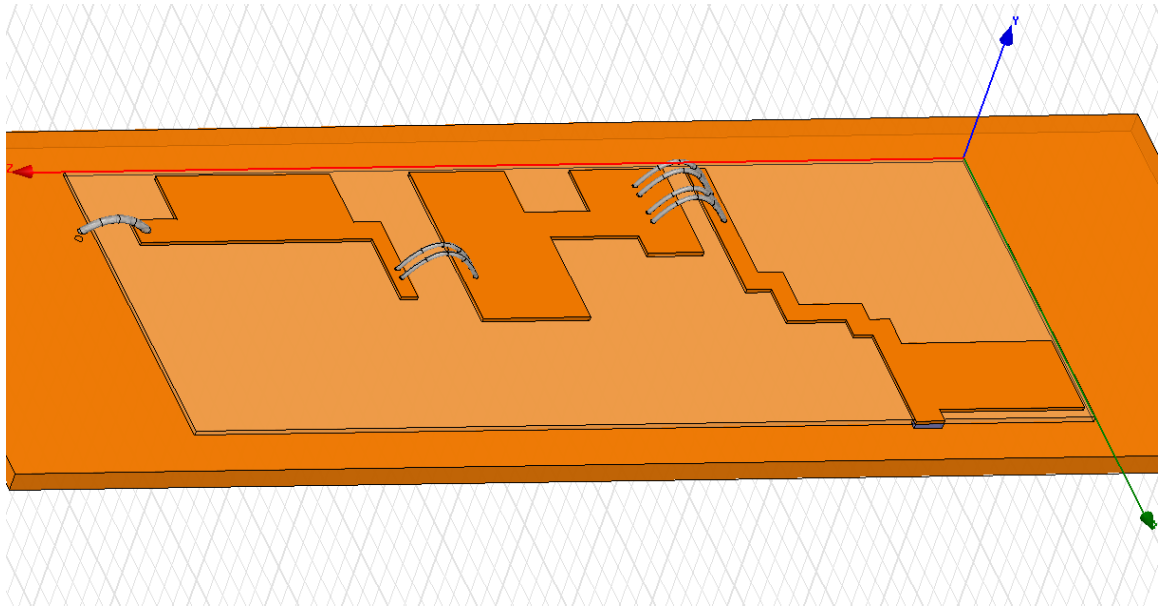


Figure 2.6. Simulation Model for Phase One

The model contained both the short on area fill I and the probe wire on area fill A. The short was placed on area fill I, because this is where the current left the IGBT. To setup the simulation in Q3D, a source was added to the bottom of the probe wire and the sink was placed below it. The placement of the port was based on the way the measurements were performed. The calibration plane of the VNA was at the point where the outer shield of the probe was stripped and the center conductor was left exposed.

For the CST Microwave Studio model, a discrete port was placed between the center of the probe wire and the heat sink. Microwave Studio calculated the input impedance of the loop which was compared to the measurements. This comparison is shown in Figure 2.7. From the input impedance, the total inductance of phase one can be found. The slope of the input impedance magnitude at low frequencies in Figure 2.8 is 20 dB per decade and the phase is negative 90 degrees. These are classic characteristics of an inductor. Therefore, we can find the total inductance of phase one using equation 4.

$$Z_{in} = j\omega L \quad (4)$$

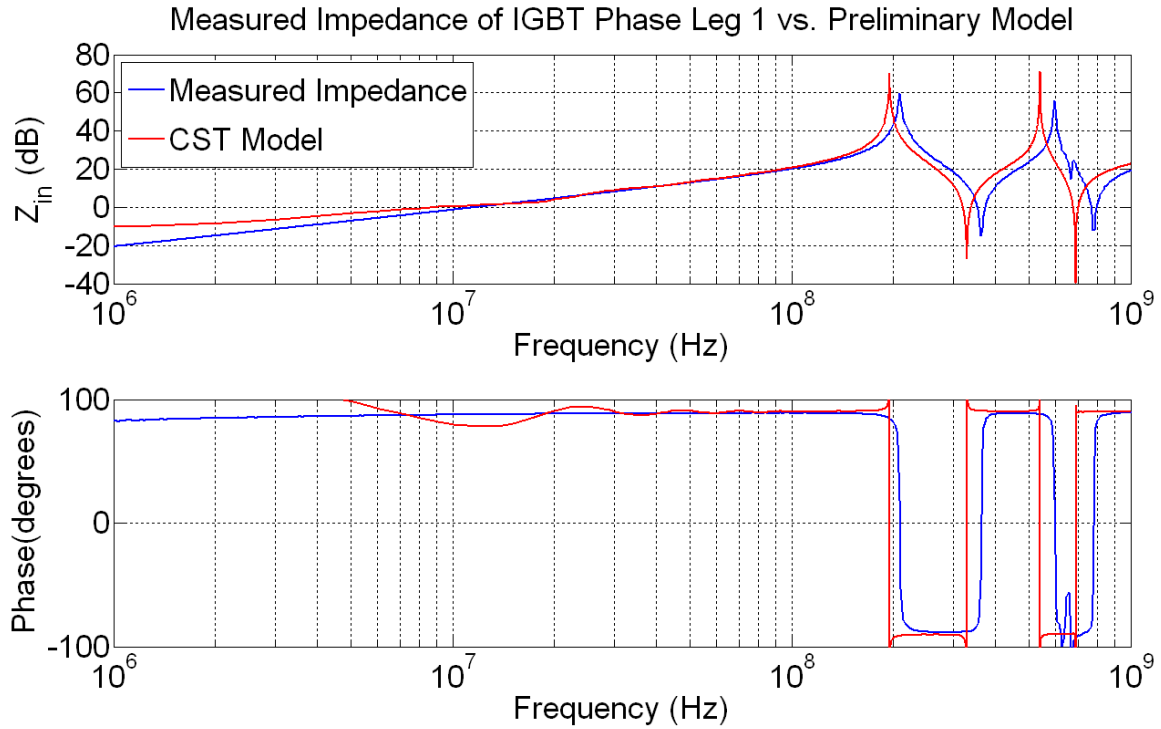


Figure 2.7. Phase One Impedance Comparison

The measurement for the total inductance was performed relatively smooth, but measurements for each individual inductance in the phase would prove to be complicated. However, taking advantage of numerical modeling would create a window of opportunity when facing this obstacle. The phase leg was split into many sections. Each area fill, group of bond wires, and probe wire was simulated separately. Figure 2.8 shows the labeling for the different sections simulated. The inductance values were pulled from these simulations and placed into the ADS model shown in Figure 2.9. The simulation results from the equivalent circuit model are shown in Figure 2.10.

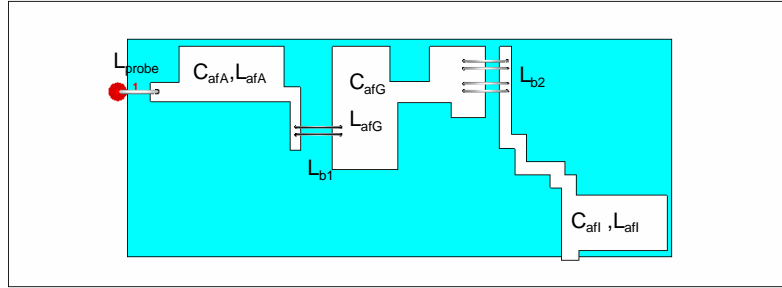


Figure 2.8. Labeled Sections of Simulation Model

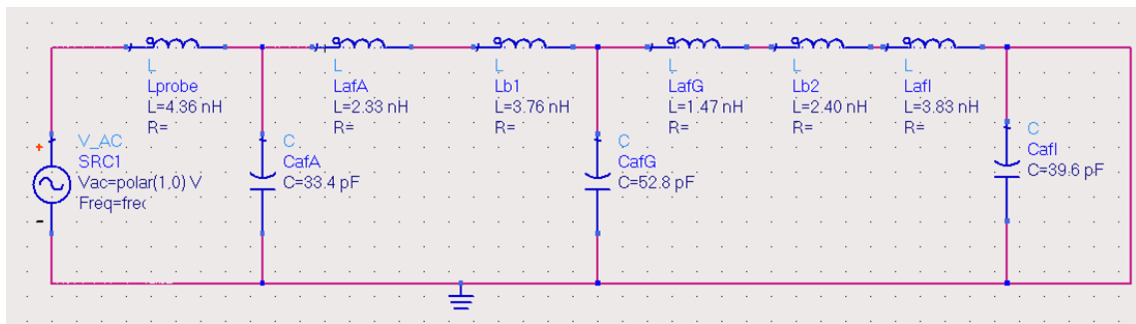


Figure 2.9. Phase One ADS M2 Model

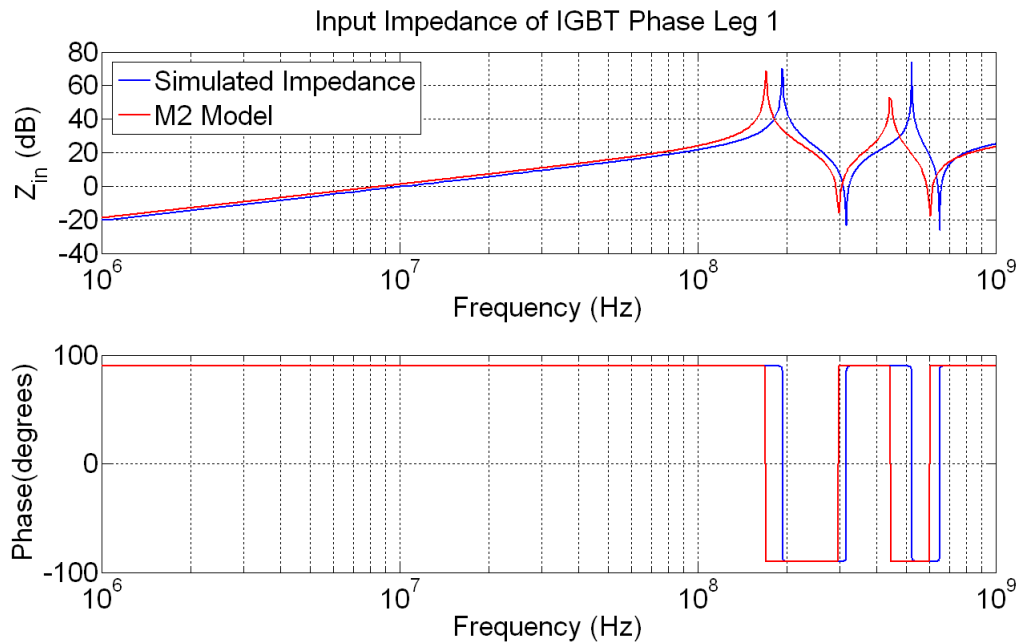


Figure 2.10. Phase One ADS M2 Model Results

As the plots show, the CST and ADS simulation results are starting to match up relatively close. However, the ADS model is still missing the mutual inductances which are difficult to find using Microwave Studio. As shown before, Microwave Studio can be used to find the self inductances of a structure, yet when it comes to finding mutual inductances other simulation programs should be used.

To find the mutual inductance, Ansoft's tool Q3D was used. Q3D was used find the unknown mutual inductances as well as check some of the previous Microwave Studio results. To calculate the mutual inductances, the current path was broken apart. For the probe, the geometry is shown in Figure 2.11. The source was assigned to the circular face at the start of the probe wire, while the other end of the probe wire connected to a block which acted as a short to the heat sink. The sink consisted of a circular sheet positioned on the heat sink directly below the source.

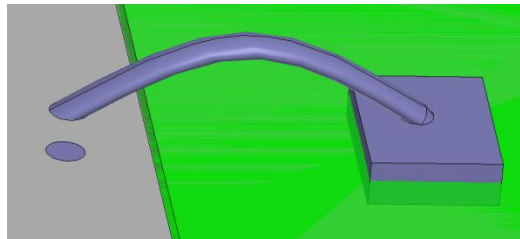


Figure 2.11. Q3D Model Used to Calculate the Inductance of the Probe

A similar simulation was created for the two bond wires connecting area fill A and area fill G. A source was placed at the start of each bond wire and a short was placed at the end of the bond wires. A sink was placed below the bond wires by placing a rectangular sheet on top of the heat sink. Figure 2.12 shows this model. For the four bond wires between area fill G and area fill I, a simulation like the previous simulations was created. Figure 2.13 shows this model. These simulations calculated the self and mutual inductance associated with the bond wires, and the values are recorded in Table 2.1.

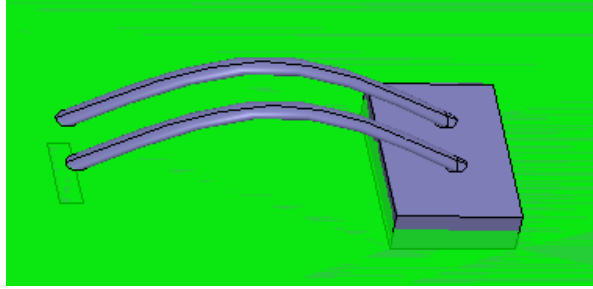


Figure 2.12. Q3D Model Used to Calculate the Inductance of Two Bond Wires

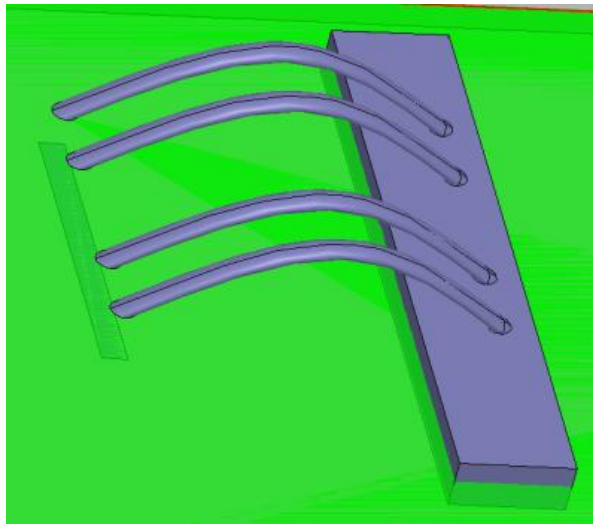


Figure 2.13. Q3D Model Used to Calculate the Inductance of Four Bond Wires

Table 2.1. Self and Mutual Inductance Results for Phase One

Bond Wire	Probe	1	2	3	4	5	6
Probe	2.4681	-	-	-	-	-	-
1	-	4.6245	1.9832	-	-	-	-
2	-	1.8932	4.6559	-	-	-	-
3	-	-	-	2.9482	0.99674	0.25004	0.13747
4	-	-	-	0.99674	2.9094	0.4542	0.2552
5	-	-	-	0.25004	0.4542	2.9131	1.0001
6	-	-	-	0.13747	0.2552	1.0001	2.9496

The next step was to find the self inductance of each area fill. These inductances were found the same way. The source was placed on top of the area fill where the probe wire connected. The short was on the other end where the bond wires left the area fill. The sink was placed below the source on top of the heat sink as portrayed in Figure 2.14.

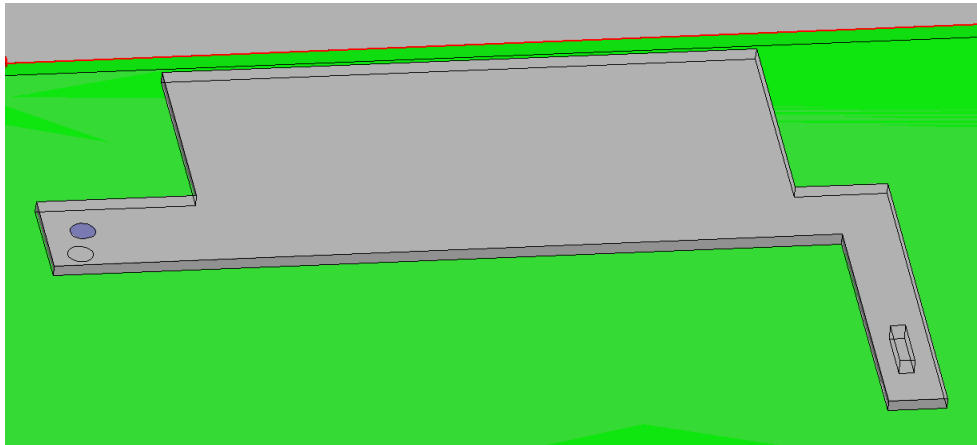


Figure 2.14. Q3D Model for Self Inductance Calculation of Area Fill A

The other area fills were calculated using the same procedure. The method for building these simulations included putting the source where the current enters the area fill, a short where the current leaves the area fill, and the sink where the current path returns to the source.

After these values were found, they were all entered it the ADS model shown in Figure 2.15. The results of the new ADS model compared to the measured data are shown in Figure 2.16.

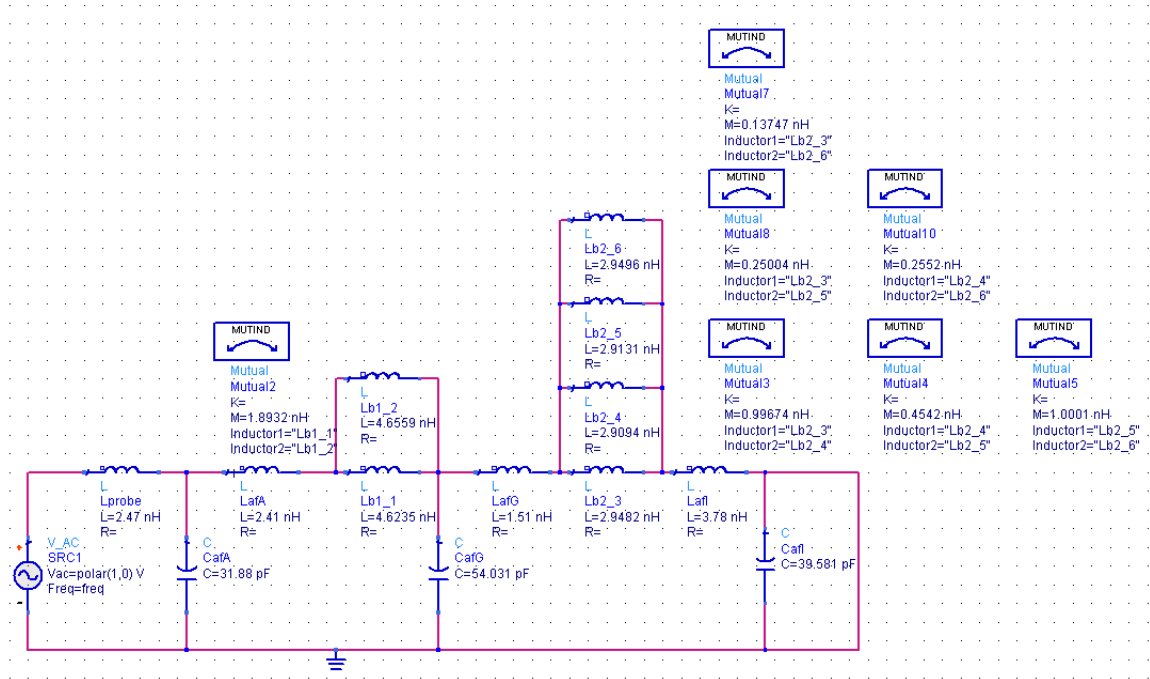


Figure 2.15. ADS Model Using Q3D Calculated Values

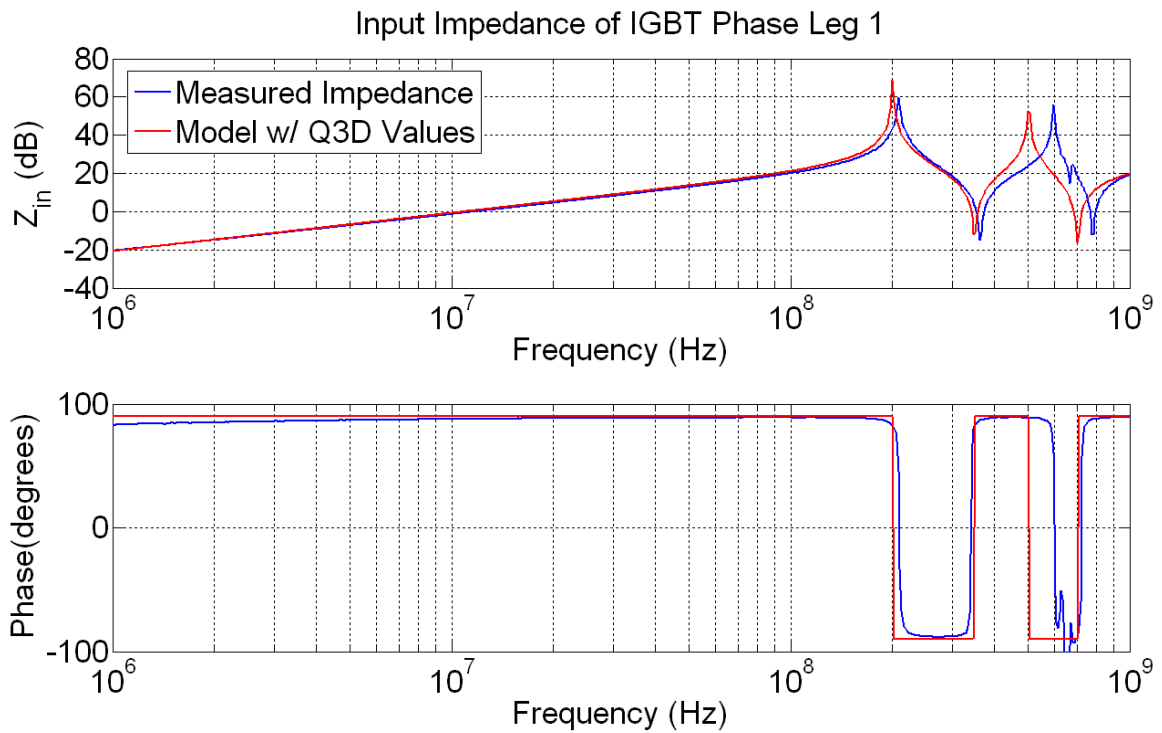


Figure 2.16. Comparison of ADS Results and Measured Values

2.2. CAPACITANCE

2.2.1. Capacitance Measurements. The three capacitances for the IGBT modules are the junction capacitance, plate to plate capacitance, and the plate to reference capacitance. The junction capacitance was neglected, because its size is relatively smaller than that of the plate to reference and plate to plate capacitance. Therefore, the two examined were the plate to plate and plate to reference. Measurements would also have to be performed on the substrate to find the dielectric constant. This is a fundamental element in obtaining accurate simulations which could be compared to the measurements. After finding the dielectric constant, it would be entered into the full-wave simulation tool.

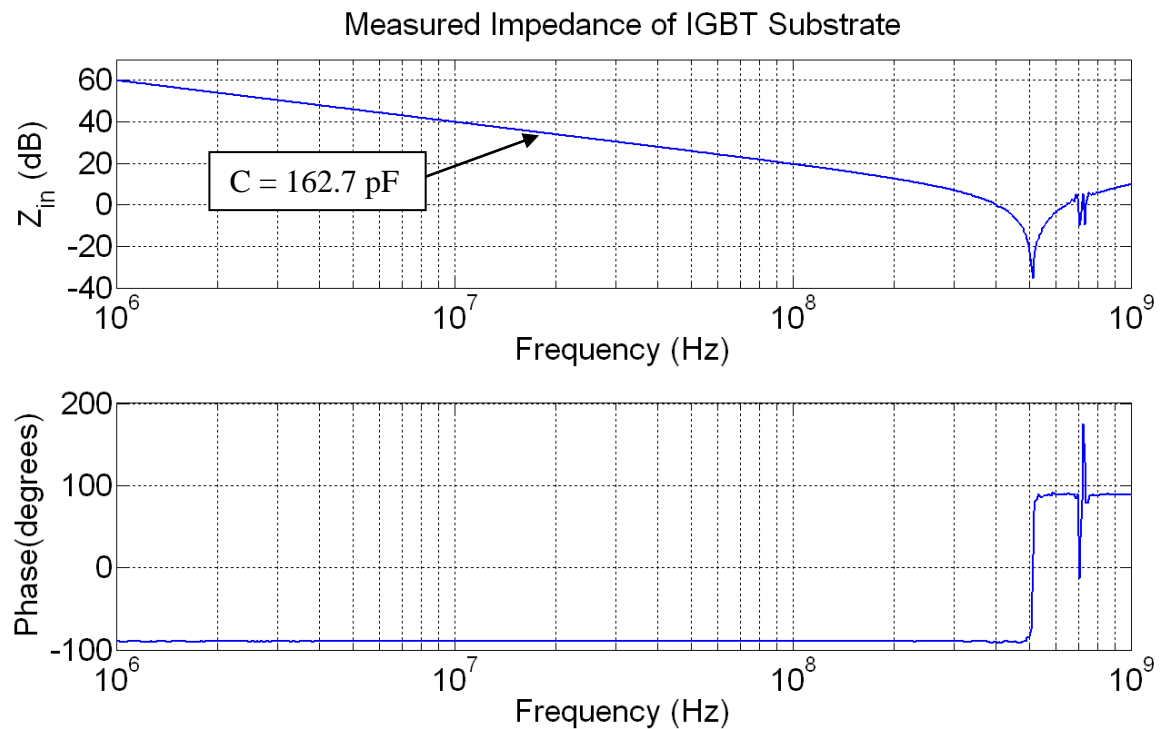
In order to find the dielectric constant, the components and copper area fills were removed from a piece of the substrate on the module using a Dremel tool. The substrate was then removed from the modules heat sink by heating the heat sink on a hot plate and lifting the substrate off. After the substrate was cleaned off and removed from the module, copper was sputtered on it. A utility knife was used to scratch the copper off of the edges, so the edges did not contain a short from the top plane to the bottom plane. This measurement was performed by using a semi-ridged coaxial probe where the center conductor was connected to one side, and the outer conductor was connected to the other side by soldering a copper strap from the outer conductor to the copper plane as shown in Figure 2.17 and Figure 2.18. The measurements are portrayed in Figure 2.19.



Figure 2.17. Substrate Capacitance Measurement Setup for Center Conductor Connection



Figure 2.18. Substrate Capacitance Measurement Setup for Outer Conductor Connection



By knowing the capacitance, the value for the relative permittivity can be found. The area of the copper sputtered substrate was calculated to be $672.5 \mu\text{m}^2$ by using the dimensions shown in Figure 2.20. The thickness of the substrate was measured to be 0.392 mm. The capacitance measured with the Impedance Analyzer was 162.7 pF. Therefore, the relative Permittivity was calculated using equation 5 to be 10.7. Where A is the area of the plane, d is the distance between the two planes, ϵ_0 is the permittivity, and ϵ_r is the relative permittivity or dielectric constant.

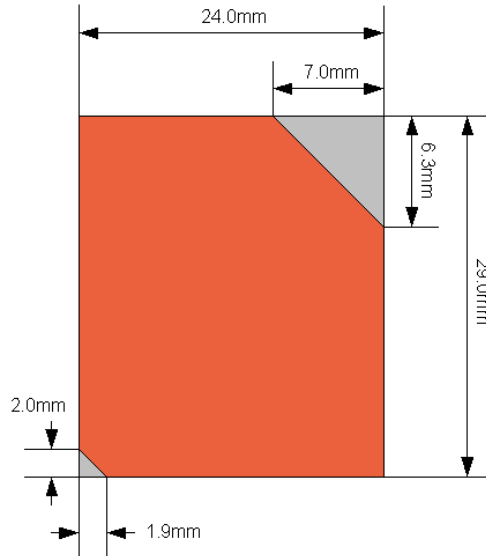


Figure 2.20. Substrate Dimensions

$$\frac{\epsilon A}{d} = \frac{\epsilon_0 \epsilon_r A}{d} \quad (5)$$

The calculated value of ϵ_r is close yet was not easily found, since the thickness of the substrate was hard to measure. Because the dielectric constant depends greatly on the thickness, the simulation values may contain error.

Measuring the plate to reference capacitance required removing all the bond wires connected to the area fill, so all that was left was the area fill of copper above the heat sink as shown in Figure 2.21.

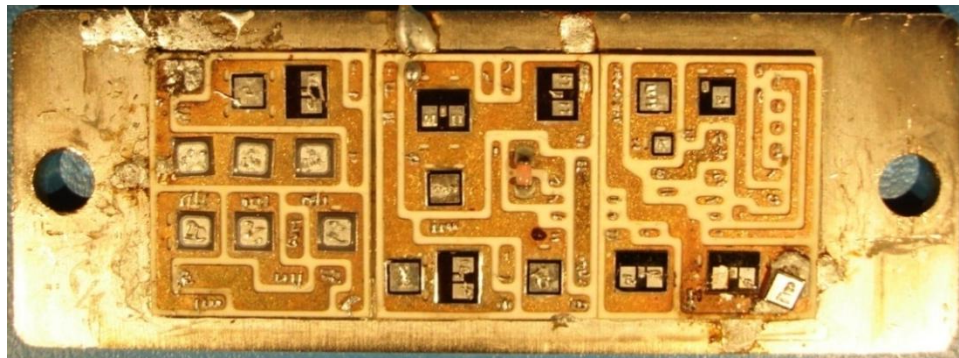


Figure 2.21. The Bond Wires were Removed from the IGBT Module to Measure the Capacitance of the Major Area Fills

The measurement setup consisted of the outer shield of a coaxial probe soldered to the heat sink and the center conductor soldered to the copper area fill. The setup is shown below in Figure 2.22, and the impedance measured using the Impedance Analyzer is shown in Figure 2.23.



Figure 2.22. Measurement Setup for Area Fill B Capacitance

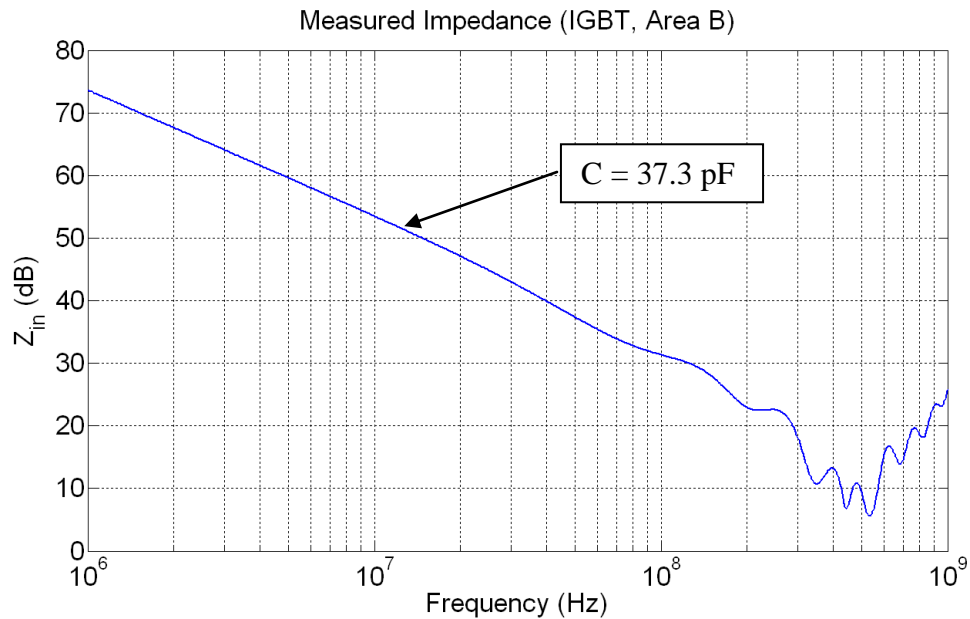


Figure 2.23. Measurement Results for Area Fill B Impedance

Measurements were performed on area fills A, B, G, and I. These measurements were also performed using a LCR meter for comparison. For the LCR measurements, one terminal was clipped to the heat sink, while the other terminal was used to touch each area fill directly. The measured capacitance values for the area fills found by the Impedance Analyzer and LCR meter are shown in Table 2.2.

2.2.2. Capacitance Simulations. Capacitance simulations were performed using both CST and Q3D. CST models were created neglecting the plate to plate and only considered the plate to reference capacitance for each area fill. Figure 2.24 shows the CST model for area fill B and Figure 2.25 shows the results of the simulation. The effects of these adjacent area fills were examined using Q3D. Simulations were generated for each area fill in phase one. These values are shown in Table 2.2.

Table 2.2. Simulation and Measurement Results

	CST	Impedance Analyzer	LCR Meter
Area A	35.4 pF	33.4 pF	-
Area B	40.0 pF	37.3 pF	38 pF
Area G	58.7 pF	52.8 pF	53 pF
Area I	45.4 pF	39.6 pF	41 pF

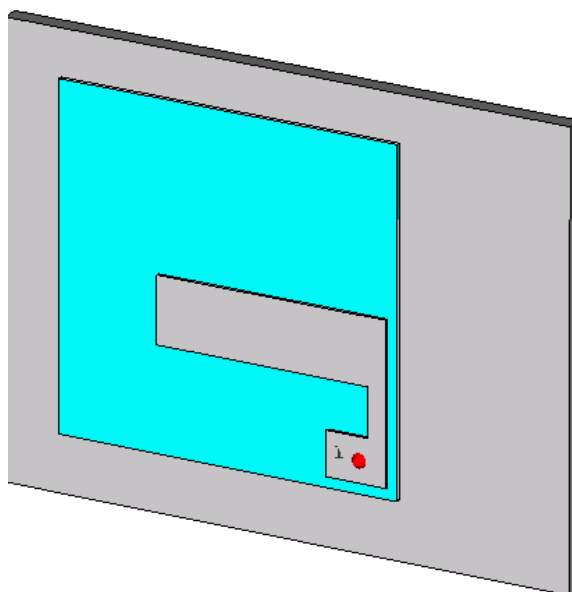


Figure 2.24. CST Model for Area Fill B

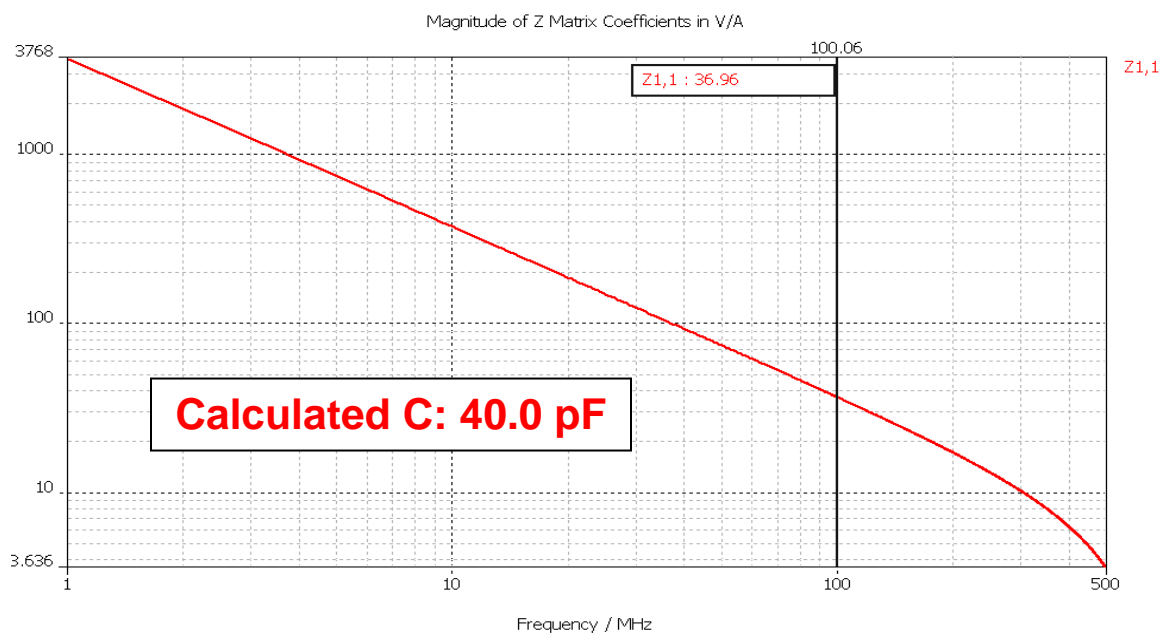


Figure 2.25. CST Simulation Results for the Input Impedance at Port One

The values calculated by CST were used in the ADS model shown in Figure 2.9 and the impedance plot of the ADS and CST simulations are compared in Figure 2.10. Ansoft's Q3D was used to compare with the capacitance simulations generated by CST. When using Q3D to solely find the capacitance and nothing else, there are no sources or

sinks incorporated in the simulation. Each area fill along with the heat sink was put into their individual net, and the simulation was then setup to find only capacitance. The model is shown in Figure 2.26 and included area fill A, G, and I. Unlike CST, Q3D finds the self and mutual capacitance values and places those values into a matrix. The calculated capacitances are shown in Table 2.3.

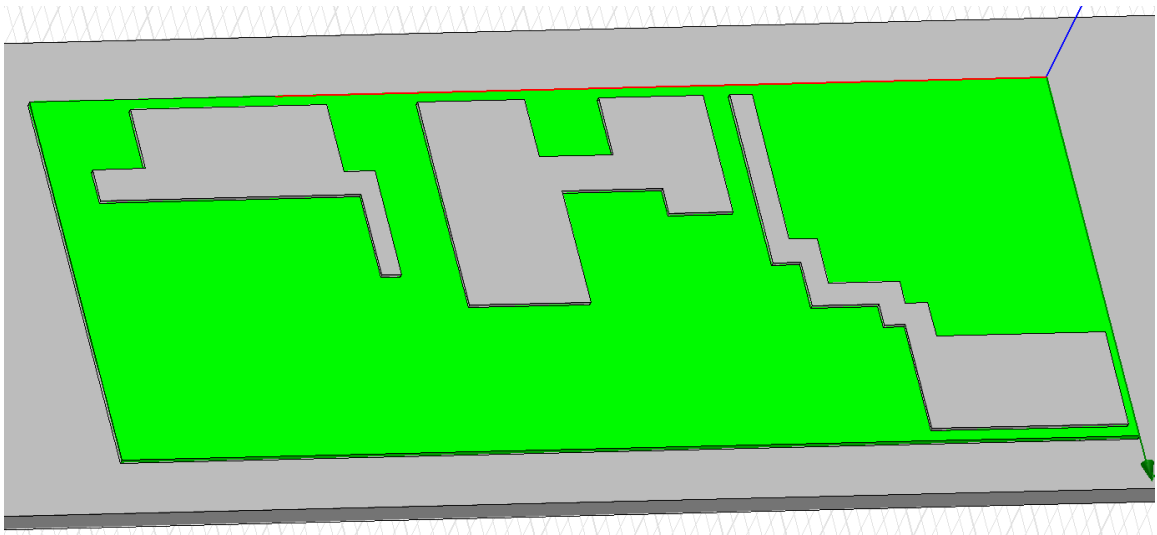


Figure 2.26. Q3D Capacitance Simulation Model

Table 2.3. Q3D Calculated Capacitances in pF

	Area Fill A	Area Fill G	Area Fill I	Heat sink
Area Fill A	-	0.00578	0.00147	31.88
Area Fill G	0.005799	-	0.007563	54.031
Area Fill I	0.00147	0.007563	-	39.581
Heat Sink	31.88	54.031	39.581	-

3. FBGA PARASITIC INDUCTANCES

The Altera Stratix II FineLine Ball-Grid Array (FBGA), along with their program Quartus, can be used together to predict the impedance across the board and add pre-emphasis to the signal leaving the FBGA package. This increases the signal's integrity to the point where it can be read accurately anywhere across the board. Measurements and simulations were made to see the influence the chip had on the impedances seen across the board. The measurements setup for the test board which was analyzed is shown in Figure 3.1, and the dimensions of the board are shown in Figure 3.2. Port 1 was a standard SMA jack, port 2 was an imaginary port placed at the center of the FBGA, and port 3 consisted of a semi-rigid coaxial probe. The outer conductor of the probe was soldered to a surface mount capacitor GND pad, and the center conductor was soldered to the VCCL pad. To find the different impedances seen from port 2 to other areas on the board, ports 1 and 3 were analyzed, since port 2 was inside the FBGA making measurements difficult. Calculations were performed showing that the transfer impedance between port one and three includes all the components that are in the transfer impedances of port two as well as the input impedance. Therefore, having the correct equivalent circuit model for Z_{13} , one can find the impedances seen at port two using the same model.

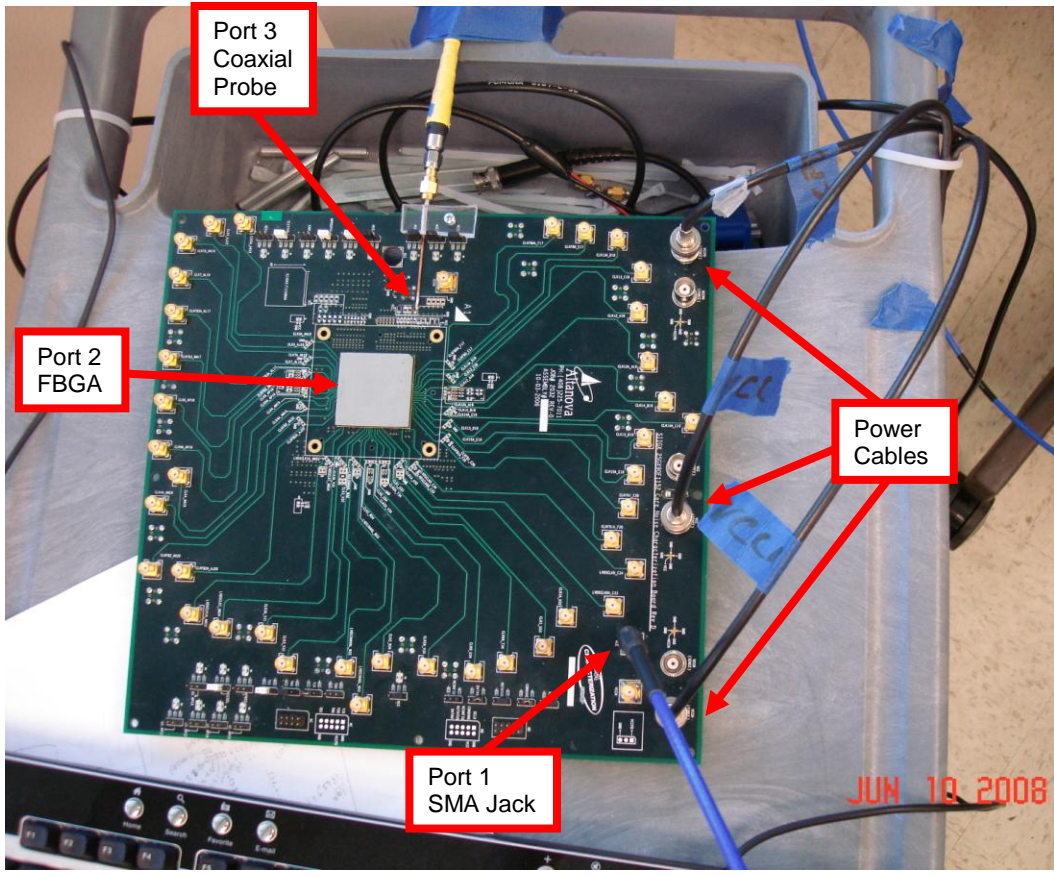


Figure 3.1. Geometry of FBGA Test Board

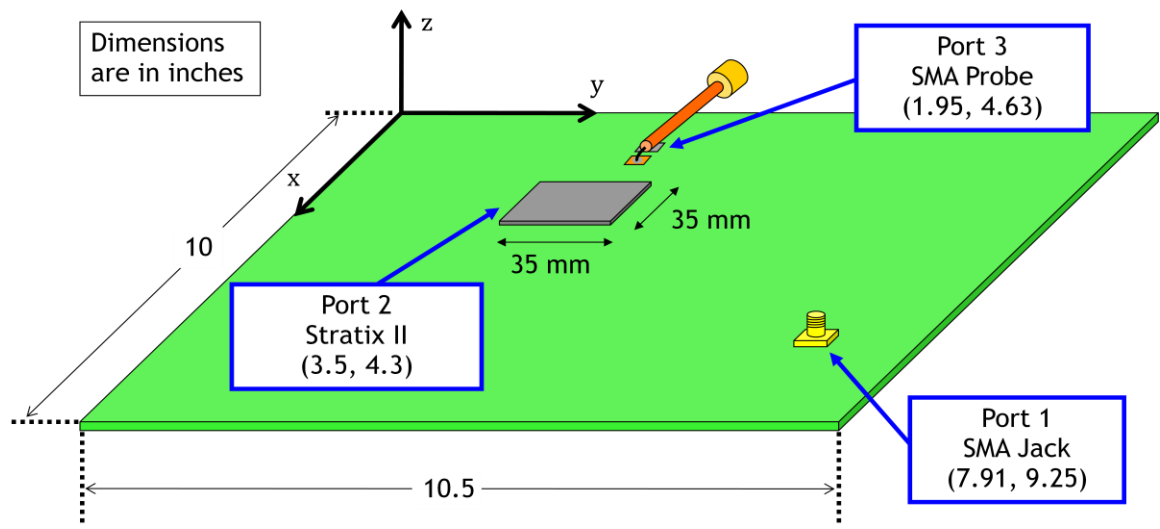


Figure 3.2. Dimensions and Placement for Measurements and Simulations

3.1. IMPEDANCES SEEN AT PORTS ONE AND THREE

3.1.1. Measurements. Scattering parameter measurements were taken at port 1 and 3 using a Vector Network Analyzer and were later converted to Z-parameters. Measurements were made on the board shown in Figure 3.1 which had no capacitors. The VNA was calibrated at port 1 to the tip of the probe where the center conductor was no longer shielded by the outer conductor. Port 3 was calibrated up to the point where the center conductor extrudes out of the SMA jack. Measurements were carried out with the FBGA powered on and off to see how the impedance changed. With no power hooked to the FBGA, the total capacitance of 29 nF was due to the capacitance of the board alone. When the FBGA was powered on, the total capacitance increased to 460 nF and was due to the capacitance of the board and FBGA. Therefore, the capacitance of the FBGA when the board is powered on is 431 nF.

3.1.2. Simulations. To match the measurement results, two types of simulations were performed. One simulation dealt with circuit components, and the other dealt with the parallel plane behavior. ADS was originally used to simulate the circuit components, but then the equations were derived and placed into Matlab. The program Ez-Power Plane (EzPP) was used to simulate the parallel power and return planes effect seen on the board. EzPP requires dimensions which are found in the stack-up of the board shown in Figure 3.3. This figure illustrates the separation of the planes, the placement of the circuit components used for the package, and the pieces added by Ez-Power Plane.

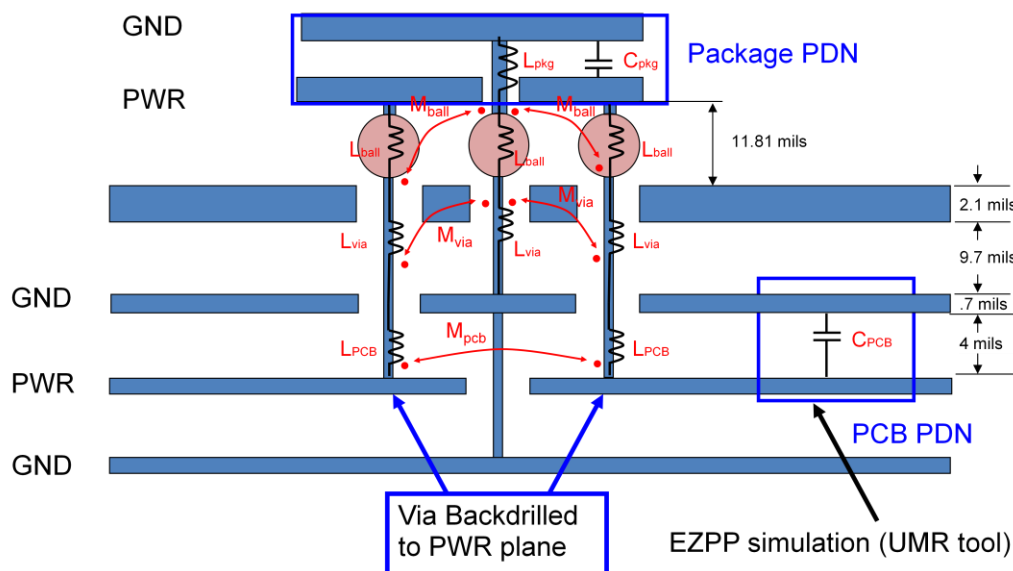


Figure 3.3. Altera Stratix II PCB Stack-Up

The program Ez-Power Plane (EzPP), created by the University of Missouri-Rolla Electromagnetic Compatibility Laboratory, was used to find the portion of the curve accountable for the wave propagations between the power and ground layers. This program looks at the low frequency parallel plate capacitance which is the capacitance added by the power and ground planes. It also takes into account the higher mode inductance and the resonance frequencies associated with the port locations and dimensions which are portrayed in Figure 3.2. Three ports were used in the EzPP simulation. The two ports used in the measurements were placed inside the EzPP simulation as well as a port placed at the center of the chip. The x-y port locations can be seen in Figure 3.2. The port size used for these simulations was a square 0.6 mm by 0.6 mm port. This value was the radius of the balls of the FBGA and was pulled from the Altera datasheet of the Stratix II. The dielectric thickness was set to four mils and the dielectric constant was set to 4.3. The loss tangent was set to 0.02. The metal thickness was 0.7 mils with a conductivity of copper.

In this case, the distributed portion is dominated by the geometry of the board. The first resonance for a board which is 10 inches by 10.5 inches is the TM_{z10} mode at 276 MHz. This frequency along with the other modes can be found by equation 6 and a few of these modes were calculated and are shown in Table 3.1

$$f_c(m, n) = \frac{1}{2\pi\sqrt{\mu\epsilon}} \sqrt{\left(\frac{m\pi}{a}\right)^2 + \left(\frac{n\pi}{b}\right)^2} \quad a > b, m > 0, n > 0 \quad (6)$$

Table 3.1. TM_z Modes

TM _z Modes					
$\begin{matrix} b=10 \text{ in} \\ a=10.5 \text{ in} \end{matrix}$	n = 0	n = 1	n = 2	n = 3	n = 4
m = 0	-	2.89E+08	5.78E+08	8.67E+08	1.16E+09
m = 1	2.76E+08	4.00E+08	6.41E+08	9.10E+08	1.19E+09
m = 2	5.52E+08	6.23E+08	7.99E+08	1.03E+09	1.28E+09
m = 3	8.28E+08	8.77E+08	1.01E+09	1.20E+09	1.42E+09
m = 4	1.10E+09	1.14E+09	1.25E+09	1.40E+09	1.60E+09

Everything below the TM_{z10} mode may be modeled using passive circuit components. The ADS model for the board when there is no power supplied is shown in Figure 3.4. The block labeled SNP1 stores the touchstone file created by EzPP, which implements the influence the planes have on the circuit. There are no connections attached to port 2 in this simulation, since no power was supplied to the FBGA. The two capacitances were found from the measurements to be 431 nF for the FBGA and 29 nF for the printed circuit board. The inductances and resistances were found from the measurements looking at the input impedances of ports one and three. Figures 3.5 and 3.7 show the input impedances of ports 1 and 3, and Figure 3.6 shows the transfer impedance between the two ports. These measurement and simulation comparisons were primarily to check that the model is correct before analyzing the FBGA effects on the board impedance.

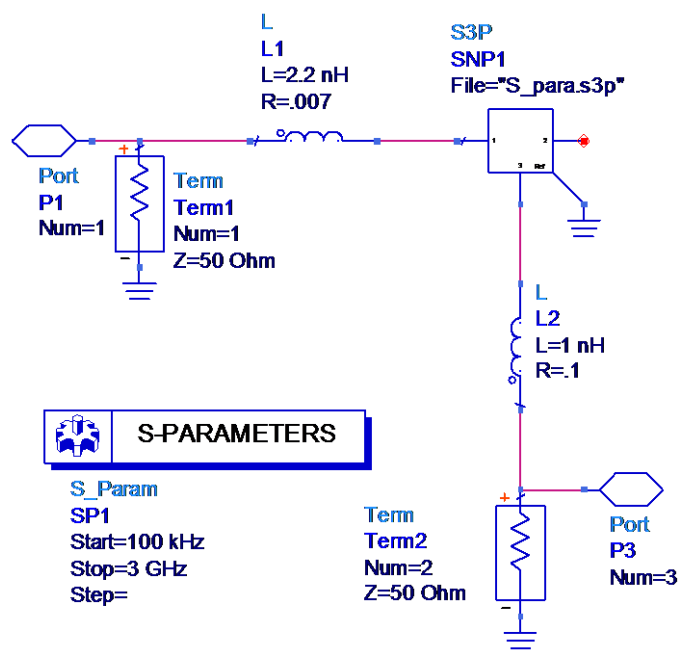


Figure 3.4. ADS Simulation for No Power Supplied to Board

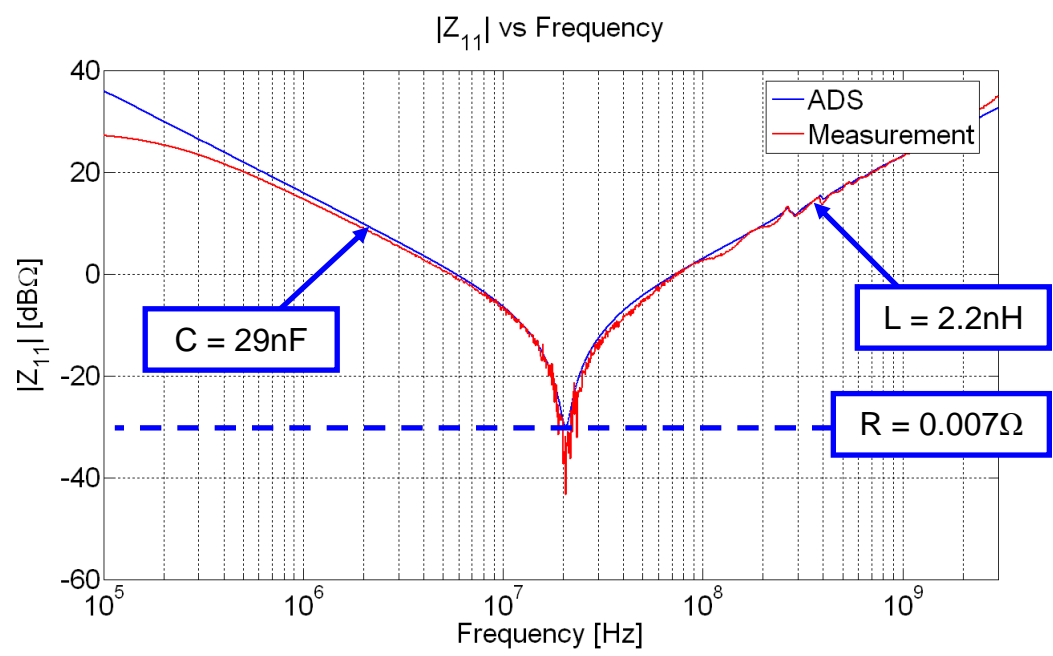


Figure 3.5. Magnitude of the Input Impedance at Port 1

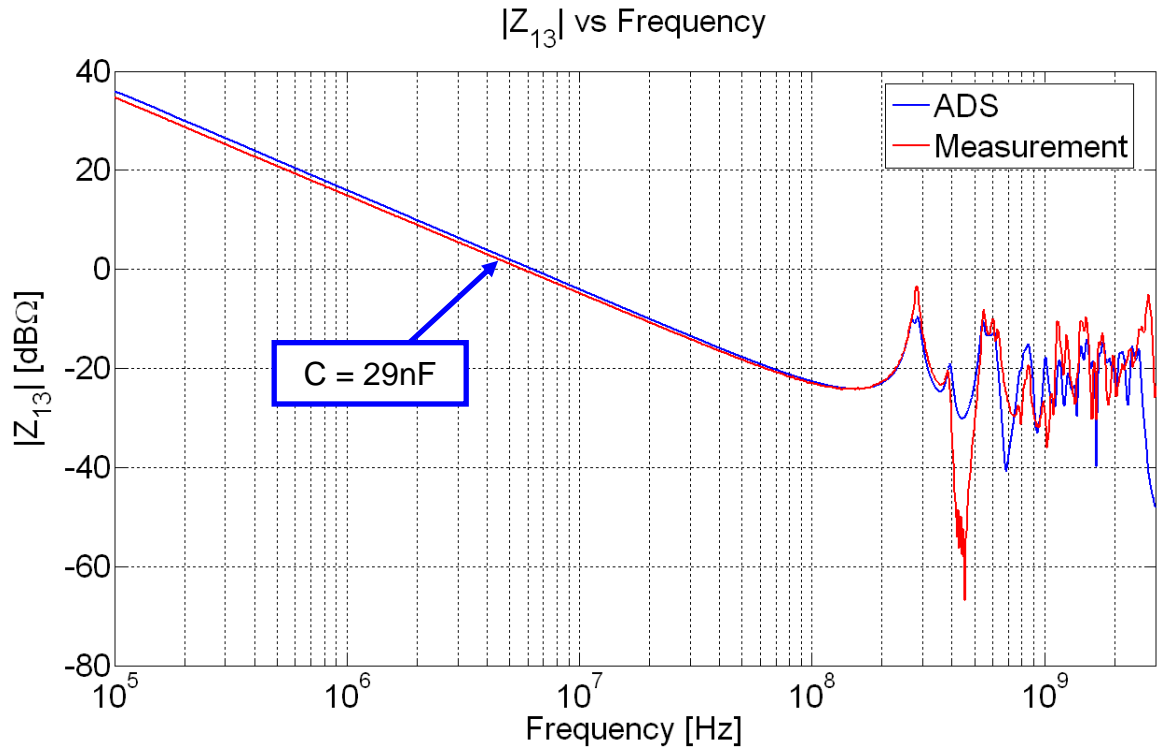


Figure 3.6. Magnitude of the Transfer Impedance Between Ports 1 and 3

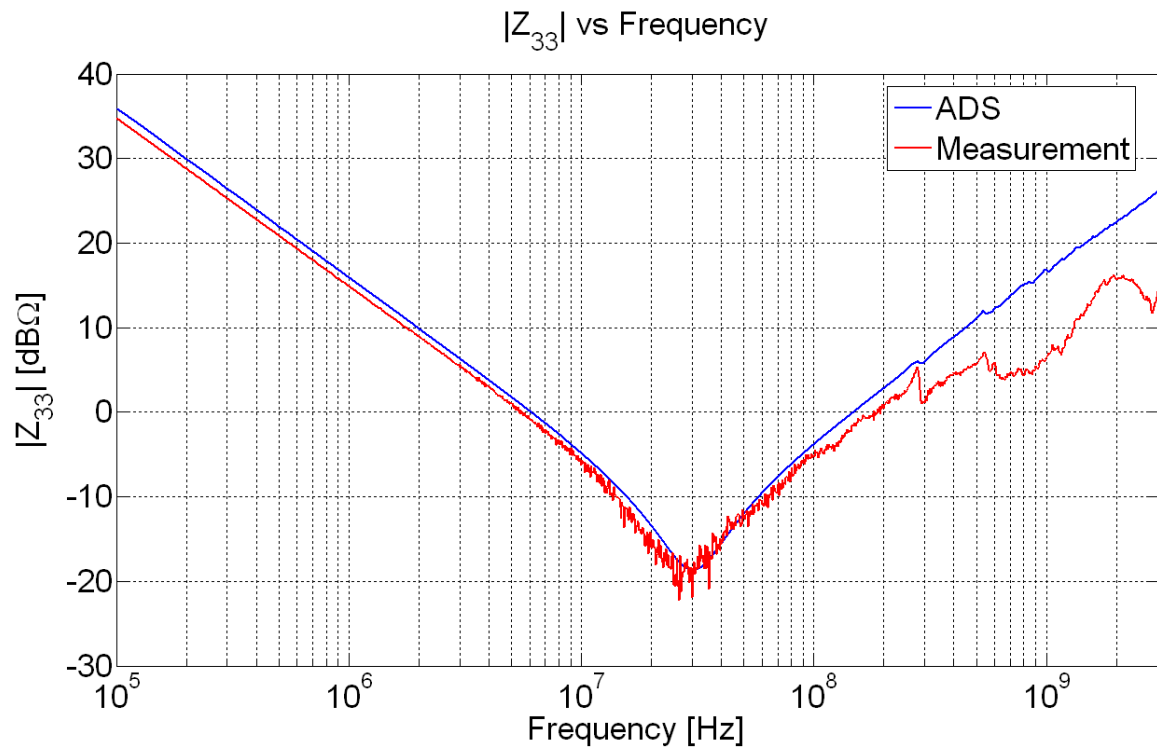


Figure 3.7. Magnitude of the Input Impedance at Port 3

Since the simulation values match the measurements for port one and three, the only part missing is the added effects of the FBGA. The inductance and resistance values of the FBGA were given by Altera, while the capacitance value used was the measured value. Figure 3.8 shows the modified ADS model to include the FBGA. Some of the resistances were changed to fit the measurements curve better, but the inductances remained the same value. The measurement and simulation comparison for the magnitude of the transfer impedance when power is supplied to the board is shown in Figure 3.9.

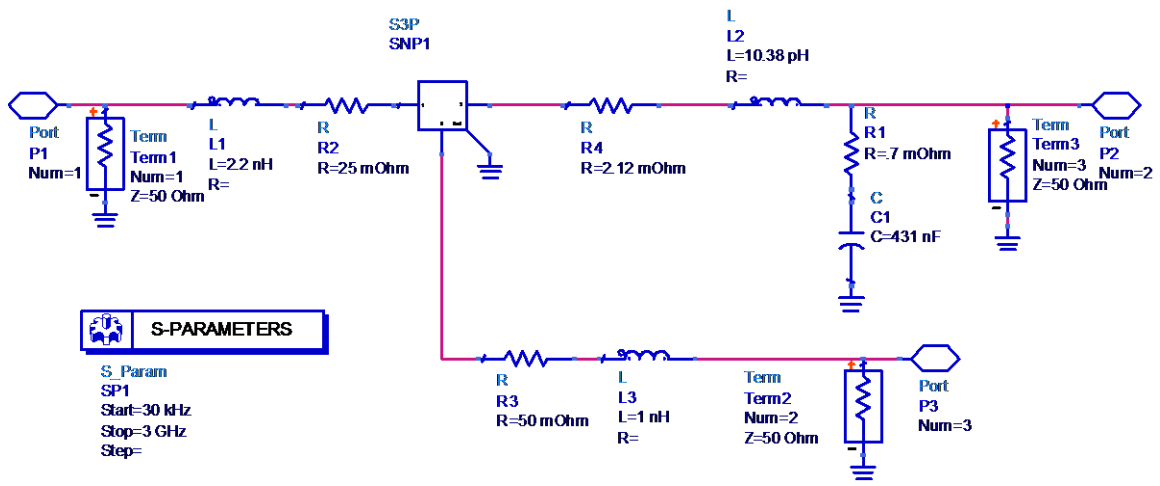


Figure 3.8. ADS Model

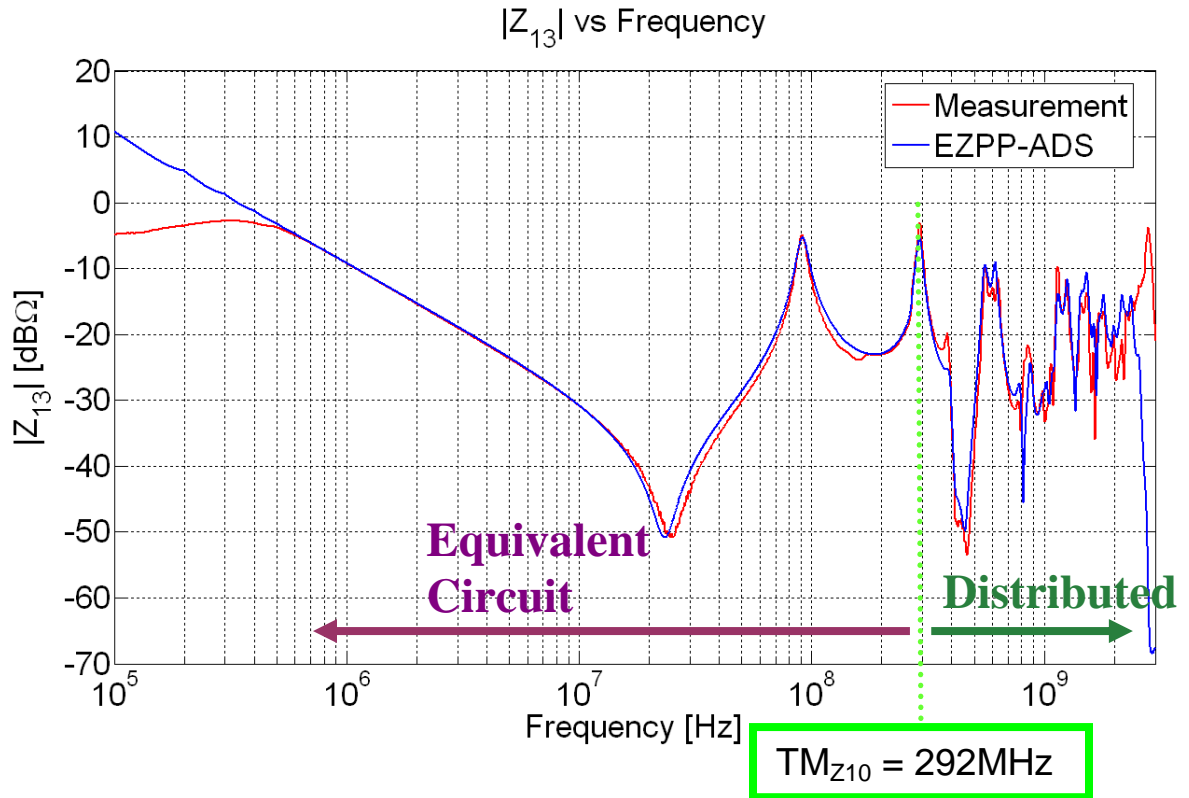


Figure 3.9. Magnitude of Z_{13} ADS and EzPP Simulation Results vs. Measurements

These results show that our simulations are effective at matching the measurements. However, it is still unknown what parts of the geometry and which circuit components in the ADS model are responsible for each of the two resonances before the TM_{z10} mode. For the resonance at 23.5 MHz, it is known that the total capacitance is 460 nF, and the inductance of 99.7 pH is found by using equation 7.

$$f = \frac{1}{2\pi\sqrt{LC}} \quad (7)$$

The next resonance at 91 MHz should be dominated by the smaller capacitance of 29 nF and the inductance making the first resonance. When using the inductance of 99.7 pH in equation 7, the capacitance comes out to be 30.68 nF. The capacitance values are correct and can be pointed out in the circuit model. However, there are no inductors in the ADS model that are close to calculated 99.7 pH. Therefore, this inductance must be buried inside the EzPP results.

3.1.3. Analytical Calculations. Calculations were made by hand and then entered into Matlab to compare the analytical calculations with the measurements and simulations. The initial schematic shown in Figure 3.10 is similar to the ADS model in Figure 3.8 except the s-parameter box that include the touchstone file generated by EzPP was replaced with a capacitor C_{planes} which represented the capacitance of the planes. R is the added resistance of the planes between ports. L_{port} and R_{port} are the measured inductance and resistance of port one. Similarly, L_{probe} and R_{probe} are the measured inductance and resistance of port three. L_{total} includes all the inductances add to the circuit by the internal inductance of the package and package connection seen in Figure 3.3. This value was given by Altera to be their measured inductance. R_{pkg} and C_{pkg} was the resistance and capacitance introduced to the circuit by the chip. R_{pkg} was given by Altera as their measured inductance, and C_{pkg} was the measured capacitance of the package which is shown in Figures 3.5, 3.6, and 3.7.

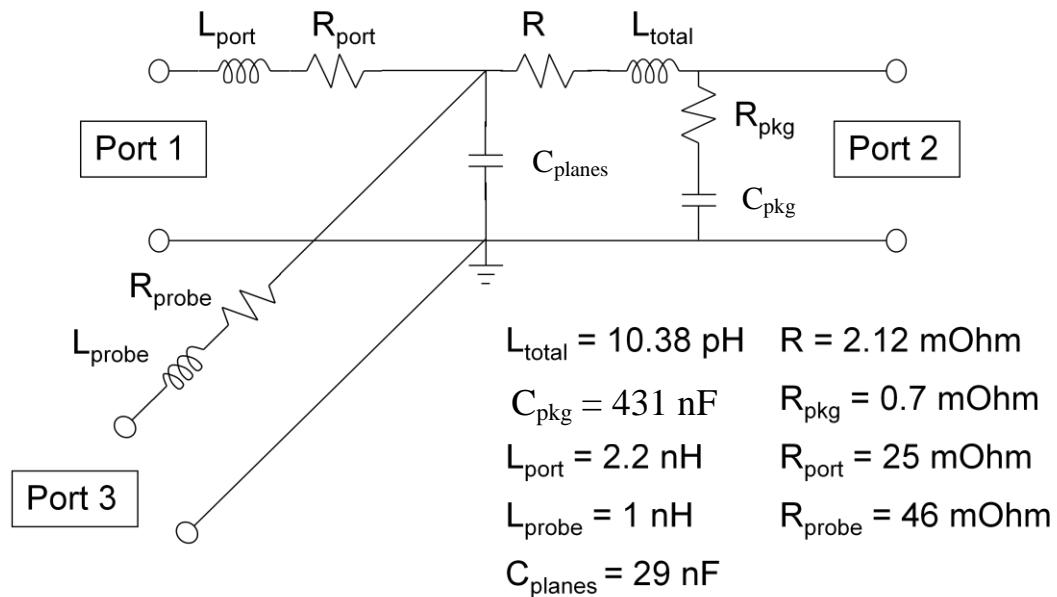


Figure 3.10. Initial Schematic Used for Analytical Calculations

The transfer impedance was derived using the definition of the transfer impedance from port one to three which is given by equation 8. It says the transfer impedance from port one to port three is defined as the voltage seen at port one divided by the current seen at port three while the current at all other ports are set to zero. When using equation 8 to find Z_{13} , the circuit shown in Figure 3.10 simplifies to the circuit shown in Figure 3.11. The calculations are shown in equations 9 and 10.

$$Z_{13} = \frac{V_1}{I_3} \Big|_{I_1=0} \Big|_{I_2=0} \quad (8)$$

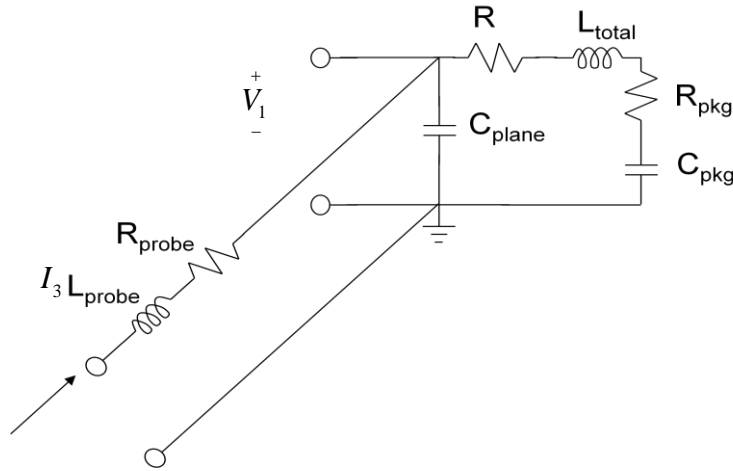


Figure 3.11. Simplified Circuit for Z_{13} Calculations

$$Z_{13} = \frac{\left(\frac{1}{sC_{\text{plane}}}\right) \left(sL_{\text{total}} + R + R_{\text{pkg}} + \frac{1}{sC_{\text{pkg}}}\right)}{\frac{1}{sC_{\text{plane}}} + sL_{\text{total}} + R + R_{\text{pkg}} + \frac{1}{sC_{\text{pkg}}}} \quad (9)$$

$$Z_{13} = \frac{L_{\text{total}} C_{\text{pkg}} s^2 + (R + R_{\text{pkg}}) C_{\text{pkg}} s + 1}{s(L_{\text{total}} C_{\text{plane}} C_{\text{pkg}} s^2 + (R + R_{\text{pkg}}) C_{\text{plane}} C_{\text{pkg}} s + (C_{\text{plane}} + C_{\text{pkg}}))} \quad (10)$$

Note that there are no influences by either the probe at port three or the SMA jack at port one. Therefore, the impedance of the planes and the FBGA are known once Z_{13} is obtained. Equation 10 was entered into Matlab, and the results were compared with the

measurements and simulations. As it can be seen below in Figure 3.12, the capacitance alone does not come close to creating an accurate simplified model of the EzPP block in the ADS model. While the measurement and ADS model match fairly well, the analytical calculations of the circuit appear to be missing an inductance. The inductance needed to hit the first resonance at 23.5 MHz was found earlier to be 99.7 pH. Therefore, some changes were made to the initial model, so the analytically calculated results match the ADS model better.

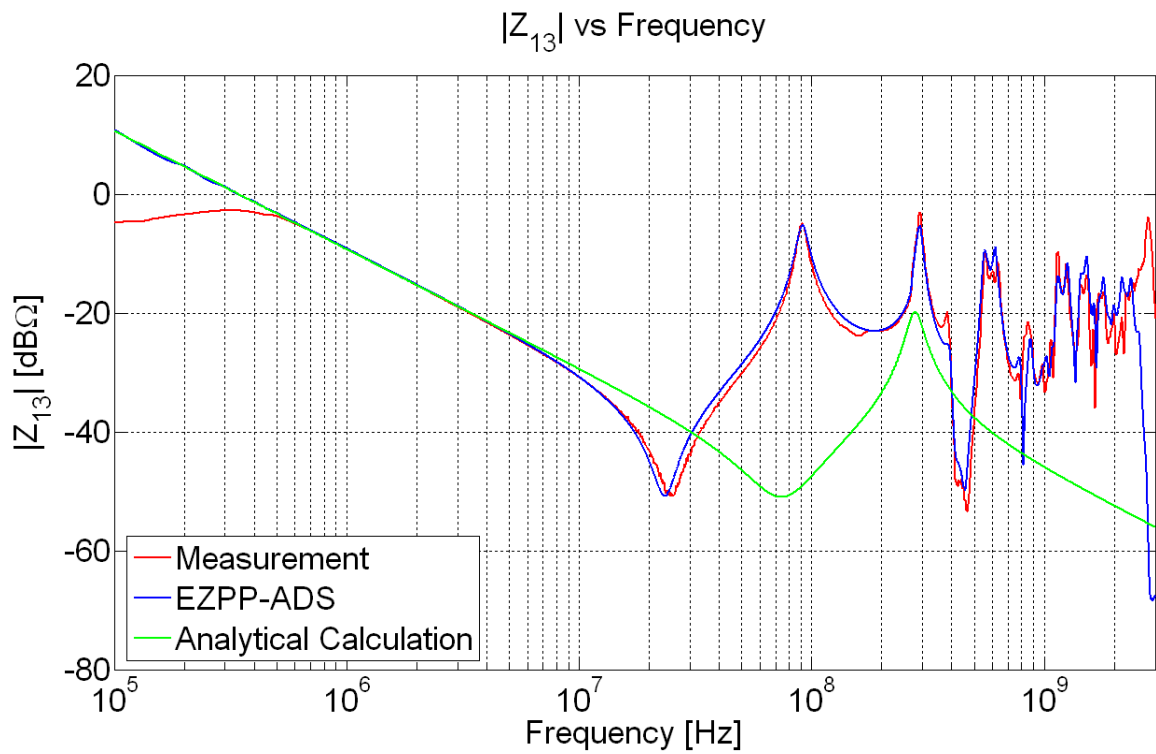


Figure 3.12. Z_{13} Magnitude Comparison

Making the curves match better was accomplished by adding the inductor L_{planes} with a value of 91 pH to the model, as shown in Figure 3.13. This is the inductance calculated by EzPP that is associated with the port size and location. The effect of this inductance is critical, since it shifts the curve onto the measurements and ADS curves as shown in Figure 3.14.

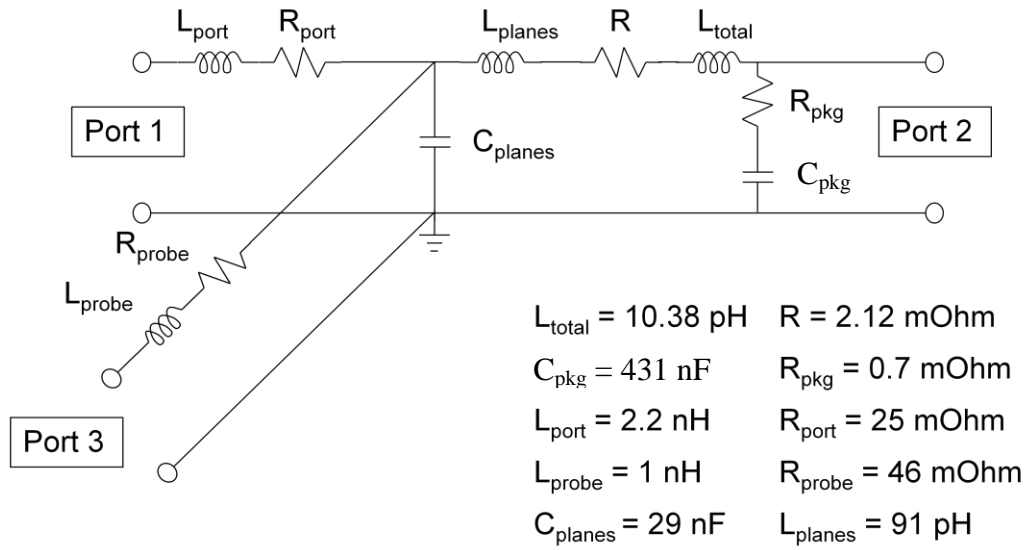


Figure 3.13. Schematic Including Higher Mode Inductance Used in Analytical Calculations

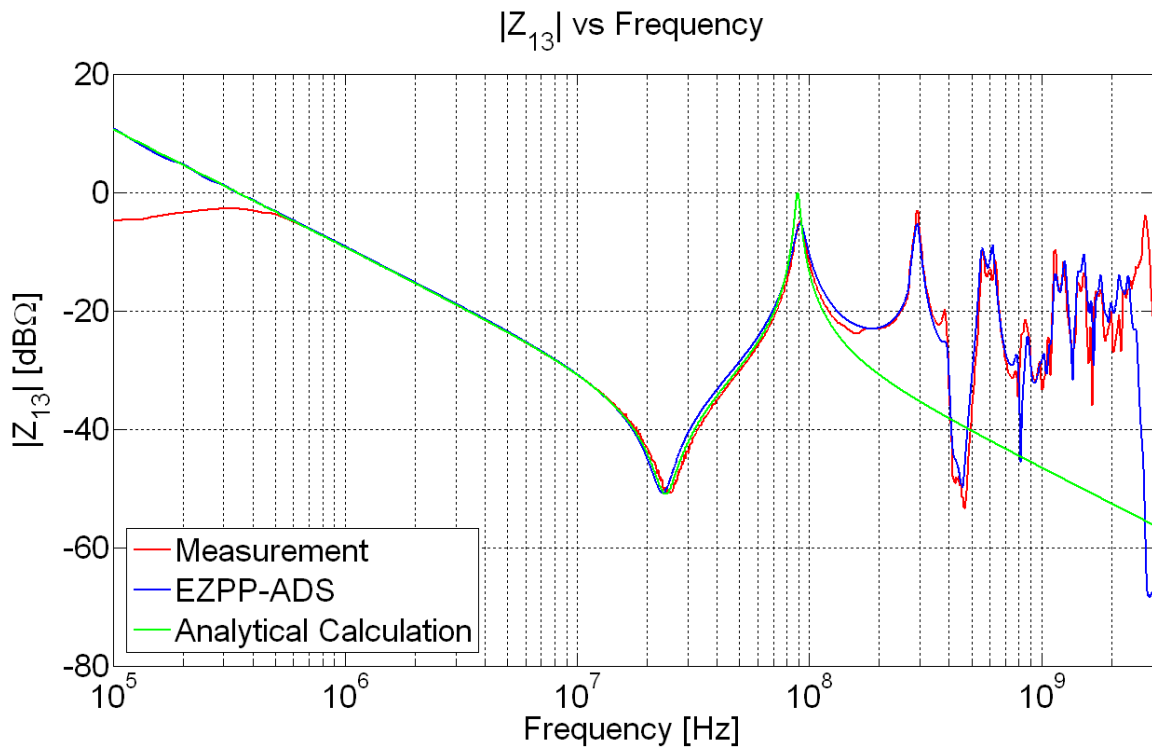


Figure 3.14. Z_{13} Magnitude Comparison with Higher Mode Inductance Added into the Model

This model is still not quite right. A resistance is needed to make the second resonance match. The second resonance is a pole at 91 MHz and is formed by the capacitor C_{planes} , the sum of the inductance of L_{planes} and L_{total} , and the added resistance R_G resonating in parallel. Adding the resistance R_G in parallel with the capacitance in Figure 3.15 made the curve matched much better as shown in Figure 3.16.

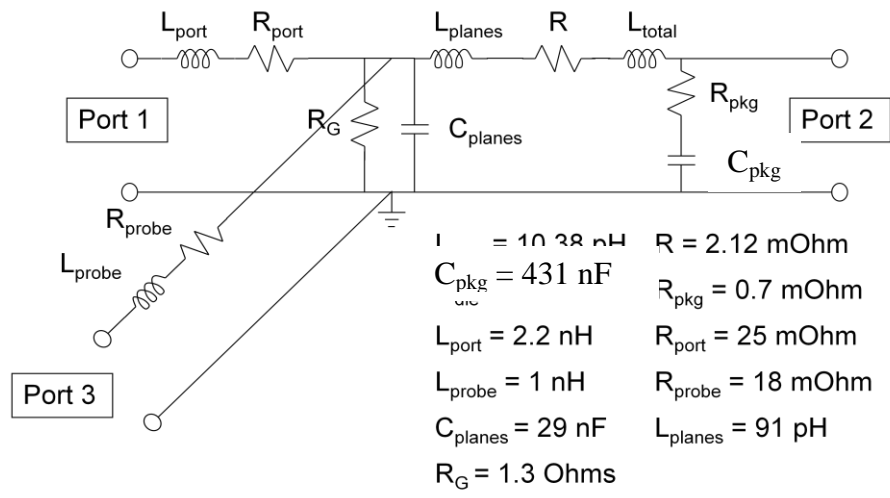


Figure 3.15. Schematic Including Higher Mode Inductance and Parallel Resistance

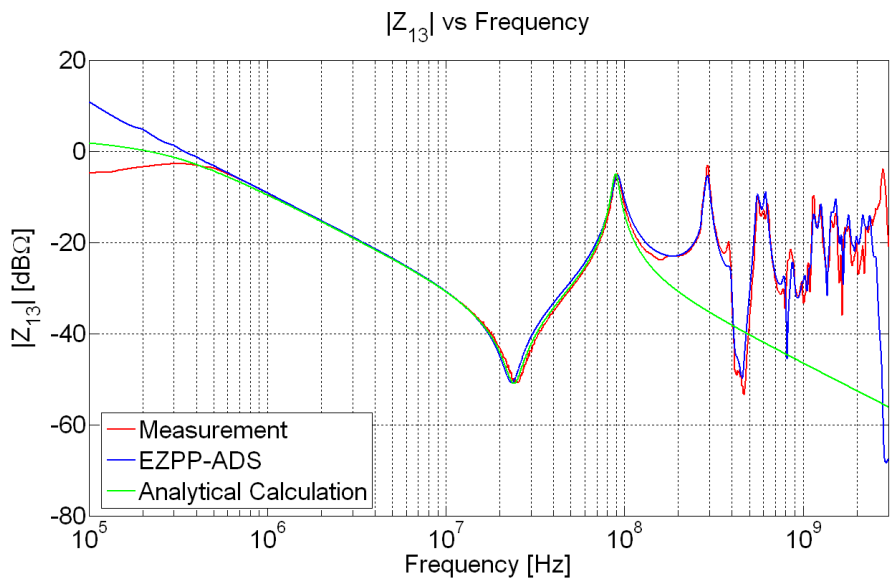


Figure 3.16. Z_{13} Magnitude Comparison with Higher Mode Inductance and Parallel Resistance Added into the Model

The three curves match up to the second resonance which covers the lumped element part of the circuit. The third resonance is the TM_{z10} mode and draws the line between the equivalent circuit part of the impedance plot and the distributed part as shown earlier in Figure 3.9.

After the transfer impedance plot was sound, the input impedance at port one and three needed to be checked. The input impedances at the ports were derived starting with their definitions. Equation 11 shows the definition for the input impedance at port one, and equation 12 shows the equation for port three.

$$Z_{11} = \left. \frac{V_1}{I_1} \right|_{I_2=0} \Big|_{I_3=0} \quad (11)$$

$$Z_{33} = \left. \frac{V_3}{I_3} \right|_{I_1=0} \Big|_{I_2=0} \quad (12)$$

Deriving the input impedance at port one and three involved little effort, since the impedance for everything else other than resistance and inductance of the port or probe was incorporated into the transfer impedance equation. For this reason, the transfer impedance is found in the input impedance equations for port one and three. The derived equation for Z_{11} can be seen in equation 13 and Z_{33} can be seen in equation 14.

$$Z_{11} = \frac{50(L_{\text{port}} s + R_{\text{port}} + Z_{13})}{50 + L_{\text{port}} s + R_{\text{port}} + Z_{13}} \quad (13)$$

$$Z_{33} = \frac{50(L_{\text{probe}} s + R_{\text{probe}} + Z_{13})}{50 + L_{\text{probe}} s + R_{\text{probe}} + Z_{13}} \quad (14)$$

Figures 3.17 and 3.18 show the comparison between the plots of the analytical equations entered into Matlab and the simulation and measurement results. It should be noted that the port inductance seen in EzPP plays a huge role in the resonance around 91 MHz. This resonance would not be seen at all if the inductance L_{planes} was removed from the circuit.

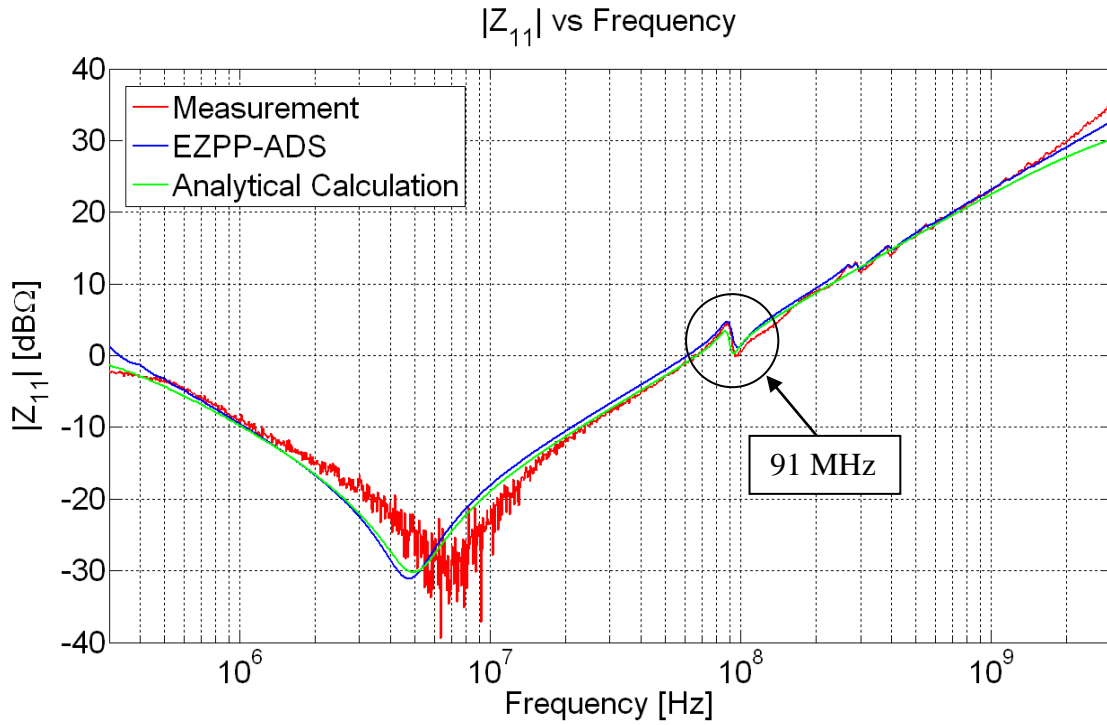


Figure 3.17. Input Impedance for Port 1

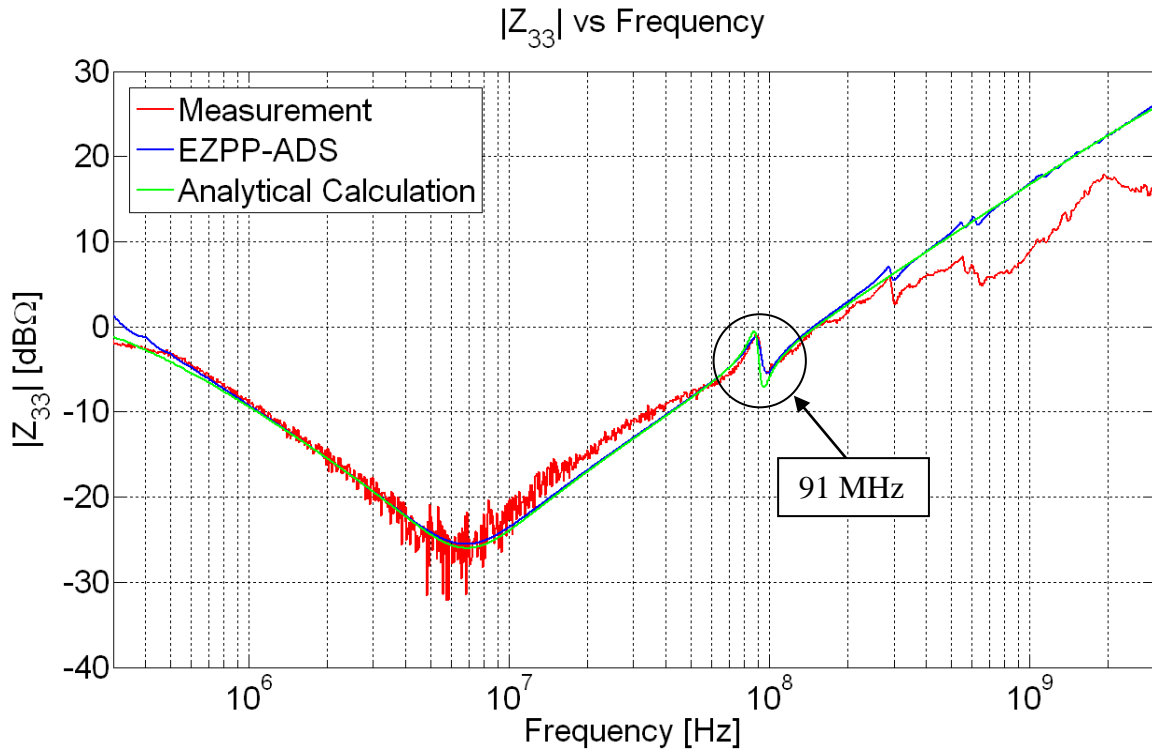


Figure 3.18. Input Impedance Seen at Port 3

3.2. IMPEDANCES SEEN AT PORT TWO

Since the measurements were too difficult to make, only simulations and analytical calculations were performed for port two.

3.2.1. Simulations. Using the same ADS model shown in Figure 3.8, the transfer impedances Z_{12} and Z_{32} along with the input impedance Z_{22} were simulated and the results are illustrated in Figure 3.19. All three of the curves show an inductance at first. The first resonance caused by the equivalent circuit model is a pole seen at 91MHz. This is the same pole that was seen before in Z_{13} . A second resonance is seen in the Z_{32} which is a zero around 190 MHz. The rest of these resonances are dominated by the effects seen by the geometry of the board.

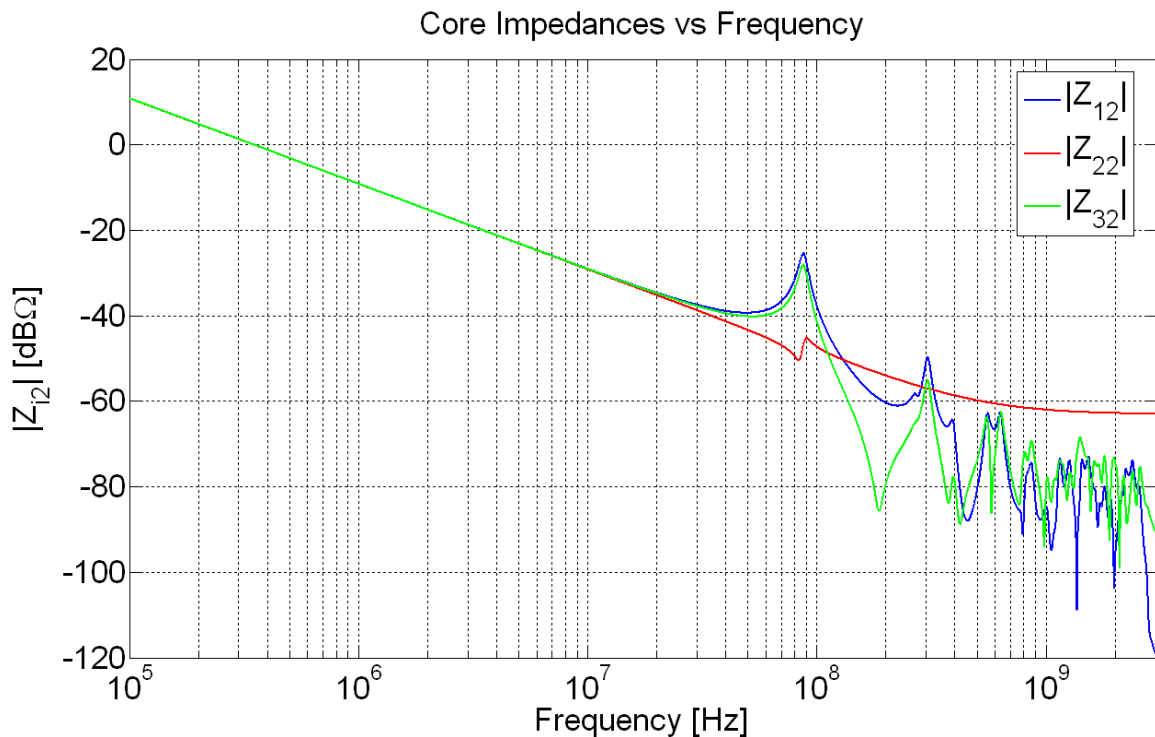


Figure 3.19. ADS Simulation Results for Port Two Impedances

3.2.2. Analytical Calculations. The same analytical calculations were performed for port two that were completed previously for ports one and three using the schematic shown in Figure 3.15.

The transfer impedance of port one to port two as well as the impedance from port three to port two was examined. The transfer impedance equations for Z_{12} and Z_{32} are given in equations 15 and 16.

$$Z_{12} = \left. \frac{V_1}{I_2} \right|_{\substack{I_1=0 \\ I_3=0}} = \frac{R_{\text{pkg}} C_{\text{pkg}} s + 1}{s(L_{\text{total}} C_{\text{plane}} C_{\text{pkg}} s^2 + (R + R_{\text{pkg}}) C_{\text{plane}} C_{\text{pkg}} s + (C_{\text{plane}} + C_{\text{pkg}}))} \quad (15)$$

$$Z_{32} = \left. \frac{V_3}{I_2} \right|_{\substack{I_1=0 \\ I_3=0}} = \frac{(R + R_{\text{pkg}}) C_{\text{pkg}} s + 1}{s(L_{\text{total}} C_{\text{plane}} C_{\text{pkg}} s^2 + (R + R_{\text{pkg}}) C_{\text{plane}} C_{\text{pkg}} s + (C_{\text{plane}} + C_{\text{pkg}}))} \quad (16)$$

The input impedance equation was also derived and is given by equation 17. It should be noted that the impedances seen at port two all have the same denominator. This means they all have the same poles although the only one really seen is at 91 MHz as shown in Figure 3.19. The difference between the impedance curves is seen in the numerator or the zeros.

$$Z_{22} = \left. \frac{V_2}{I_2} \right|_{\substack{I_1=0 \\ I_3=0}} = \frac{(L_{\text{total}} C_{\text{plane}} s^2 + R C_{\text{plane}} s + 1)(R_{\text{pkg}} C_{\text{pkg}} s + 1)}{s(L_{\text{total}} C_{\text{plane}} C_{\text{pkg}} s^2 + (R + R_{\text{pkg}}) C_{\text{plane}} C_{\text{pkg}} s + (C_{\text{plane}} + C_{\text{pkg}}))} \quad (17)$$

4. LOCATING PARASITIC CIRCUIT ELEMENTS IN MOTOR DRIVES

The motor drive examined was a variable-frequency drive. These drives vary frequencies of the AC power supply used to power the motor to regulate the rotational speed of AC motors. In the system studied, the length of the cable connecting the drive to the motor was constant, as well as the size of the motor. The drive itself was already designed although ideas for improvement were encouraged. The frequencies of the system said to have problems were from 30 MHz to 40 MHz though a wider range was examined.

4.1. CURRENT PROBE EFFECTS ON MEASUREMENTS

A current probe was used in the setup to find the transfer impedance, so the effects it had on the measurements' accuracy was of high importance. The Fisher F-61, F-62, and F-65 were a group of three current probes which were compared and examined.

4.1.1. Copper Strap. A copper strap was used in characterizing of the probes and the through calibration for calibrating out the effects of the current probe when finding the transfer impedance of the system. When creating this strap, it was important to get the loop area as small as possible, yet keep it large enough to fit on the clamp on the current probes. Another factor that was considered was the strap width. The narrower the strap was made, the higher the inductance would be due to current crunching. In this case, the width was made 6 cm, since that was the width of the SMA jack that was used. The creation of this strap included soldering one end of a strip of copper to the reference of a SMA jack, and the other end to the center conductor of the same jack as shown in Figure 4.1. The end soldered to the center conductor was cut to more of a point where it connected to the jack. This was to help with the connection mechanically, but to also help eliminate the chance of current crunching which would add inductance. The copper strap was wrapped in electrical tape after all the connections were made. This was done to reduce any chances of the strap shorting on the current probe. Figure 4.2 illustrates this step.

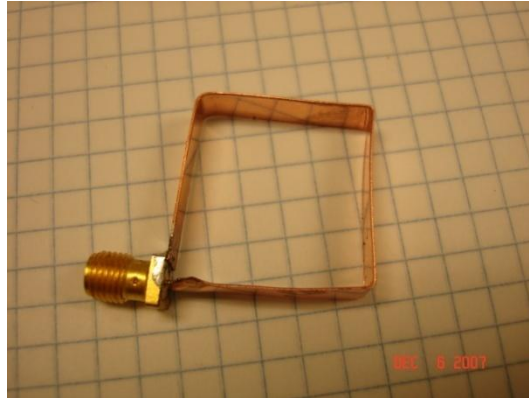


Figure 4.1. Copper Strap



Figure 4.2. Copper Strap Wrapped in Electrical Tape

Input impedance measurements were performed on the strap to see how good it performed at higher frequencies. Figure 4.3 illustrates that the input impedance magnitude consists of a 20 dB per decade slope and the phase is a relatively firm 90 degrees up to around 300 MHz. At this point, the strap has a real term which begins to influence the curve, causing the input impedance of the strap to no longer be purely imaginary. This shows that the calibration becomes a factor of error above 300 MHz.

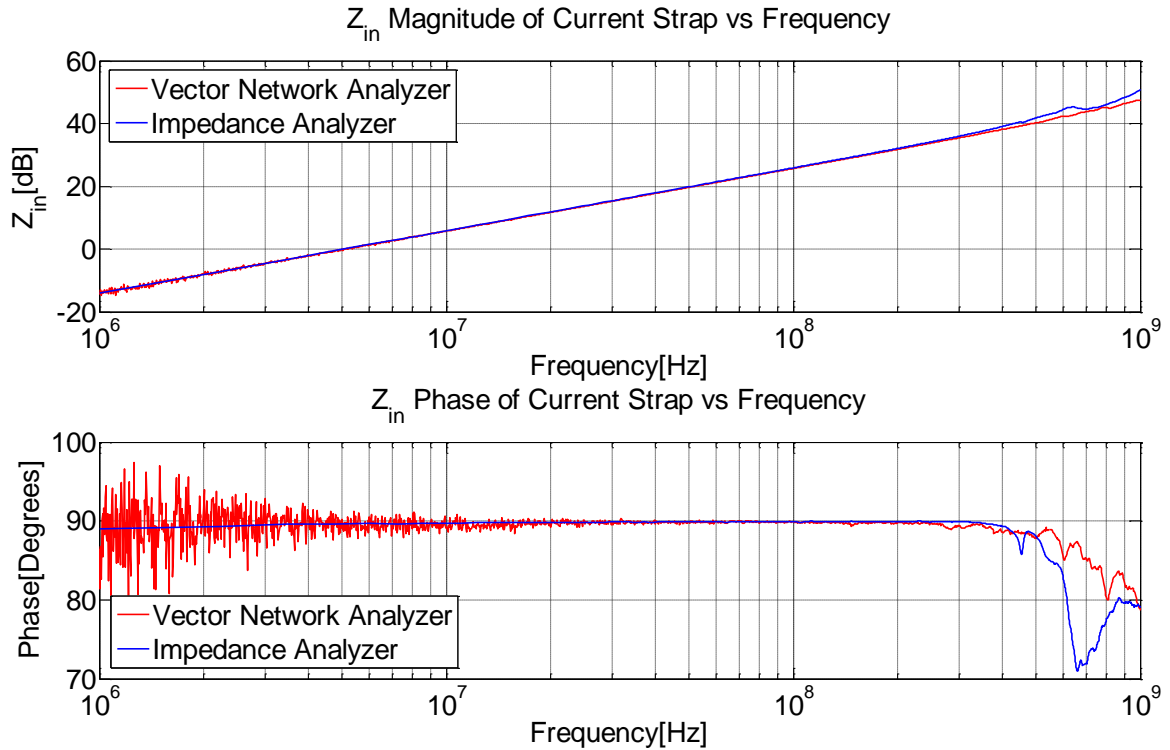


Figure 4.3. Input Impedance of Current Strap

4.1.2. Current Probe Transfer Impedance. The transfer impedance of each current probe was found using the copper strap created. Since the VNA measures the voltages at both the current probe and the copper strap, the measurement can be modeled as that illustrated in Figure 4.4. The measurement setup for each current probe was the same and can be seen in Figure 4.5.

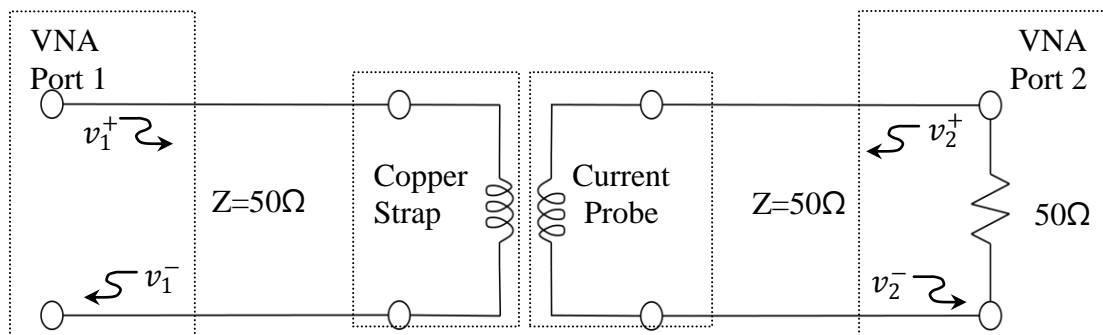


Figure 4.4. Equivalent Circuit Model for Transfer Impedance Measurement Setup

Looking at this model, the transfer impedance was derived by starting with the fundamental equation. Equation 18 defines the transfer impedance from port one to port two.

$$Z_T = \left. \frac{V_1}{I_2} \right|_{I_1=0} = \frac{S_{21}}{1-S_{11}} Z_o \quad (18)$$



Figure 4.5. Current Probe Transfer Impedance Measurement Setup

After the measurements were taken, the transfer impedance was found using equation 18. The results of the different probe transfer impedances are shown in Figure 4.6 and can be compared with the manufactures data shown below the measured data in Figures 4.7, 4.8, and 4.9. However, since the copper strap was used in these measurements the errors seen before in Figure 4.3 are seen again here once the curve gets above 300 MHz. Up to this point, the curves for the probes match quite well.

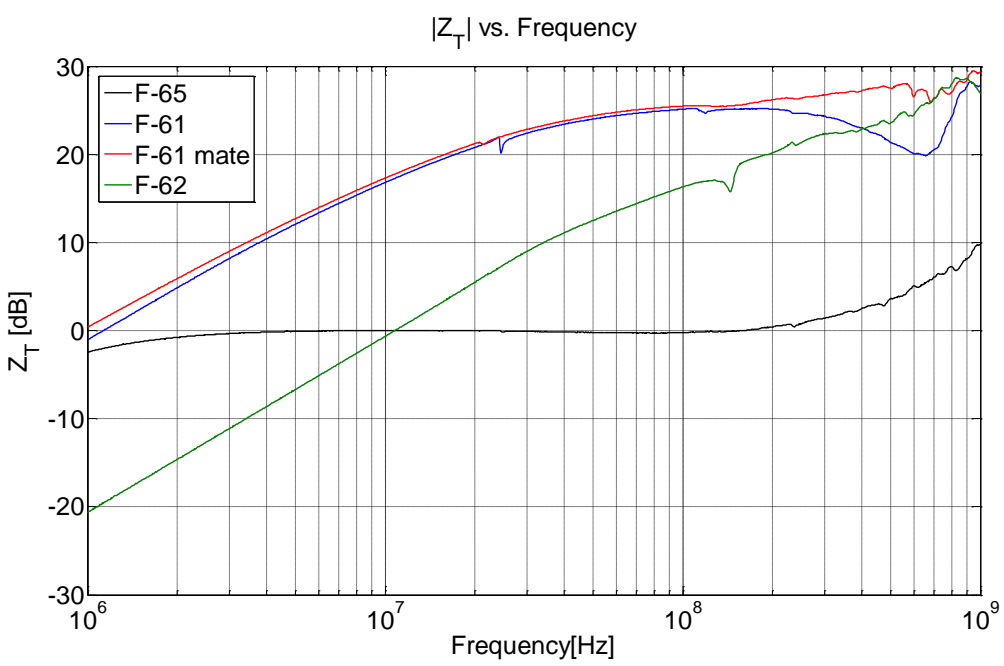


Figure 4.6. Transfer Impedance of the Three Current Probes Tested

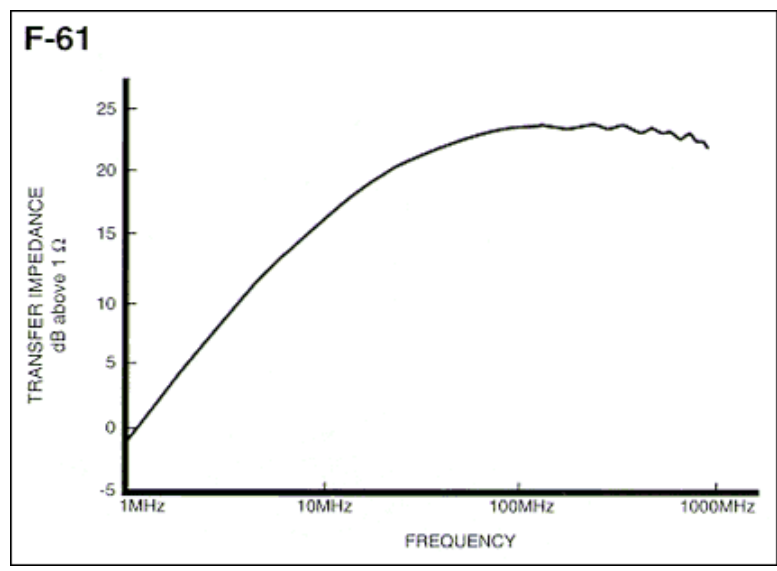


Figure 4.7. Manufacturer's Transfer Impedance Plot for the F-61

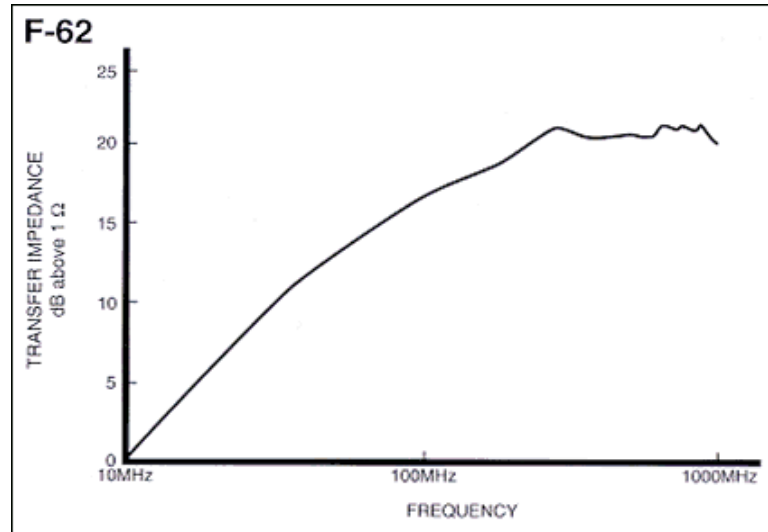


Figure 4.8. Manufacturer's Transfer Impedance Plot for the F-62

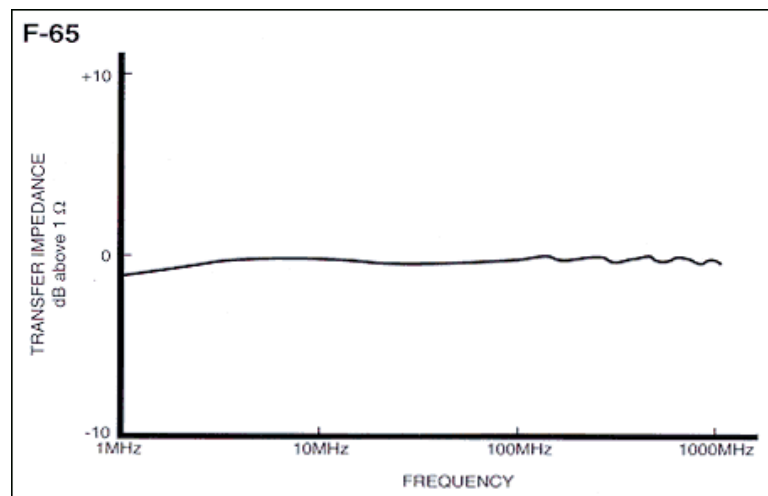


Figure 4.9. Manufacturer's Transfer Impedance Plot for the F-65

4.2. MEASURED IMPEDANCE OF MOTOR DRIVE TO CABLES

Measurements began by looking at the source of the switching which was the IGBT module. One set of measurements was performed by placing a probe inside the IGBT module, while another set was performed outside of the module. This would show the effect the module had on the transfer impedance.

4.2.1. Measurements Performed from Inside IGBT. The setup for the measurements started by figuring out where to solder the semi-rigid coaxial probe. The schematic of the IGBT is shown in Figure 4.10. Figure 4.11 shows the pin and component locations.

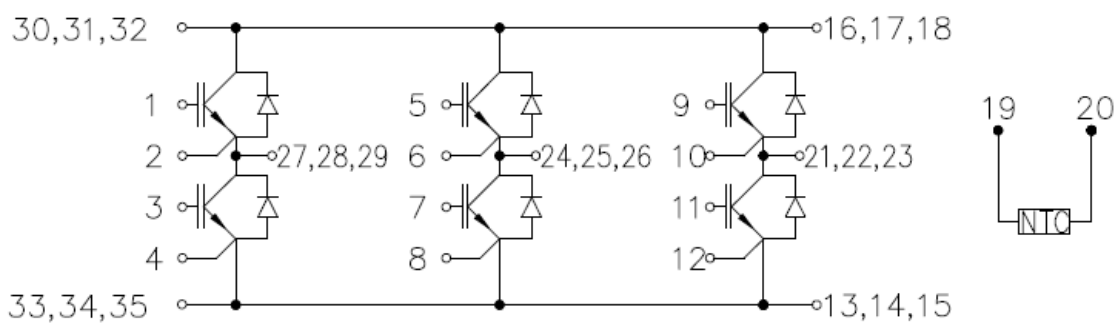


Figure 4.10. IGBT Schematic

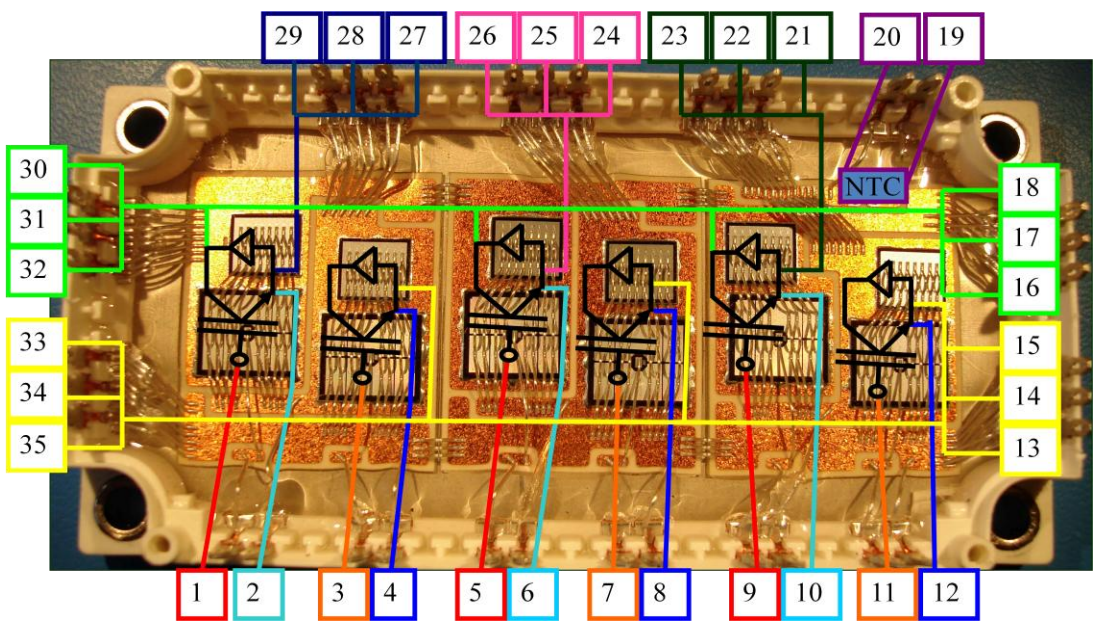


Figure 4.11. IGBT Pin and Component Locations

To make this measurement, a semi-rigid coaxial probe was placed across the collector and emitter of the IGBT with its gate connected to pin 1. The outer conductor

was soldered to the collector which was the positive rail. The inner conductor was connected to the emitter which heads out to the motor. Figures 4.12 and 4.13 illustrate the connection of the probe. The IGBT is thought of as a source for this measurement, since it allows the current flow through freely when it switches. Therefore, this measurement displays what the current sees when the IGBT lets current pass. The connection of the semi-rigid coaxial probe made up port one. The other port of the VNA was connected to a current probe clamped around a bus of three wires running from the drive to the three phase motor. The wires were tied together and spaced 10 inches above a sheet of aluminum using blue insulating foam to maintain a consistent separation. The current probe was separated from the cable mounting plate of the drive by five centimeters. Copper tape was used to create a good path for the current to return from the aluminum sheet to the heat sink where the reference of the IGBT module was mounted. The setup is portrayed in Figure 4.14.

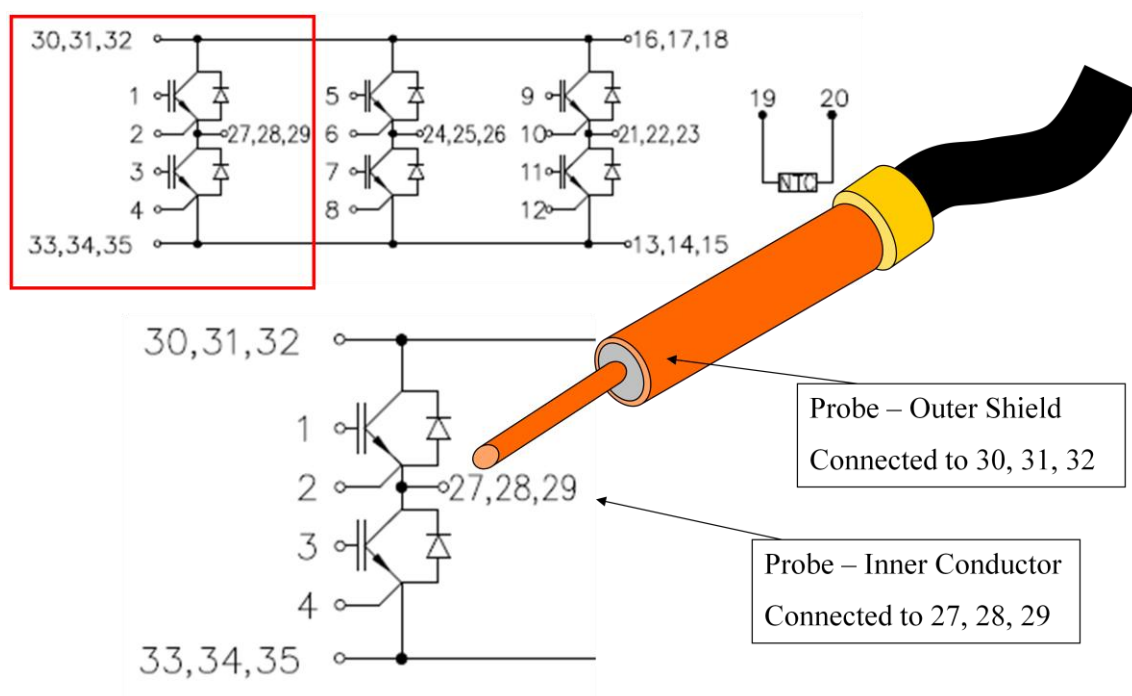


Figure 4.12. Probe Connection Across IGBT Shown on the Schematic

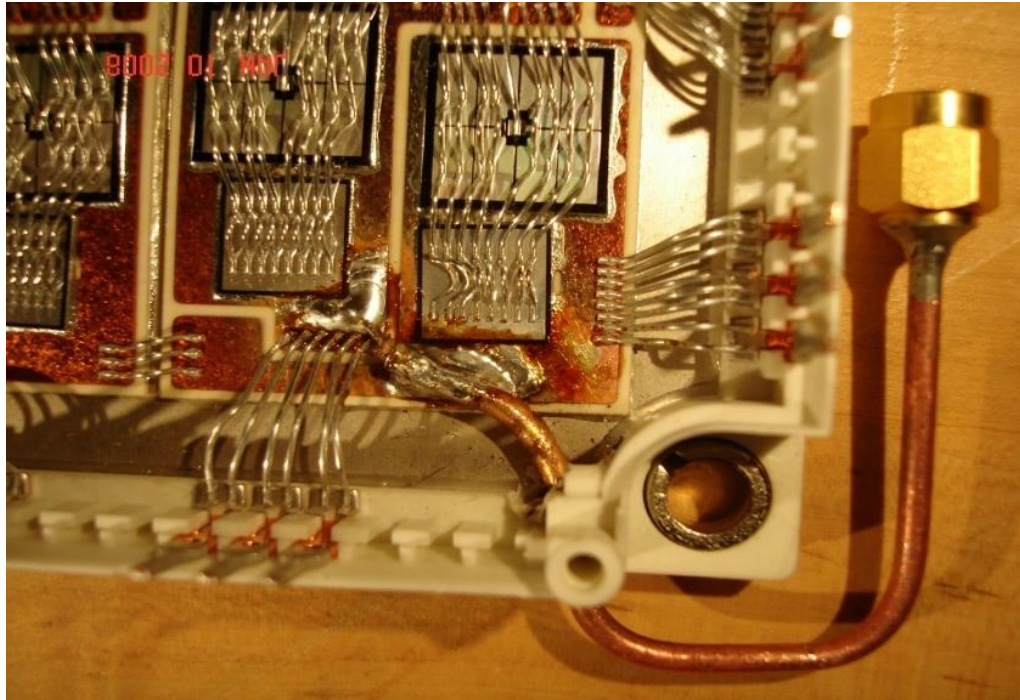


Figure 4.13. Probe Connection to IGBT Module

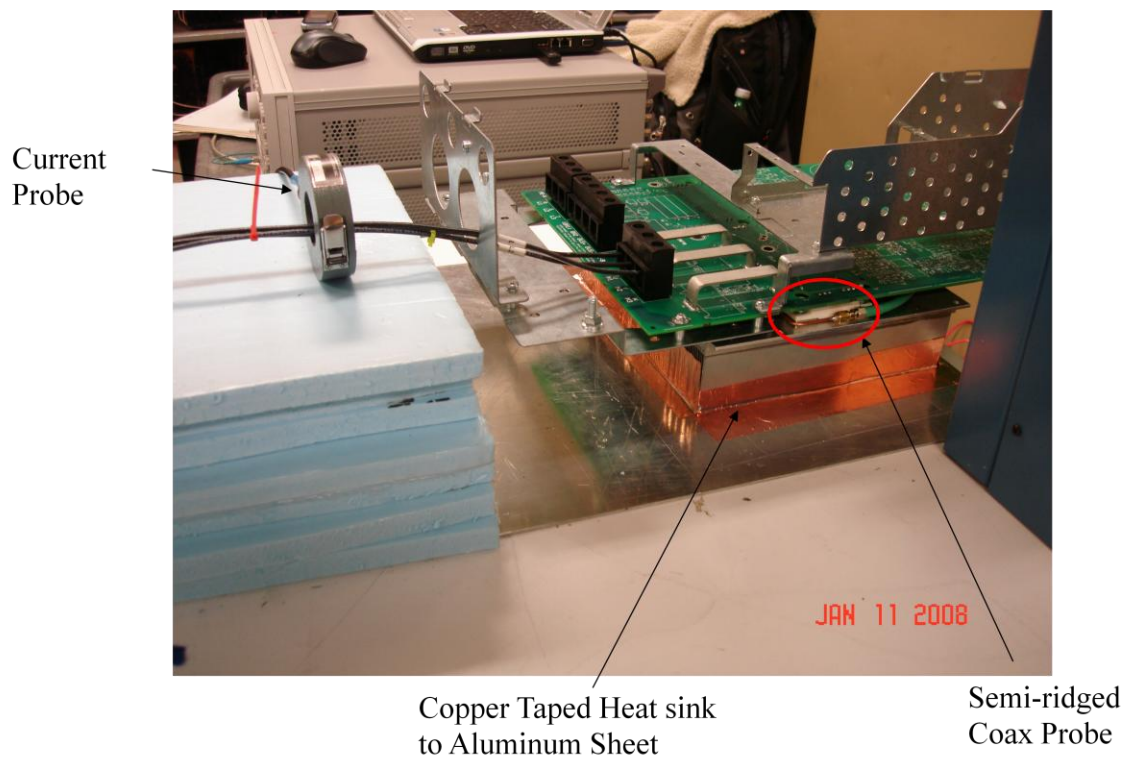


Figure 4.14. Setup for Transfer Impedance from IGBT to Cables Leading to the Motor

4.2.2. Input Impedance Looking into the IGBT Module. The input impedance looking into the IGBT module was measured with the impedance analyzer using the low impedance test head. The setup resembled that shown in Figure 4.14, except the current probe was not attached. The impedance analyzer was connected to the semi-rigid coaxial probe. The calibration was performed at the low impedance test head, and a port extension was used to move the calibration plane up to the tip of the semi-rigid coaxial probe inside the IGBT. The data taken is shown below in Figure 4.15. Although the problems were said to be around 30 to 40 MHz, the resonance of the system is centered around 12 MHz.

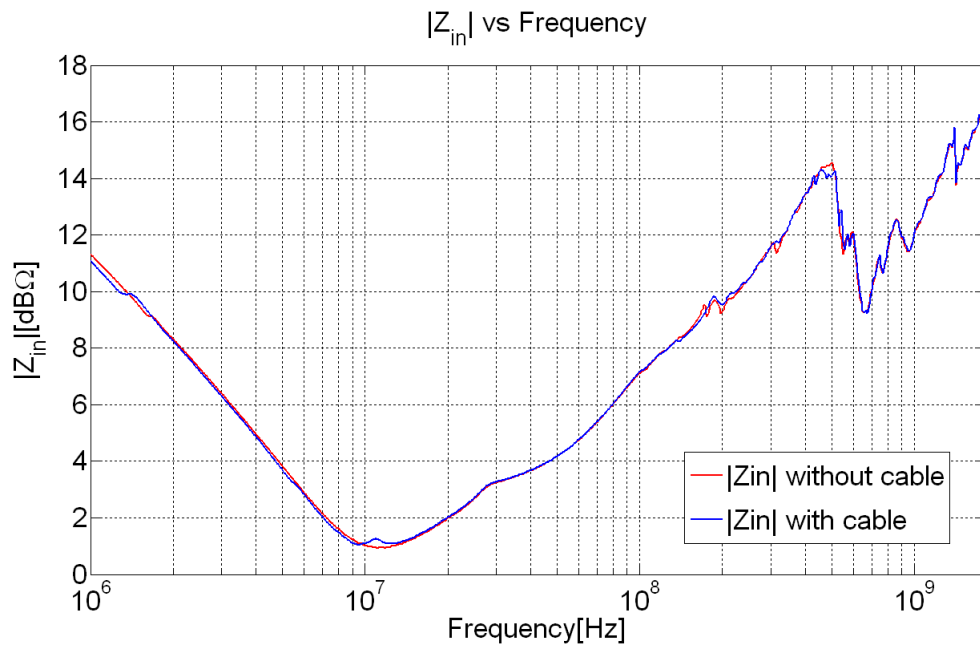


Figure 4.15. Input Impedance Seen from Inside the IGBT

4.2.3. IGBT Module to Cable Transfer Impedance. The transfer impedance between the cable and the IGBT was measured using the Fisher F-61 and F-65 current probes and a Vector Network Analyzer. The setup for this measurement is illustrated in Figure 4.14. To remove the effects of the current probe, the through calibration connection was setup the exactly the same as the measurements setup shown in Figure 4.5. Since the copper strap was used in the calibration, the band of frequencies which the

data could be trusted without the error from the copper strap being present included everything below 300 MHz. The plot of the measured transfer impedance is Figure 4.16. Below 300 MHz, the curves for the F-61 and its mate were nearly identical. However, when the curves passed the 300 MHz frequency, they start to vary more as seen previously when characterizing and testing the current probes. It can be seen from this plot that the transfer impedance is small around the 30 to 40 MHz range as expected.

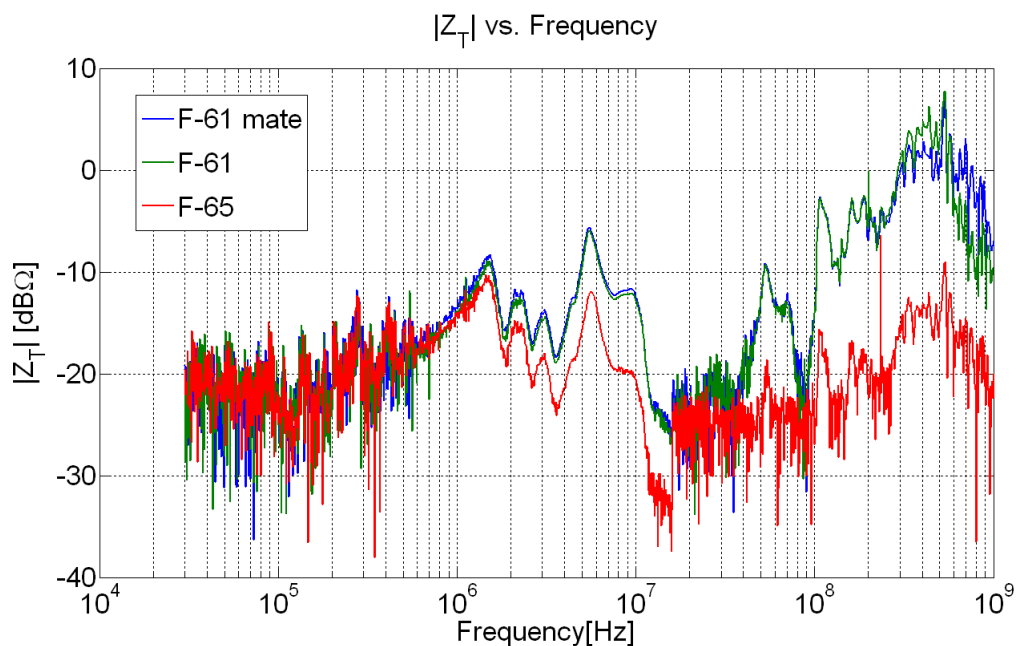


Figure 4.16. Transfer Impedance from IGBT to Cables

4.2.4. Transfer Impedance Outside the IGBT Module. Measurements from were made outside of the IGBT module to see what effects the IGBT module had on the transfer impedance. By tracing the current paths that leave the module and head to the motor, the ideal placement of the probe can be found at or just past pins 21 to 29. A triangular piece of copper was cut and soldered to the connection of the resistors just outside of the module. At this location, one of the legs of the triangle connected to all three phases on the board where the current left the IGBT and headed to the motor. The center conductor of a semi-rigid coaxial probe was soldered to the point of the triangle on the opposite side of the connection to the board as illustrated by Figure 4.17. The shape

of a triangle was used, because it more or less funnels the current into the desired location. Working at keeping the current from being forced from a wide path to a narrow path or vice versa minimizes any added inductance.

After the probe and triangle were connected, the board was attached back to the heat sink and the rest of the structure. The outer conductor of semi-rigid coaxial probe was connected to the reference of the system by attaching it to the heat sink using copper tape as shown in Figure 4.18. The full setup was completed and is shown in Figure 4.19.

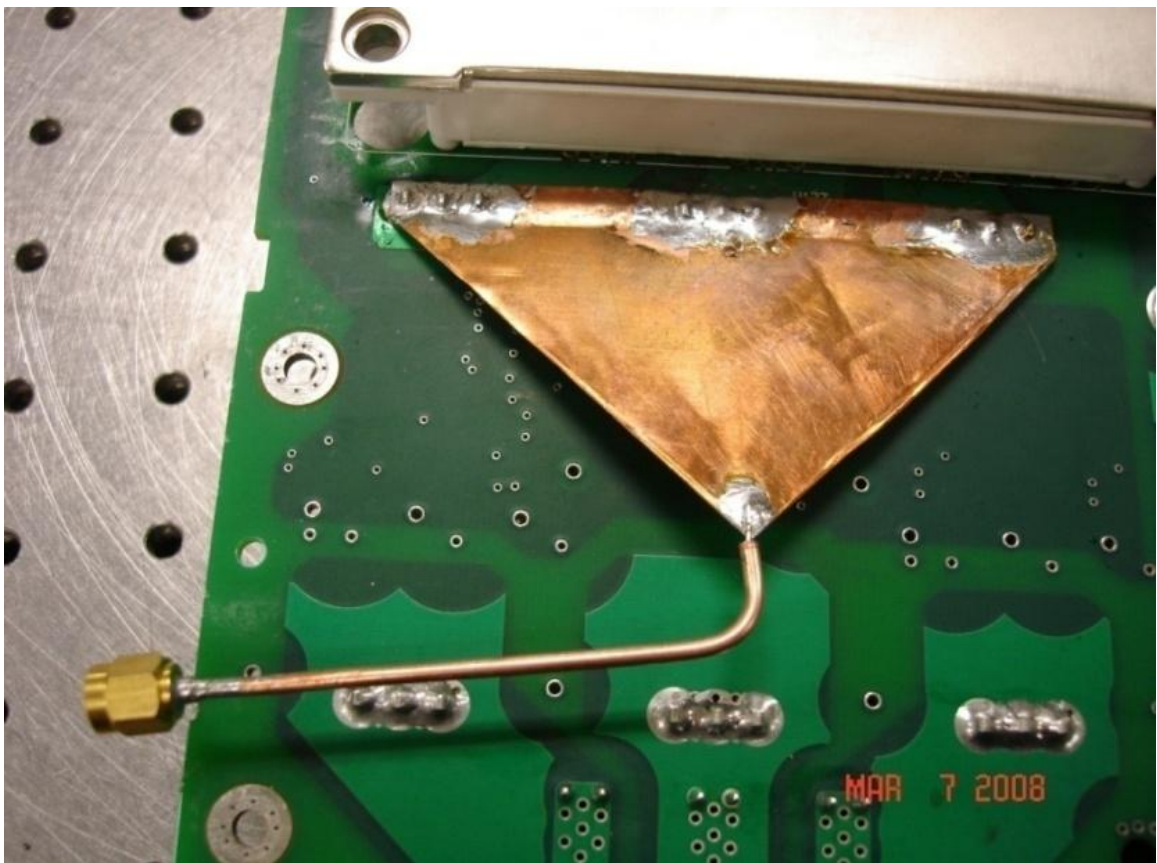


Figure 4.17. Copper Triangle Used to Connect the Center Conductor to the Three Phases and Reduce Inductance

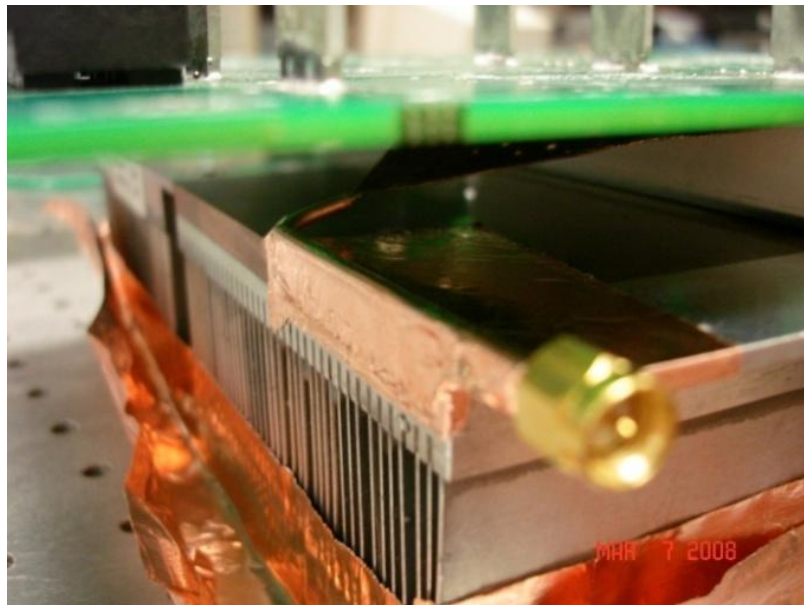


Figure 4.18. Copper Tape Was Used for Connection of Outer Conductor of the Probe to the Heat Sink

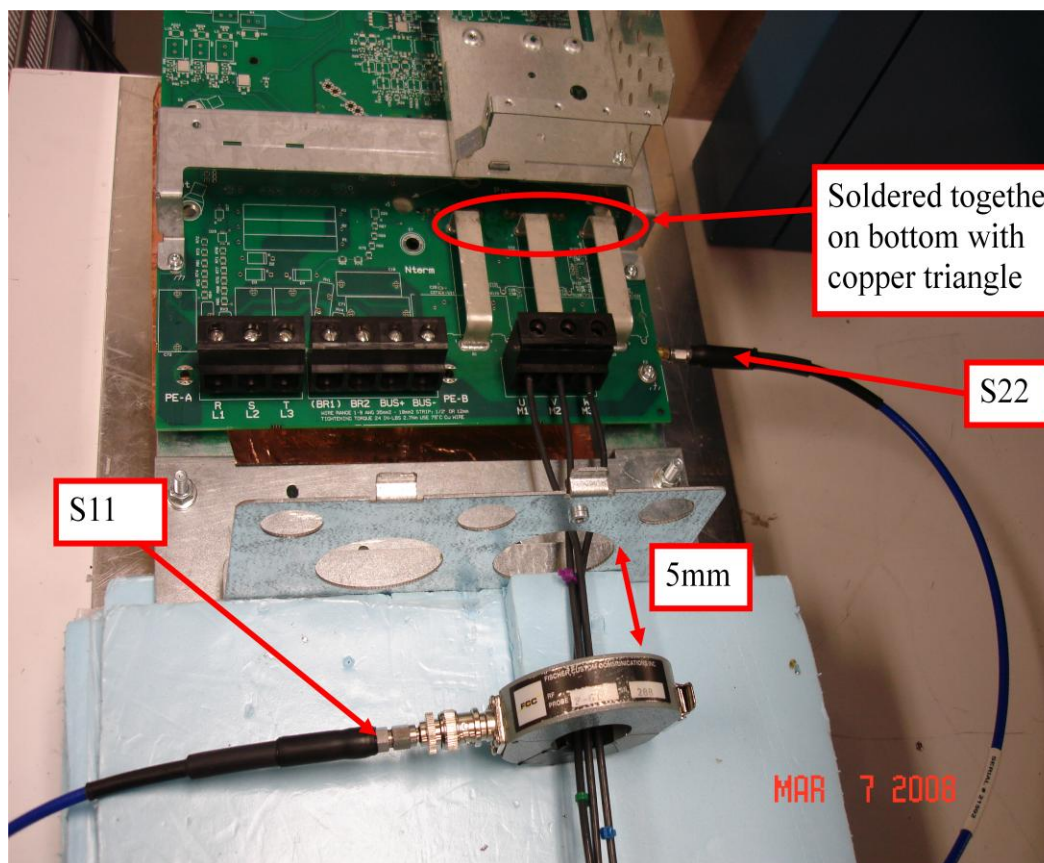


Figure 4.19. Measurement Setup for the Impedance Measured Outside the IGBT Module

The transfer impedance was measured using a Vector Network Analyzer, and the measurements are shown below in Figures 4.20 and 4.21. Figure 4.20 shows the magnitude of the transfer impedance where one zero can be seen close to 28 MHz and another close to 43 MHz. The impedance is allowed to go much higher outside of the IGBT module, since the capacitance added by the module is not playing a part in the measurements.

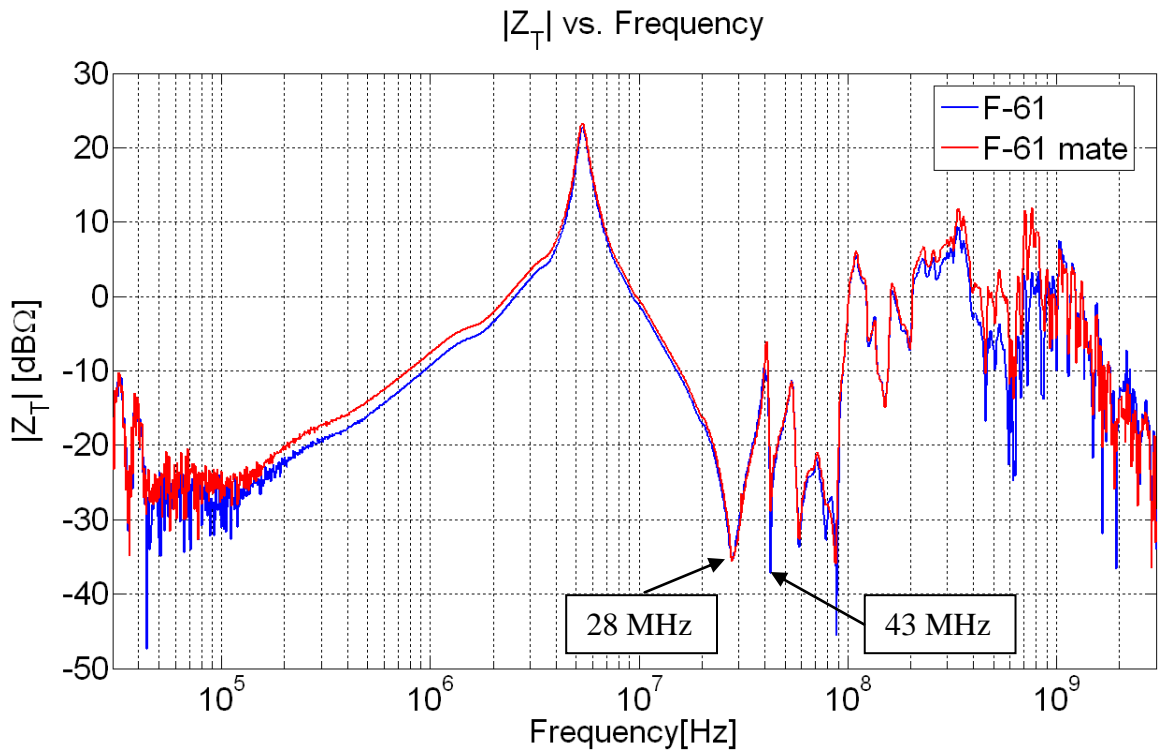


Figure 4.20. Transfer Impedance Magnitude Taken Outside of the IGBT Module

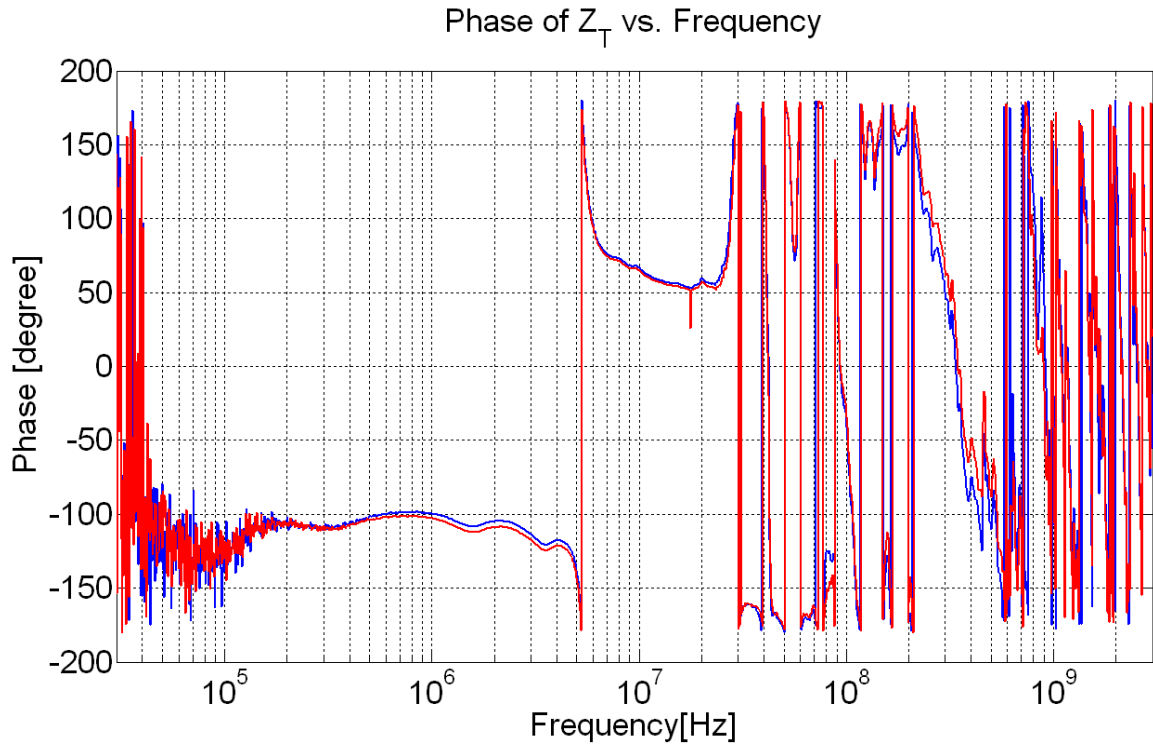


Figure 4.21. Transfer Impedance Phase Taken Outside of the IGBT Module

Measurements were performed on the cables and motor using an Impedance Analyzer to obtain the input impedance on the cable and Time Domain Reflectometer (TDR) to obtain the characteristic impedance of the cable and the exact length. Other measurements with the Impedance Analyzer and the TDR provided the values used in the equivalent circuit model. The data from the measurements and simulations along with the equivalent circuit model for the motor and cable can be found in the Appendix.

5. ENERGY DELIVERING SYSTEMS

The old saying of how a chain is only as strong as its weakest link also applies to electronic devices. When disrupting a device, the focus is finding where the weak point is in the circuit. All components used in circuits have voltage and current ratings, which is what this energy delivering system attempts to exceed. For most of the cases, the component which is being pushed past the limit is the microcontroller. Rather than destroying the microcontroller or causing it to go into latch-up, the energy delivering system uses coils to focus strong magnetic fields in specific locations on the device to guarantee these limits are surpassed inducing large voltages and currents inside the device. Achieving a maximum *emf* induced into a victim circuit requires maximizing the *B* field radiated by the culprit. Equation 19 explicates that if the magnetic flux density, *B*, is increased the *emf* will also be increased. The location of the maximum magnetic *H* field can also be found by using full-wave simulation tools. Since *B* is directly proportional to *H* as shown in equation 20, the maximum *B* locations will also be known. The *B* field applied to the victim is dependent on time and space. Therefore, the applied fields generated by the coils can be represented like that shown in equation 21.

$$\text{emf} = \oint_C \vec{E} \cdot d\vec{l} = -\frac{d}{dt} \int_S \vec{B} \cdot d\vec{s} \quad (19)$$

$$\vec{B} = \mu \vec{H} \quad (20)$$

$$\vec{B}_a = i_a(t) f_a(\vec{r}) \quad (21)$$

Finding the current applied, $i_a(t)$, requires SPICE simulations. The field applied as a function of space, $f_a(\vec{r})$, is found from the full-wave simulations.

5.1. PROTOTYPE

5.1.1. Simulations. Full-wave simulations were performed using the program CST Microwave Studio. The original serpentine coil was simulated with zero thickness to decrease the simulation time. The inductance associated with the thickness of the coil was considered negligible, since the main interested was finding the inductance associated with the loop formed by the coil array and the return. The model simulated can be seen in Figure 5.1.

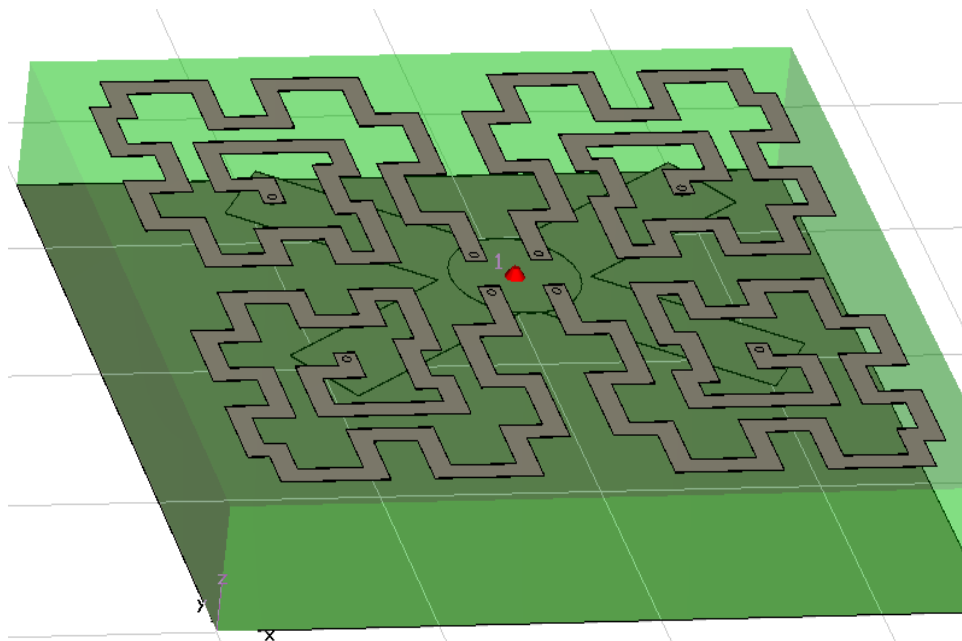


Figure 5.1. CST Model Used for Single Layer of Serpentine Coil

The bottom layer of the model was a reflector plane. The idea for this plane was to reflect the fields away from the device as well as shield the device. The plane was set one inch below the next layer which was the return plane. The return plane was in the shape of an X in order to keep the geometry symmetric. The length of each crisscross component was 65 millimeters from the center of the PCB to the end of the component. The 15 millimeters circular plane located 20 mils above the crisscross return plane was the power plane. 20 mils above the power layer was the serpentine coils with a trace

width of five millimeters. Vias with a diameter of 2 millimeters were used to connect the coil to the return and the power layers. After a time domain simulation was completed, the inductance was pulled from the input impedance curve of the coils 45.81 nH.

With some manipulation of Maxwell's Equations, it can be shown that the B field increases with the increase of current through the coils. Another layer of serpentine coils was placed above the first set of coils, because of the physics behind a solenoid and knowing that a PCB can have many layers. The vias that were used in the previous model were extended up to the second coil. This configuration made all eight coils in parallel. A part of the new model is shown in Figure 5.2.

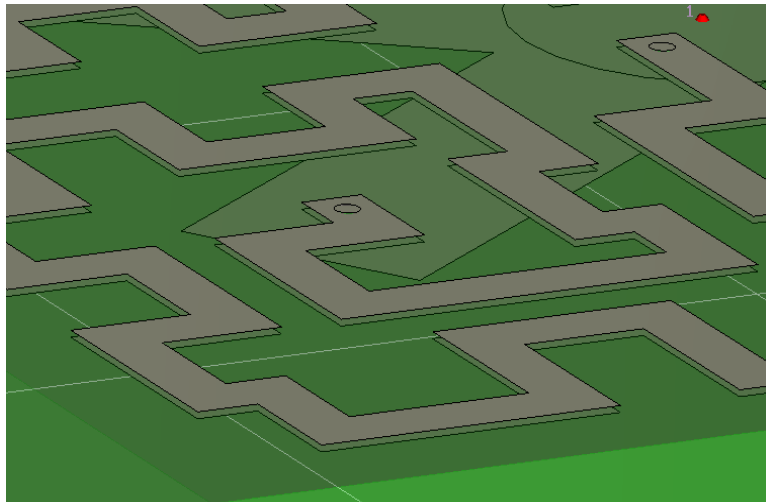


Figure 5.2. CST Model Used for Two Layers of Serpentine Coils

Doubling the layers decreased the inductance only a little to 44.42 nH from the 45.81 nH. Therefore, this extra layer makes this model more desirable, since it allows an increase in the current which increases the magnetic fields. Decreasing the inductance further was accomplished by increasing the diameter of the vias and making it the same size as the width of the coil traces. The smaller vias made the inductance of the two layer model come to 44.42 nH, while the larger vias lowered it to 43.67 nH. The two layer model now looked like that portrayed in Figure 5.3.

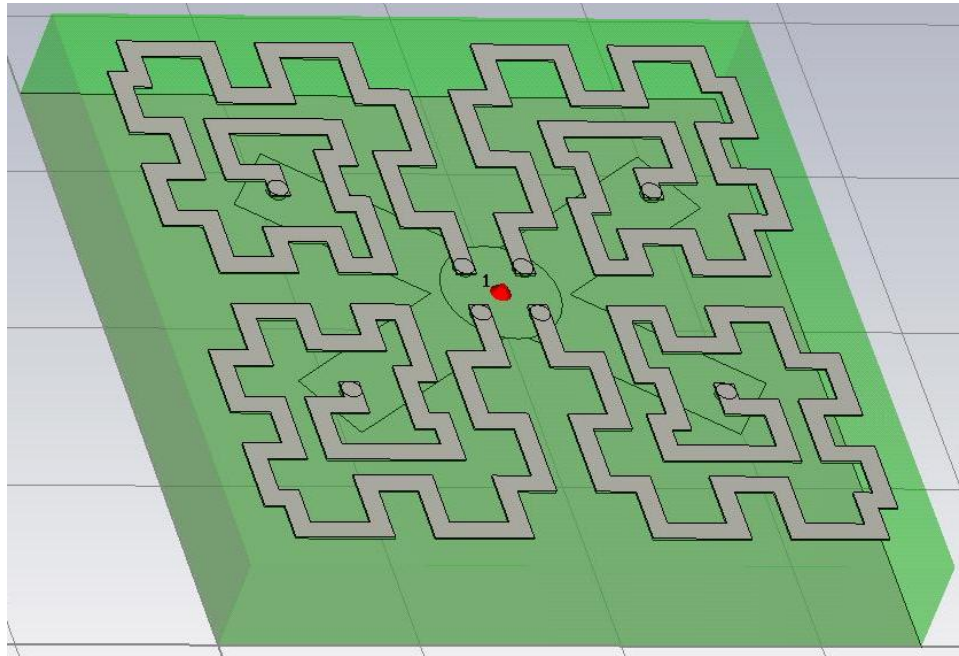


Figure 5.3. CST Model Using Two Coil Layers and Larger Vias

Field plots were extracted from CST to get a good feel for how the magnetic fields looked when the serpentine coil was excited. The magnetic fields seen when a cut plane is placed vertically through two of the coil's centers is shown in Figure 5.4. While one coil pushed the fields through, the other coil pulls the fields. This is what makes the serpentine array work better than that of a single loop. The serpentine coil keeps the inductance low, and the array makes the coils work together to create a stronger field distribution. It can also be seen from Figure 5.4 that the reflector plane binds the fields to the area between the coil and the reflector plane. The closer the reflector plane is moved to the coils, the more restricted the fields become. If the reflector was to be placed on the back of a 62 mil PCB, it would pinch and lower the strength of the fields.

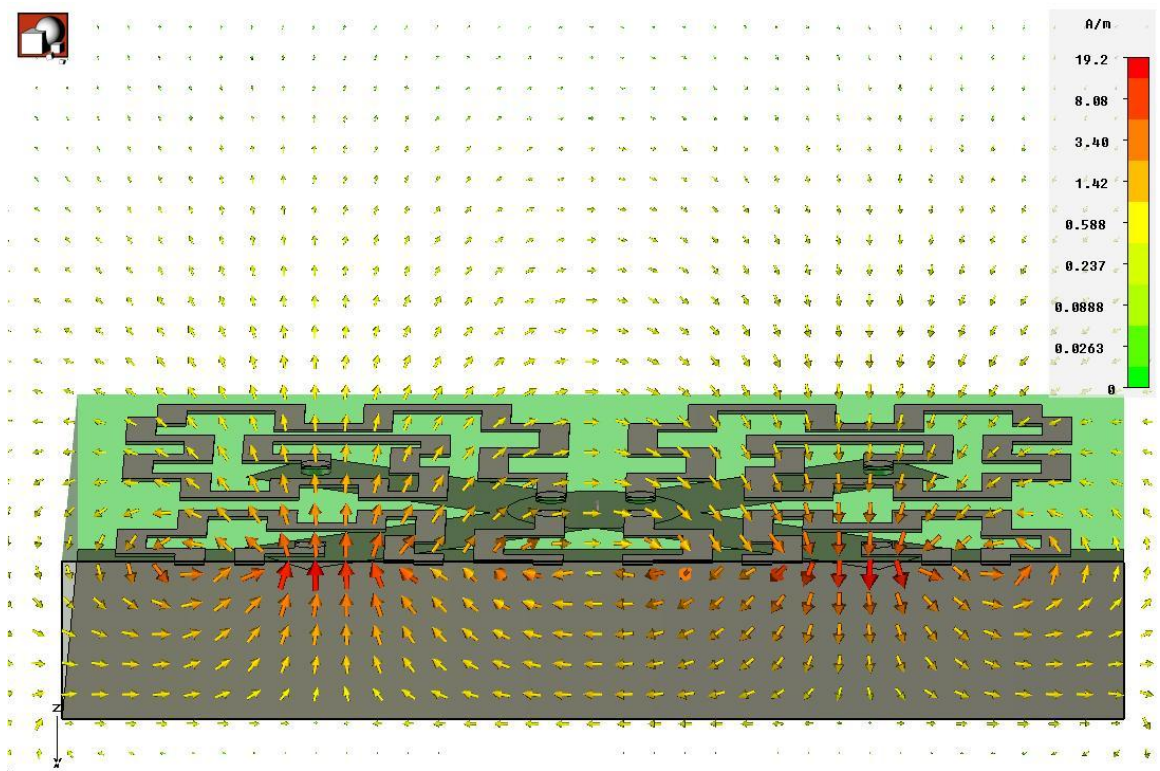


Figure 5.4. Two Layer Model’s Magnetic Fields Seen with a Cut Plane Placed in Model

One of the intended purposes for the simulation was to find the maximum field strength from each model and its location. Figures 5.5 and 5.6 both show the magnetic fields at an inch away from the coils. Figure 5.5 shows that for the two layer model the maximum value is 0.704 A/m, while Figure 5.6 shows that the maximum value is 0.307 for the one layer model. These simulations shows that the fields more than double when we add another layer.

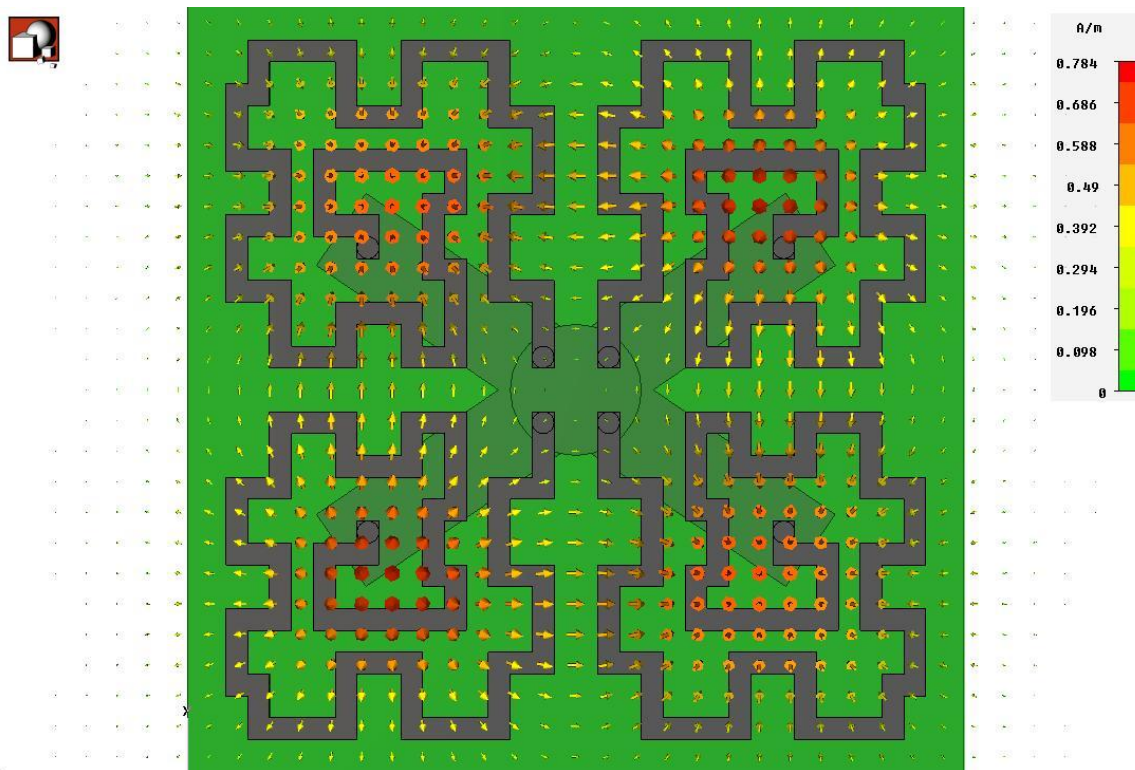


Figure 5.5. Two Layer Model's Magnetic Fields Seen at an Inch Away from the Coils

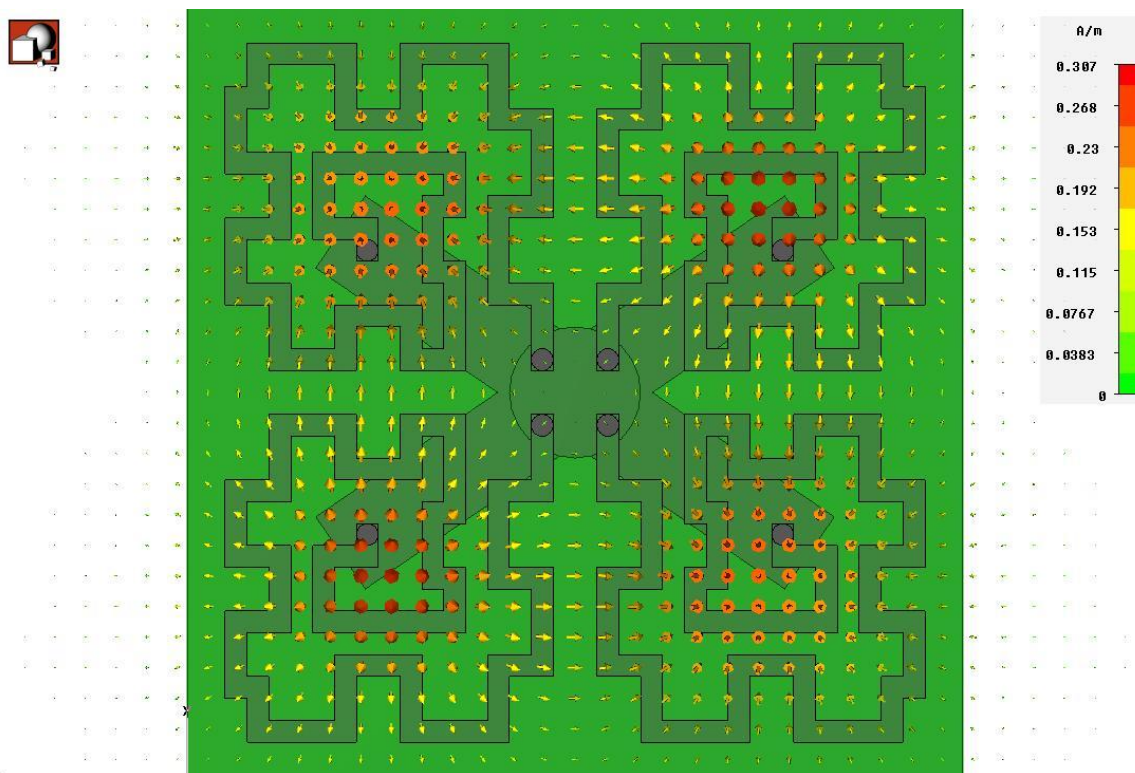


Figure 5.6. One Layer Model's Magnetic Fields Seen from an Inch Away from the Coils

After the inductance from the coils had been calculated by CST, they were inserted into a PSPICE model to find the current through the coil. The design called for two 34 nF capacitors in parallel which charge up to 40 kV and then discharged across the coils. The use of one and two 34 nF capacitors was examined for this model. The inductance of the transmission line was also varied from 10 nH to 100 nH, since the length of the cable was unsure. In the model shown below in Figure 5.7, the capacitor bank is C1. The resistance and inductance of the cable is R1 and L1, respectively. L2 was the inductance associated with the coils being pulsed. A switch, U1, has also been added to make sure PSPICE simulates a capacitor discharging when time is equal zero.

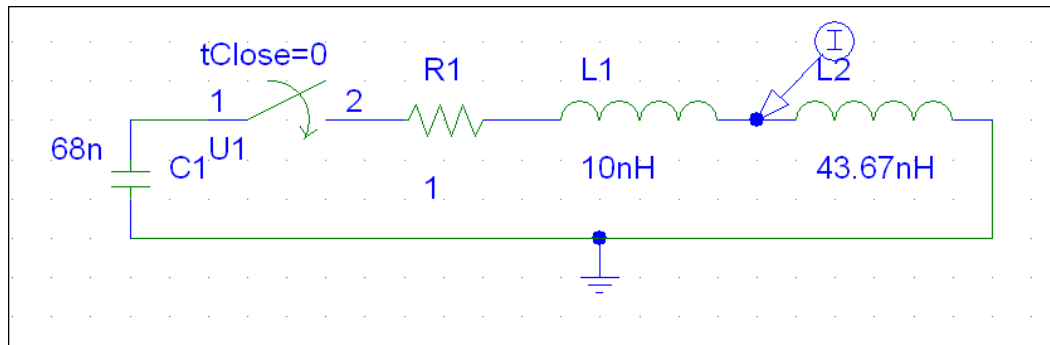


Figure 5.7. PSPICE Model

The current verses time through the two layers of serpentine coils is shown in Figure 5.8 for the two coils. No matter what size of inductance is introduced by the coil (43 nH, 44 nH, 50 nH), the current had the same set of curves but with different values. For both one and two layers of coils, the maximum current was nearly 14.2 kA. For this simulation, the one circuit element that will make the biggest change in the current is the resistance in the line, R1. Comparisons were also made between the one layer case and the two layer case. The difference between these was nearly negligible as shown below by Figure 5.9. For this figure, the inductances from the larger diameter via simulations were used.

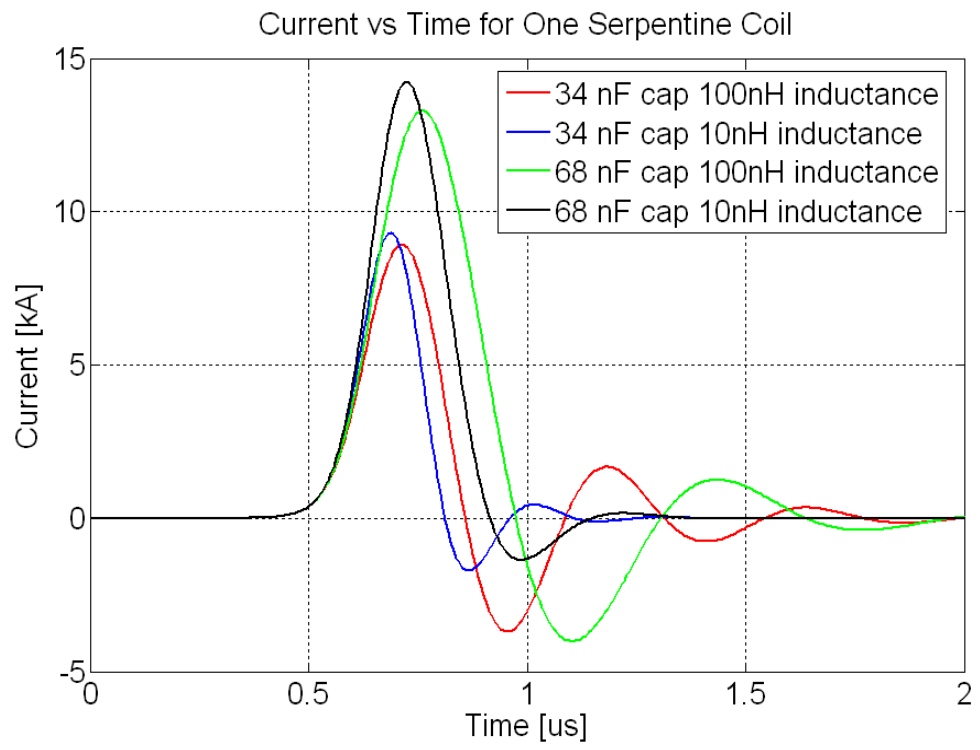


Figure 5.8. PSPICE Results for Two Coils Comparing the Values of C1 and L1 Over Time

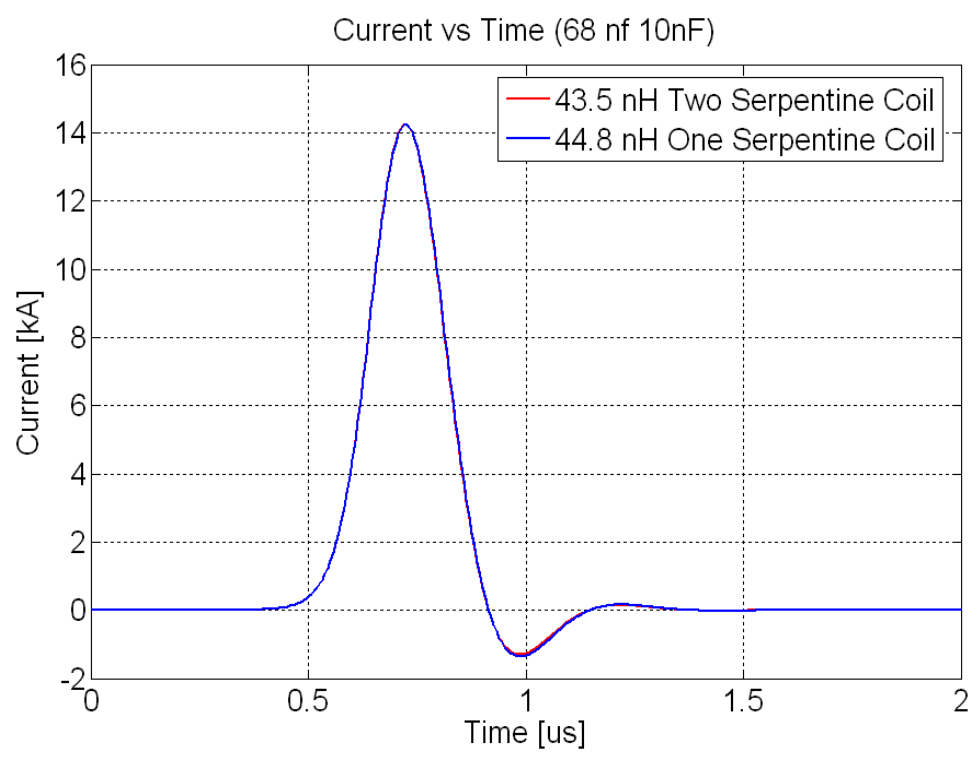


Figure 5.9. Comparison for One and Two Layers of Coils

5.1.2. Manufacturing the Printed Circuit Board. A PCB was manufactured after the model had be simulated and performed well. However, the model was changed when manufacturing the boards. The manufactured board was 62 mils thick and contained only two layers. The coils were on the top layer and the return was on the bottom layer. The power layer was more or less moved to the same layer as the coils. It consisted of a pad with a radius of an inch which covered the start of the coils. A 1/2 inch hole, large enough for the bolt used to attach the power to the coil, was cut out of the center. Because the power connection was placed in the center, the return had to be modified. The return became a 300 mil 'U' shaped trace on the bottom of the board. The return layer contained a hole to bolt the on strap which connects the cable to the coils. A reflector plane was not part of the board. It could be added later by spacing it with foam and using copper tape for the plane. The manufactured board is illustrated in Figure 5.10 and 5.11. The bottom layer is Figure 5.10, and the top layer is Figure 5.11.

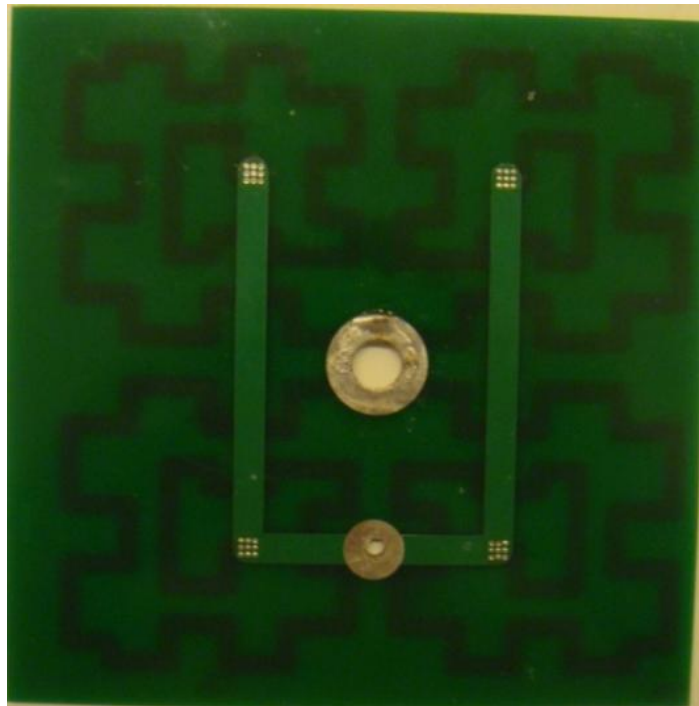


Figure 5.10. Back Side of Manufactured PCB

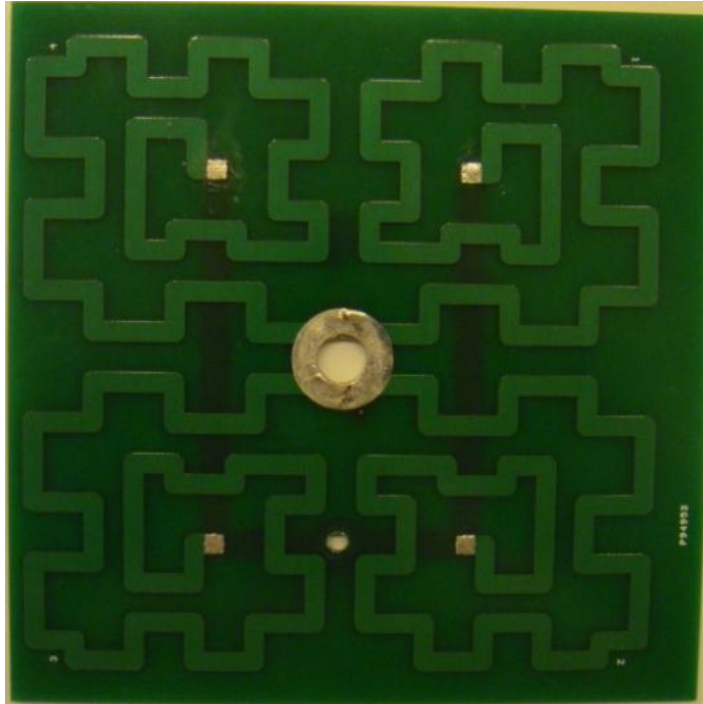


Figure 5.11. Front Side of Manufactured PCB

This board proved to have problems when energized by the high voltage pulser. The coils and return layers turned out to be too close, which caused electrostatic discharge to occur. This was mainly at the edges of the board and where the hole was made to connect the reference. Therefore, the model was changed to remove these problems.

5.2. NEW ONE LAYER DESIGN

Since there were problems with the actual structures performance, the design was then confined to controlling the ESD. Before performing any more simulations, this was resolved.

5.2.1. Changes Made to PCB to Eliminate Electrostatic Discharge. The electrostatic discharge was overcome by making sure the return trace maintained a distance of 1200 mils or more from the center pad where the high voltage power was attached. The return trace was also rotated 90 degrees to create the shortest possible path. If the trace was left in the same orientation, the trace would have to look like that in

Figure 5.12. After the changes were made, the return trace looked like that illustrated in Figure 5.13.

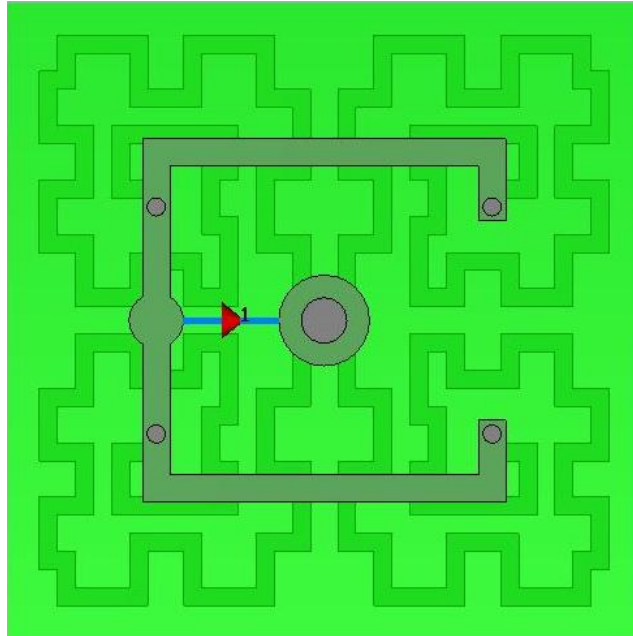


Figure 5.12. Change in Model without the Turn of 90 degrees

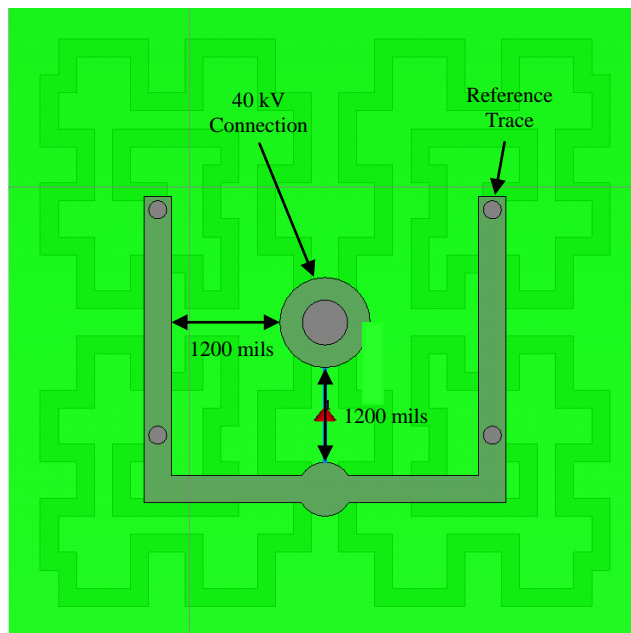


Figure 5.13. Solution to the Electrostatic Discharge Problem from the Power Connection to the Return Trace

To solve the problem where connection of the return was bolted to the PCB, the hole was eliminated completely, and a copper strap was soldered to the return trace. The discharge at the sides of the board was eliminated by separating the two planes. To do this effectively, two boards were made. One board contained the coils, and the other contained the reference trace. By making two separate boards, it gave the flexibility of changing the separation between the coils, as well as allowing for another layer of coils to easily be added later. Figure 5.14 portrays the difference between the previous PCB return trace and the modified one.

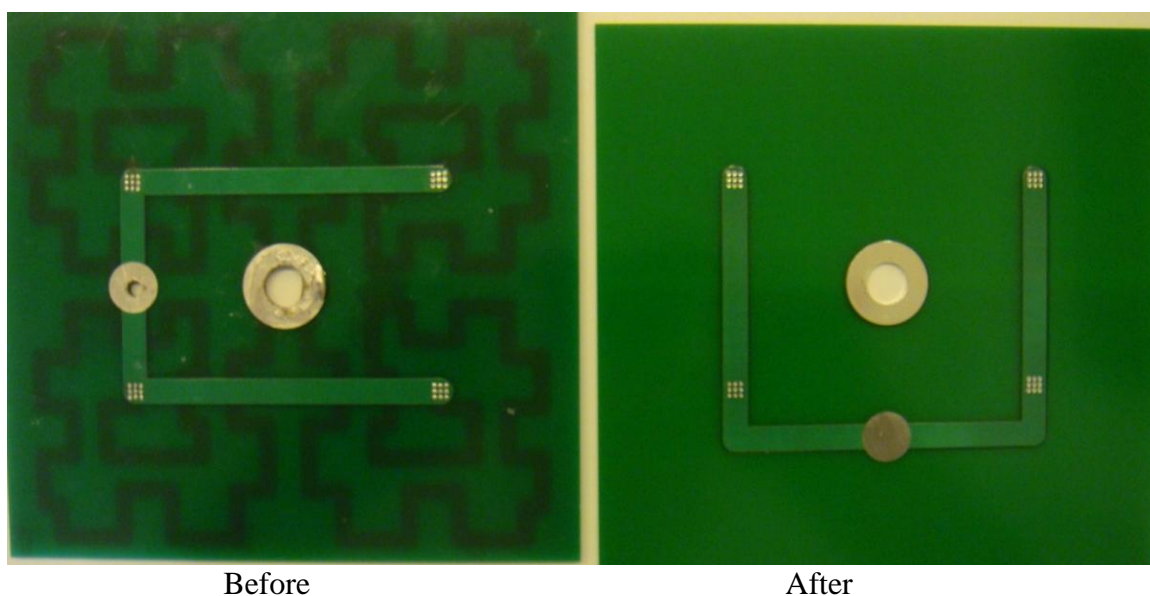


Figure 5.14. Return Trace Changes

5.2.2. CST Simulations Made for New Design. Now that the return trace had been redesigned, the full design was also examined. The hope was to keep the planes as close together as possible to maintain the desired low inductance. The EDS was to be controlled by using two sheets of FR4 for the separation which was each 60 mils thick. The geometry for the simulations looked like that in Figure 5.15. The left picture was the top and the right picture shows the bottom. The field distribution is portrayed in Figure 5.16.

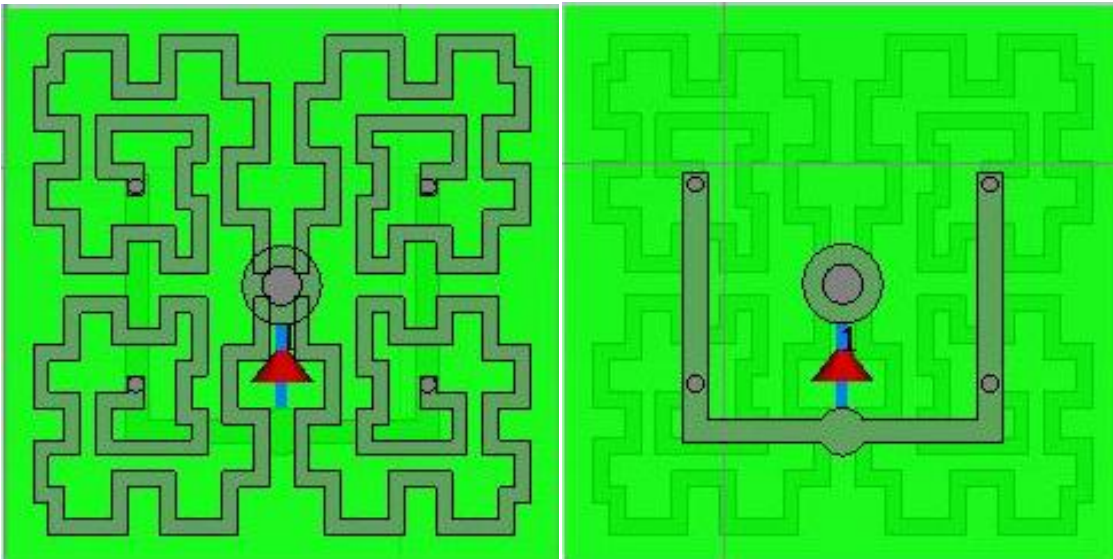


Figure 5.15. CST Model Used for Simulation of New Design

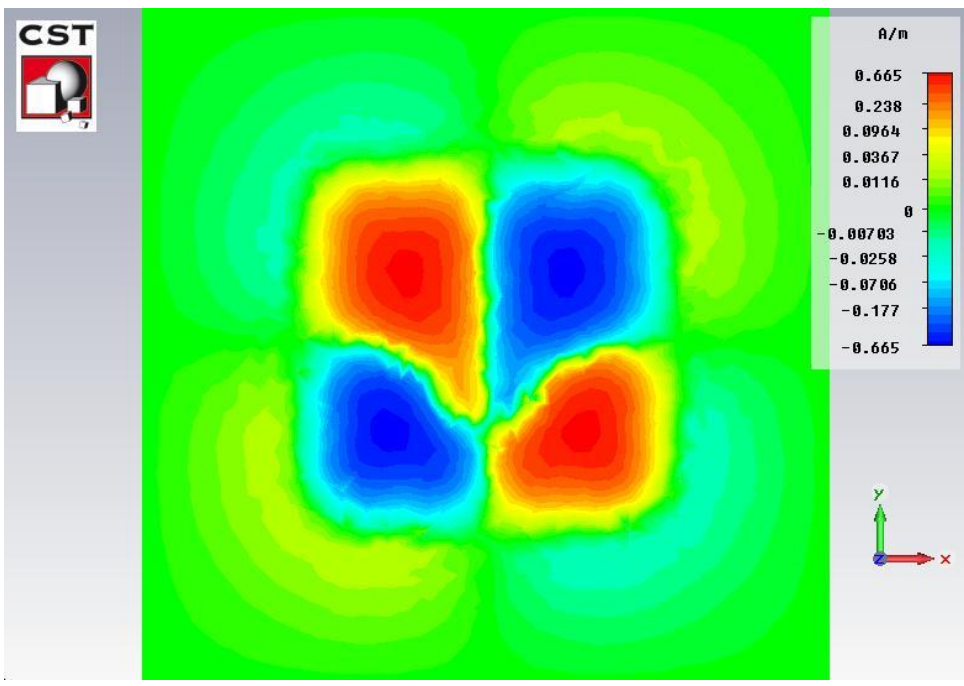


Figure 5.16. Modified Coils Field Distribution at an Inch Away from Coils with 240 mil Separation Between Coils and Return Plane

The inductance calculated by CST was 101.88 nH and would only get larger as the coils and return trace moved further away. However, the fields became distorted and lost some of its strength as seen in Figure 5.16. The return trace became a factor, since it

was no longer symmetric like the model in Figure 5.1 and 5.3. This caused the currents to return to the reference connection from the pulser at different times. Since the system operated at low frequencies, it was thought that this would not occur. However, these assumptions proved to be wrong when simulating a 2 MHz pulse in CST. To make the field distribution appear as it should, the current path was forced to be made longer, since the frequency of the input was fixed. Simulations by CST show that when this distance is increased to at least 750 mils or more, the structure becomes electrically long and the field distributions are again uniform. Field distributions for $\frac{3}{4}$ of an inch and one inch are given by Figure 5.17 and 5.18. The only down fall to making the separation larger is the increase in inductance. For a separation of $\frac{3}{4}$ of an inch, the inductance is 116.41 nH, and the inductance is 119.48 nH for a separation of one inch. This increase makes very little difference in the current going through the coil.

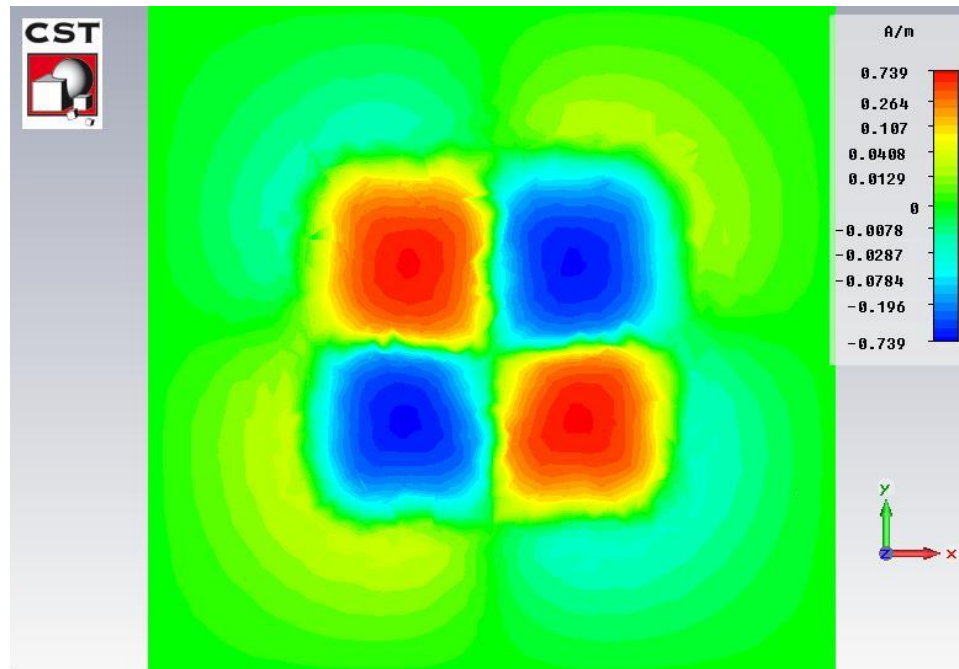


Figure 5.17. H-field Distribution at an Inch Away from Coils with a Separation of $\frac{3}{4}$ of an Inch Between Layers

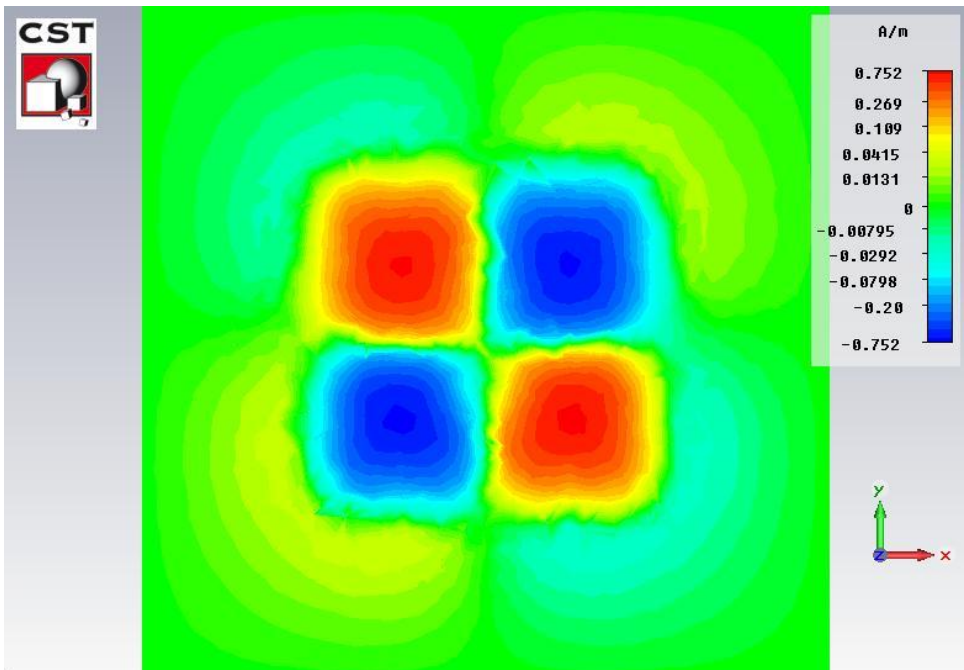


Figure 5.18. H-field Distribution at an Inch Away from Coils with a Separation of an Inch Between Layers

5.2.3. Current Calculations Performed in Matlab. The current calculations used 34 nF for the capacitance, since the objective was to calculate the current going through the coils using the setup at the UMR EMC Laboratory. An estimated resistance of one ohm was used to complete the model. PSPICE was used at first to find the currents, but the simulations required a long time in order to get the lower frequency spectrum. Therefore, the analytical equation was derived from the schematic shown in Figure 5.19.

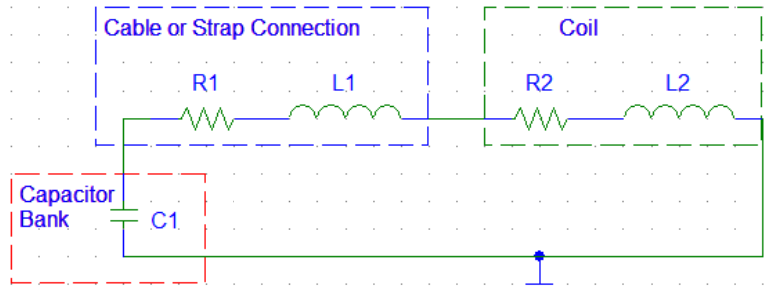


Figure 5.19. Equivalent Circuit

R1 was set to one ohm, and R2 was set to zero. L2 was changed to match the inductance value calculated by CST for each separation distance. L1 was calculated by hand using the equation 22.

$$L_{cable} = 5.08 \ln\left(\frac{r_s}{r_w}\right) \text{ nH/in} \quad (22)$$

The radius of the shield, r_s , and the radius of the wire, r_w , was measured to be 0.61 inches and 0.315 inches, respectively. The total length of the cable was measured to be 57 inches. Therefore, the total calculated inductance for the cable was 191.37 nH. Since this was close to half of the inductance value of the coils, the voltage drop across the coils was nearly 1/3 of the total voltage. As a result, the power delivered to the coils was approximately 1/3 the total power provided by the capacitors. To ensure more power was delivered to the coils the cable was shortened to 25.875 inches. This lowered the cable inductance to 86.87 nH which was the value used in the current calculations. Figure 5.20 shows the different currents going through the coils with respect to time, and Figure 5.21 shows the different currents with respect to frequency. It can be seen that the current magnitude changes very little with a separation of 240 mils, 750 mils, and an inch. The maximum values are placed in the legend of each plot. The resonance frequency for this geometry will vary a little based on the inductance, but it will be close to 2 MHz. For the one inch separation which was used, the resonance frequency is at 1.82 MHz.

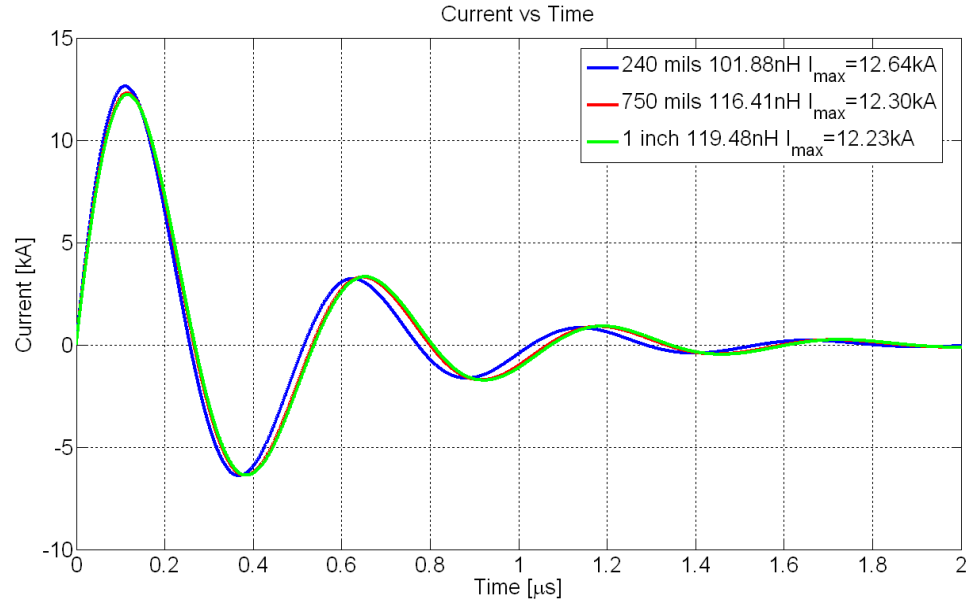


Figure 5.20. Current Through Coils vs. Time

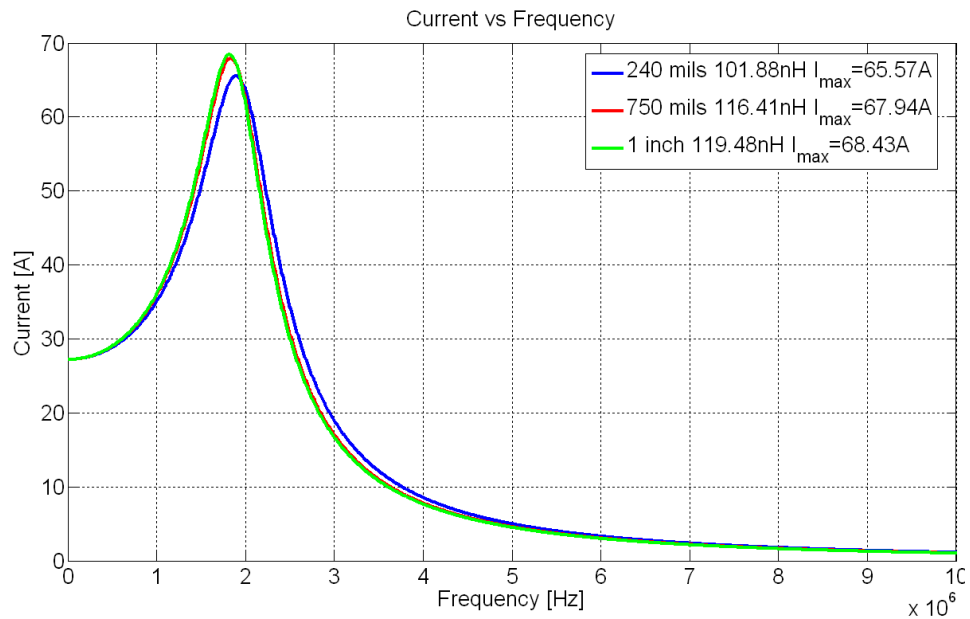


Figure 5.21. Current Through Coils vs. Frequency

The current was calculated by deriving the differential equations of the circuit and solving for equation 23.

$$i = A_1 e^{s_1 t} + A_2 e^{s_2 t} \quad t \geq 0 \quad (23)$$

Basic circuit analysis was used to find s_1 and s_2 . R_1 and R_2 were added together to create the variable R . L_1 and L_2 were also added to create L . The variables s_1 and s_2 are given by equations 24 and 25.

$$s_1 = \frac{1}{2} \left(-\frac{R}{L} + \sqrt{\left(\frac{R}{L}\right)^2 - \frac{4}{CL}} \right) \quad (24)$$

$$s_2 = \frac{1}{2} \left(-\frac{R}{L} - \sqrt{\left(\frac{R}{L}\right)^2 - \frac{4}{CL}} \right) \quad (25)$$

Variables A_1 and A_2 were derived and are shown in equations 26 and 27.

$$A_1 = \frac{V_{in}}{L(s_1 - s_2)} \quad (26)$$

$$A_2 = \frac{V_{in}}{L(s_2 - s_1)} = -\frac{V_{in}}{L(s_1 - s_2)} \quad (27)$$

Variables A_1 and A_2 were simplified by finding the solution to $s_1 - s_2$ shown by equation 28.

$$s_1 - s_2 = \frac{1}{2} \sqrt{\left(\frac{R}{L}\right)^2 - \frac{4}{CL}} \quad (28)$$

Substituting equation 28 it into equation 26 and 27 defined a new variable, A , given by equation 29.

$$A = \frac{V_{in}}{\sqrt{R^2 - \frac{4L}{C}}} \quad (29)$$

When the new variables were substituted into equation 23, the solution gave the equation for the current and shown below in equation 30.

$$i = Ae^{-\left(\frac{R}{2L}\right)t} \left(e^{\left(\frac{1}{2}\sqrt{R^2 - \frac{4L}{C}}\right)t} - e^{-\left(\frac{1}{2}\sqrt{R^2 - \frac{4L}{C}}\right)t} \right) \quad (30)$$

Equation 30 was entered into Matlab and used to find the currents flowing through the coils. The equations were also derived to find which components were the biggest factors in maximizing the current. All the exponentials in equation 30 are bound between one and zero. The dominating factor of the current magnitude is A which is defined in equation 29. V_{in} is one dominating factor which is directly proportional with the current, but is bound by the spark gap switch and the capacitor ratings. A is its largest when L and R get smaller and C gets larger. R is the resistance in the geometry and is not easily changed. Since C is more or less fixed, L is the only variable that can be changed.

5.2.4. Manufacturing New PCB Coil Design. From the simulations in the previous section, it proved to be important that the structure maintained a separation of at least 750 mils between the two PCBs. This separation was to help the fields stay uniform and eliminate the possible chance of ESD. The separation of an inch was used, since a separation of 750 mils shown the fields starting to change. The spacing was maintained by using four pieces of blue insulation foam which was a quarter of an inch thick for each piece. The coil PCB was placed on top of the foam stack, and the return was placed on bottom of the stack. Clamps were used to reduce the air between the four pieces of foam by squeezing the two PCBs and foam together while wires were placed through all the vias and soldered. The wires connected the two layers electrically as well as mechanically.

As stated before, the ground strap was soldered on to the return trace, so a little bit of the film on top of the return trace was scratched away to expose the copper for soldering. The strap was wider at the connection to the return trace and tapered as it got closer to the cable connection. When the cables were connected, some copper wool was used to make a better connection. Figure 5.22 illustrates the finished geometry, and Figure 5.23 shows the new setup.

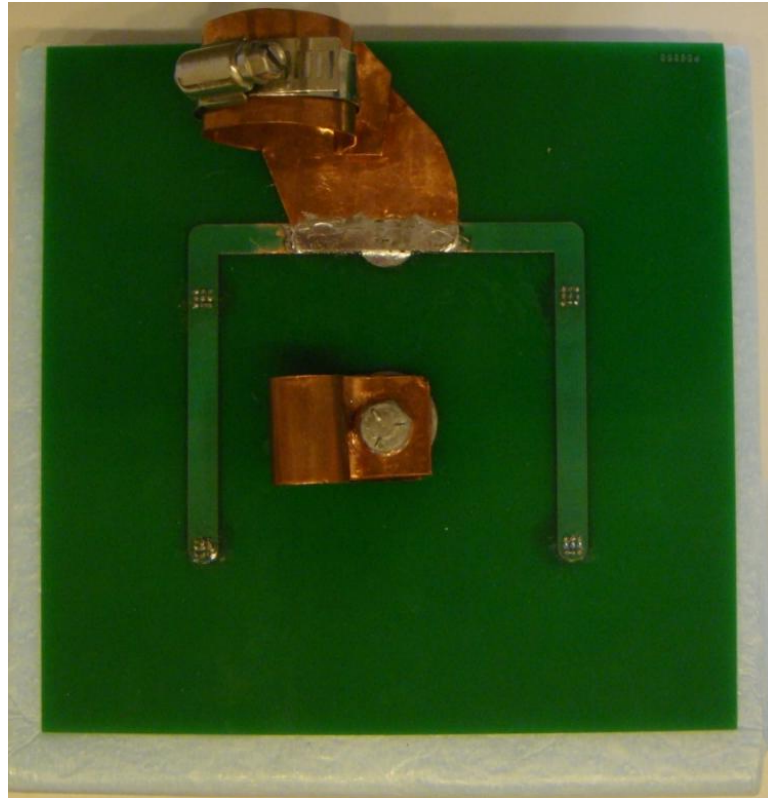


Figure 5.22. New PCB Design

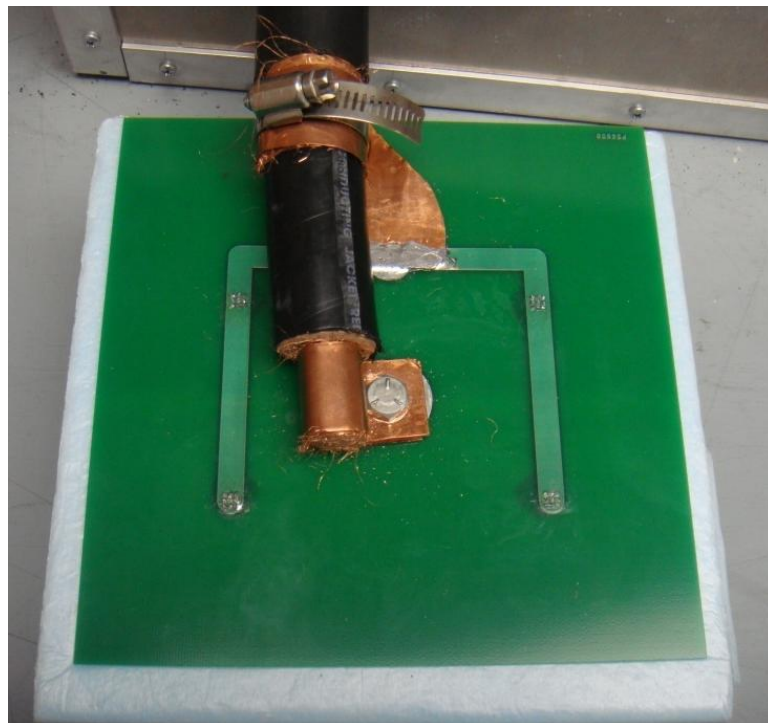


Figure 5.23. New Setup

APPENDIX

This appendix is composed of a detailed report given to Rockwell Automation by a three person senior design team from the University of Missouri-Rolla and a four person senior design team from Rose Hulman Institute of Technology. As a graduate student mentor to these students, I instructed them on the proper method of taking measurements and recording data, taught them the proper usage of simulations tools, and how to compare and make sense of the simulations and measurements. This Appendix shows the success of this project and gives background to areas in this thesis.

Missouri University of Science & Technology
&
Rose-Hulman Institute of Technology

Departments of Electrical and Computer Engineering

EMC Modeling of Rockwell Automation AC Drive

May 6, 2008

Submitted by

Daniel Baker
Andrew Gawlik
Gareth Shields
Chris Valenta
Dr. Ed Wheeler

Matt Halligan
Igor Izyumin
Clint Patton
Jason Phillips
Dr. Jim Drewniak

Abstract

Senior design teams from Rose-Hulman Institute of Technology and Missouri University of Science and Technology have investigated and modeled the electromagnetic compatibility (EMC) of an AC motor control system. Circuit geometries have associated parasitic elements that can provide common-mode current paths and thus significantly contribute to radiated emissions. Using computer simulation and laboratory measurements, circuit models can be augmented so that non-intended parasitic paths are included in the system models.

The insulated gate bi-polar transistor (IGBT) drive module is responsible for the majority of emissions due to large, fast-switching currents. This rich spectral content is coupled into the cables and motor where it is effectively radiated. Modeling the IGBT package required extracting parasitic capacitances and inductances from the geometry in the package. The package schematic was then updated with the parasitics to determine common-mode current coupling paths.

The motor was modeled by a high frequency circuit using an impedance analyzer and network analyzer to take common- and differential-mode measurements.

The cable length and frequencies of operation dictated it be modeled as a loaded transmission line. The characteristic impedance was measured with time domain reflectometry so a transmission line model could be developed. The effect of ferrites on cable impedance and emissions was also investigated by taking measurements with and without ferrites.

Missouri University of Science and Technology Teams

IGBT: Igor Izyumin and Jason Phillips

Igor and Jason worked together on modeling, measurements, and simulation of the IGBT module. This work involved 3D modeling in CST and Solidworks, as well as CST, Q3D, and ADS simulations. They also worked on measuring the IGBT module capacitances and inductances. This work required preparing the module, performing calibration and fixture compensation, and recording, processing, and interpreting the measured data. In addition, they co-authored weekly progress report presentations for meetings with Dr. Drewniak, RHIT, and Rockwell Automation.

Motor and Cables: Matt Halligan

Matt worked on modeling, measurements, and simulation of the motor and cables. This work involved modeling in PSpice, as well as Matlab, and PSpice simulations. He measured the common-mode and differential-mode impedance of the induction motor, characteristic impedance and time delay parameters for the shielded and unshielded cable. Additional measurements performed were input impedance measurements of the motor and cables, and common-mode current measurements. This work required creating extensive custom lab setups with the motor and cables, performing calibration of instruments, and recording, processing, and interpreting the measured data. In addition, he authored weekly progress report presentations for meetings with Dr. Drewniak, RHIT, and Rockwell Automation.

After a complete academic year of research, the IGBT and Motor and Cables teams have performed well, meeting most of the requirements set out in the proposal for this project. For an undergraduate research team, the quality of the research has far exceeded that of an average undergraduate team. The research presented in this report is on the graduate level. Therefore, by going above and beyond the expectations for a senior design team, it is believed that Igor, Jason, and Matt should get an 'A' for their efforts in senior design.

Table of Contents

Abstract	76
Table of Contents	80
Introduction.....	81
Participants.....	81
Problem Statement	81
Objectives	83
Overview.....	83
Summary of Achieves.....	86
IGBT Module Modeling	86
Motor and Cables	98
Deliverables.....	128
Recommendations.....	128
Conclusion	128
Appendix A: References	130

Introduction

Participants

The Electromagnetic Compatibility Laboratory at Missouri University of Science and Technology (Missouri S&T) is one of the world's leading groups in EMC and SI research and application. The EMC Laboratory and its industrial partners in the associated EMC consortium work in solving fundamental EMC design issues and then sharing these solutions among all participating partners [A7].

Rose-Hulman Institute of Technology is a premier institution of undergraduate engineering, science, and mathematics education [A6]. Their faculty has collaborated with the Missouri S&T EMC Laboratory for several years and is currently working on a joint NSF CCLI Phase II project with the Missouri S&T EMC Laboratory.

Rockwell Automation is a leading manufacturing of motor drives that control the speed, torque, timing, and acceleration of motors in industrial applications ranging from conveyors to roller coasters across a wide range of power configurations [A1]. Rockwell Automation's engineers are currently developing the next generation AC motor controls which are code named RHINO with a planned release date in the spring of 2008.

Problem Statement

Current motor drives (see Figure 1) such as the RHINO and legacy PowerFlex products have experienced electromagnetic interference (EMI) issues which need to be addressed. These issues have required making adjustments to circuit board layouts, tweaking circuit parameters and re-designing certain critical components, and adding filters (capacitors, chokes, etc.) in order to meet FCC or CISPR conducted and radiated emission requirements [A2] [A3]. Motor drives have significant potential as emission sources, since IGBTs switch large currents relatively quickly. This leads to the presence of strong time-varying electromagnetic fields [A4]. The design of the motor control systems must limit these emissions while at the same time allowing robust operation. The geometry

associated with the design and operation of the drives is expected to play a pivotal role in their EMC performance.

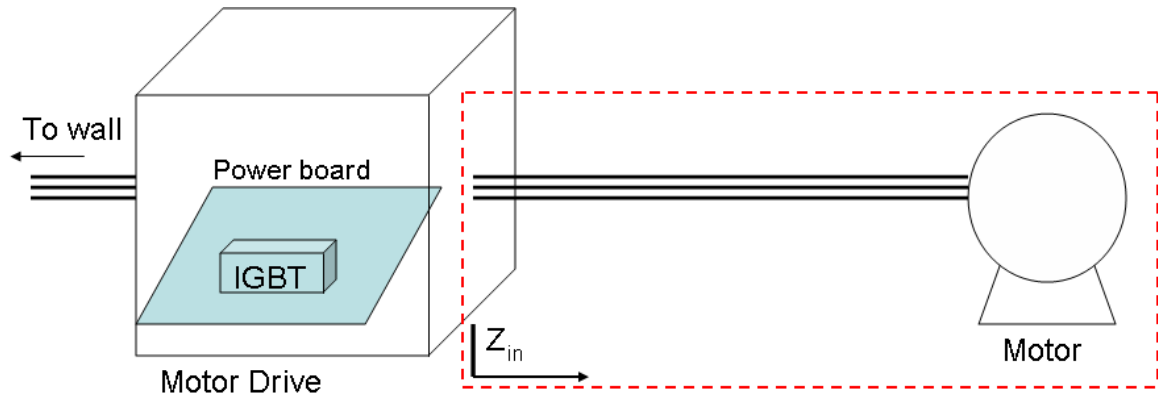


Figure 1- System Layout

To address some areas of concern regarding EMC in their present motor drives, Rockwell Automation engineers have added ferrite cores, adjusted ground paths, and modified metal enclosures. While these techniques often effectively reduce emissions to allow compliance, they add considerable cost and product delays. One of the goals in this project is to allow Rockwell Automation engineers to more effectively include EMC early in their designs.

Modeling the coupling paths in a device before production can provide insight into the electromagnetic behavior of the device. It is important that engineers appreciate how geometries affect the electromagnetic behavior of the device as they develop schematics and consider layout options. The circuit geometry will have associated parasitic elements (inductances and capacitances) that can provide common-mode current paths and thus contribute to significant radiated emissions [A5]. Using computer simulation and laboratory measurements, circuit models can be augmented so that non-intended paths which result from the presence of these parasitic elements are included in the system models. When engineers have access to the complete circuit, including the parasitic

elements, they can identify the major emission sources and work to reduce their effect early in the design process.

Objectives

The goals of this project were set as follows:

1. Create an equivalent circuit model of the intentional and parasitic current paths in the PowerFlex70 including:
 - a. the IGBT module
 - b. the motor and connecting cables
2. Demonstrate and document the processes involved in modeling, computer simulation, and laboratory measurement necessary for parasitic parameter extraction.

Overview

Geometry and layout are of paramount importance when identifying EMI sources and coupling mechanisms. The physical geometry of the system, to a large extent, determines how readily EM energy is radiated. Fig. 2 shows the EMI path of the system. The goal is to economically minimize common-mode currents on the connecting cables.

The dominant sources of EMI for the motor control module are switching currents created by the switching action of the IGBTs. The energy from these currents can be radiated from the motor connecting cables due to the presence of common-mode current paths created by parasitics. Coupling paths consist of common-mode current paths from the heat sink and enclosure to the IGBT module and the printed circuit board.

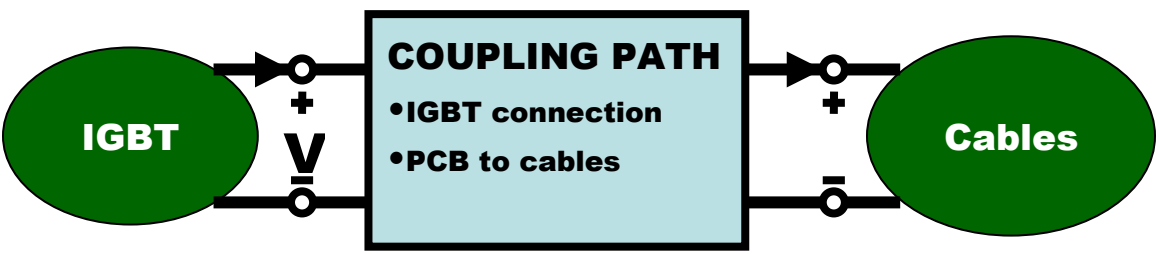


Figure 2 - EMI System

Fig. 3 shows a preliminary measurement of the emissions from the motor output cables of a PowerFlex70 (noise floor at -107dBm).

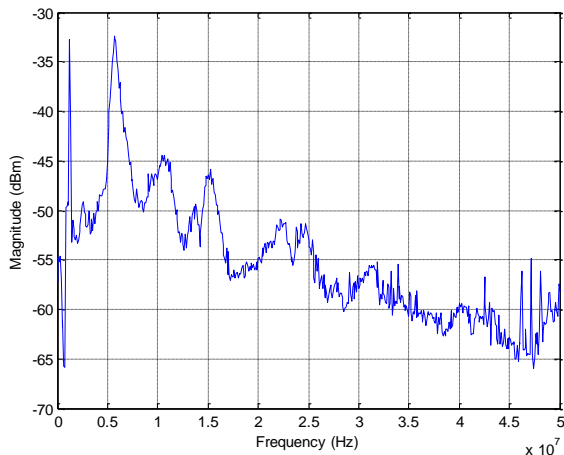


Figure 3 - Wide Band Emissions of Powerflex70 Drive Output

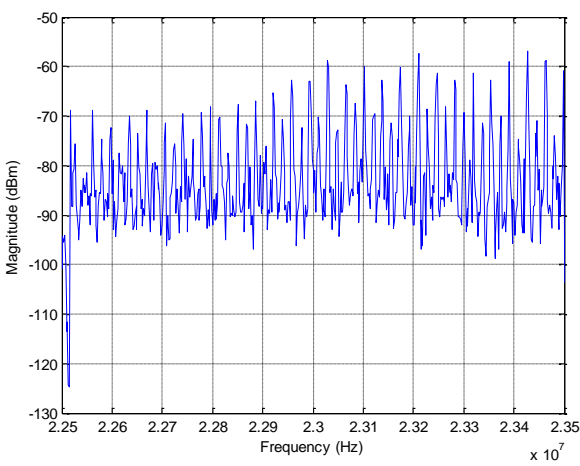


Figure 4 - Narrow Band Emissions of PowerFlex70 Drive Output

From previous experience, the IGBT will be the presumed source of EMI energy due to the large, fast-switching currents and proximity to a large metallic heat sink. One focus will be on modeling the IGBT; another will be on the motor and connecting cables.

Although Rockwell Automation recommends that shielded cable be utilized to ensure compliance, customers may use existing unshielded cable. Therefore, both types of cable will be investigated. Mitigation techniques related to the effectiveness of suppression ferrites and shielding will be explored.

Model development will follow the paradigm illustrated in Fig. 5. The coupling path, cable, and motor will be modeled with geometry in mind. A one-to-one correspondence between the equivalent circuit and the geometry will be maintained. Complete circuit models will be developed including parasitic devices present due to system layout and topology. These models will then be validated via a combination of numerical simulation (CST EM Studio, CST Microwave Studio, and Ansoft Q3D) and laboratory measurements with using vector network analyzers, impedance analyzers, time domain reflectometers, and spectrum analyzers.

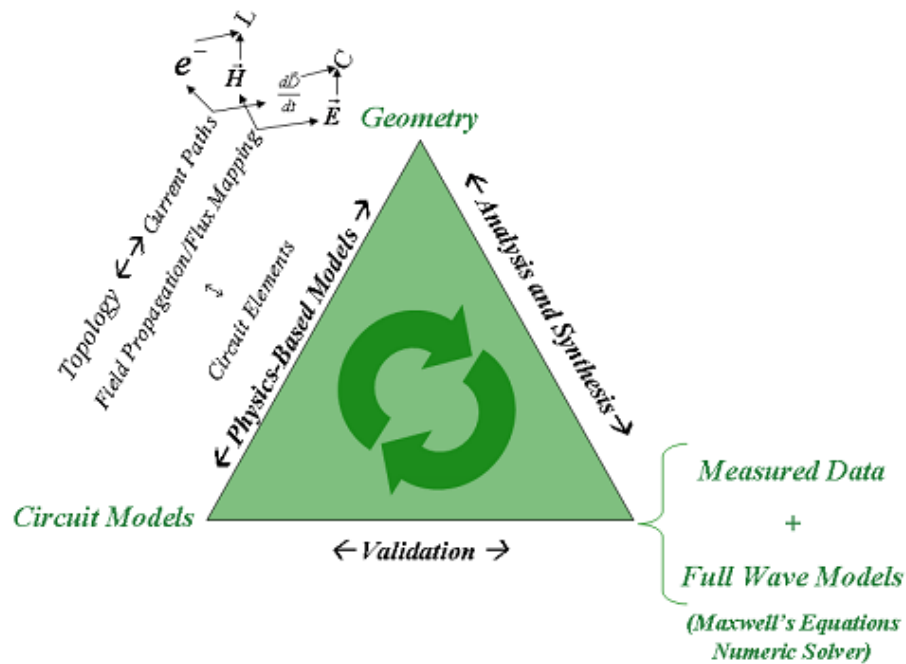


Figure 5 - Equivalent Circuit Modeling Paradigm

Once completed, the equivalent circuit model will allow the rapid identification of critical common-mode current paths, and will allow EMC problems to be identified early in the design phase. It will also allow meaningful assessment and selection of mitigation measures such as geometry modification, ferrites and shielding.

Summary of Achievements

The teams at Rose-Hulman Institute of Technology and Missouri University of Science and Technology split into two sub-teams in order to accomplish the assigned tasks. One team focused on modeling the IGBT while the other worked on the motor and cables modeling.

IGBT Module Modeling

In modeling the IGBT package (Fig. 6), the goal was to determine the parasitic capacitances and inductances of the IGBT module and append these parasitic elements to the circuit schematic.

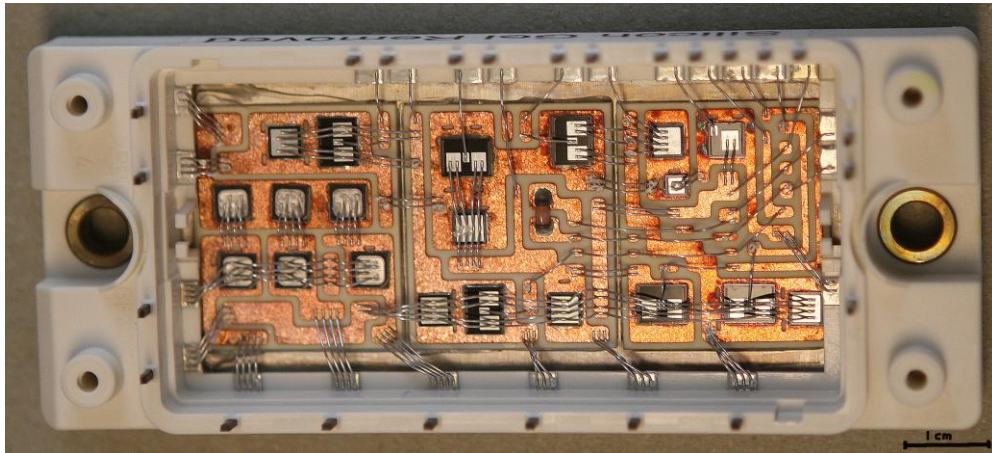


Figure 6 - IGBT Package

The geometry of the package presents two dominant parasitic capacitances: copper area fills to area fills and area fills to heat sink. The major copper area fills are shown in Fig. 7.

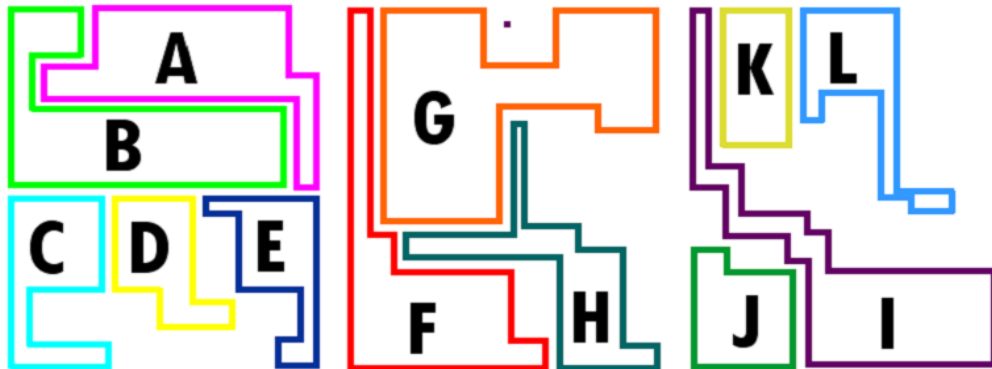


Figure 7 - Labeled Area Fills

First, we modeled these capacitances using CST Microwave Studio, a numerical electromagnetic field solver package. The dielectric constant of the alumina substrate was measured by sputtering a sample of the material with copper and measuring the capacitance, plate area, and thickness of the sample. The dielectric constant and measured substrate thickness were used in the simulations.

Models of each area fill were then constructed in CST Microwave Studio and their capacitances were obtained from the -20 dB/decade impedance curve. The largest area fill to area fill capacitance was determined to be less than 10% of the smallest area fill to heat sink capacitance. Therefore, it was concluded that the area fill to heat sink capacitances would dominate the capacitive coupling paths. This was confirmed in later simulations using Ansoft Q3D Extractor, as the mutual capacitances were on the order of a few femtofarads. The area fill to heat sink capacitance values were superimposed on the original circuit schematic as shown in Fig. 8. The simulated values for these capacitances are shown in Table 1.

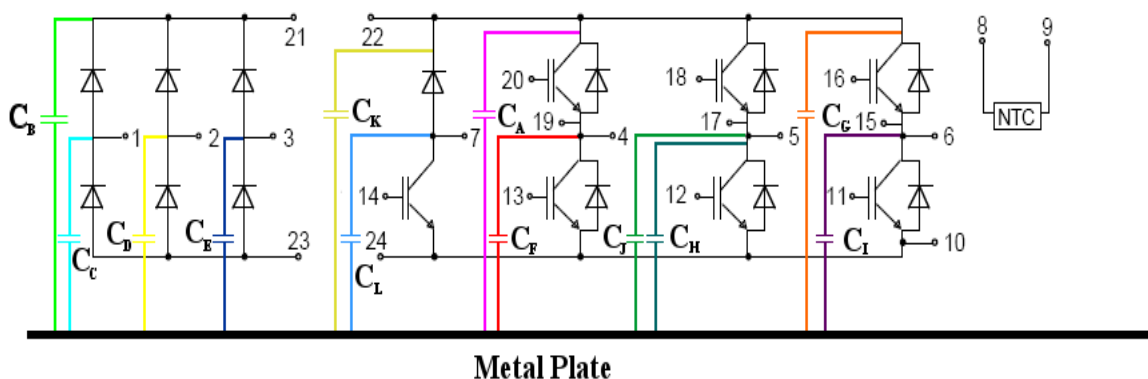


Figure 8 - Updated IGBT Package Schematic

Table 2 – Area Fill to Heat Sink Simulated Capacitances

Region	Capacitance (pF)	Region	Capacitance (pF)
A	34.5	G	57.3
B	38.8	H	25.6
C	19.1	I	45.1
D	15.4	J	17.3
E	16.0	K	15.1
F	35.9	L	19.3

To validate these simulations, we took laboratory measurements of the three largest area fill to heat sink capacitances (B, G, and I) using an impedance analyzer. Images of this setup can be found in Figs. 9 and 10. At Missouri S&T a HP4921A impedance analyzer was used with a low-impedance test head. RHIT used a HP4294A impedance analyzer with an auto-balancing test fixture. Fixture compensation was used in both setups (open

and short for Missouri S&T; open, short, and load for RHIT). The results are shown in Table 2 below.

Table 3 – Area Fill to Heat Sink Capacitances

Region	Measured (pF)	Simulated (pF)	% Difference
B	37.7	38.8	2.9
G	53.3	57.3	7.2
I	39.4	45.1	13.7

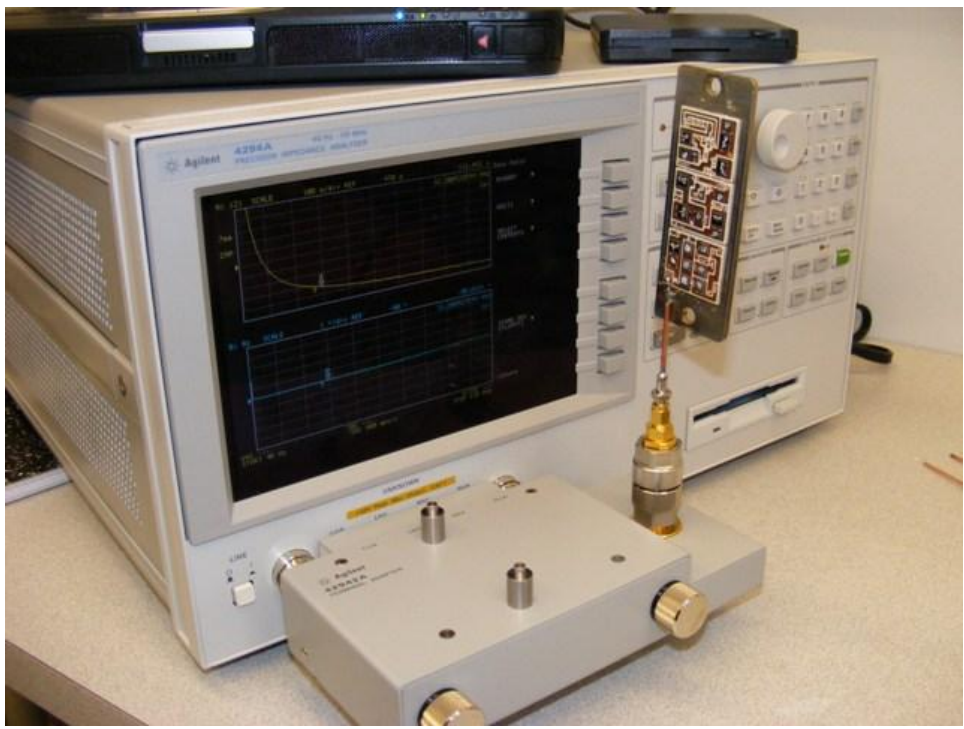


Figure 9 - IGBT Capacitance Measurement Setup

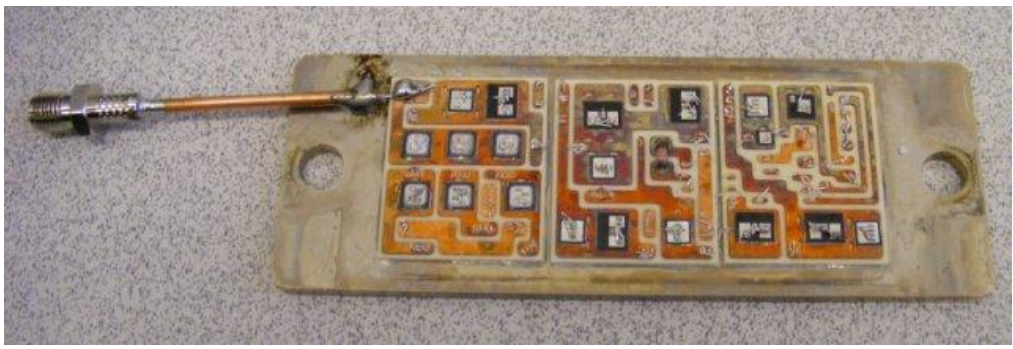


Figure 10 - IGBT Area Fill B Capacitance Measurement

Two of these capacitances agreed to within 8%. The largest region – I – was within 14%. Region I has a long, narrow appendage which allows outside fields to interact with it, so the margin of error is larger. However, we were still satisfied with the agreement of our measurements and simulations, as it is within an acceptable margin of error. Knowing that the simulations matched the measurements gave confidence in their accuracy.

The next step in modeling the IGBT package was to determine the existing common-mode parasitic inductances. To find these scattered, more complicated parasitics, it was needed to first determine the self-inductances of each of the three phase legs (Phase Leg 1 is shown as an example in Figures 11 and 12). Each phase leg corresponds to one of the three phases from the positive DC rail to the output to the motor. The outputs are pins 4, 5, and 6 corresponding to phases 3, 2, and 1, respectively.

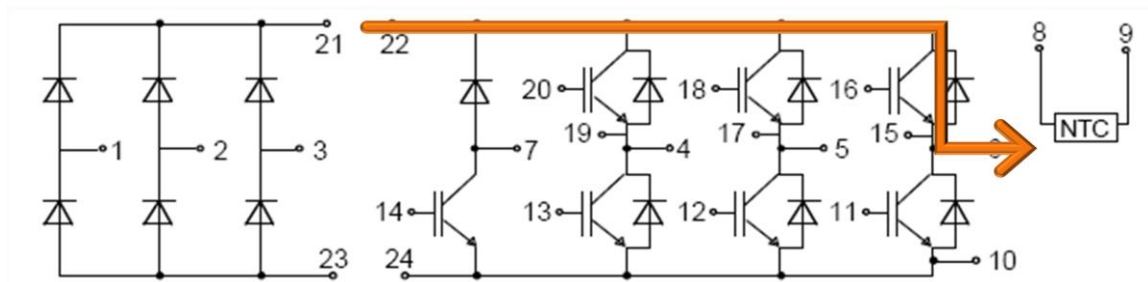


Figure 11 - Schematic of Phase Leg 1

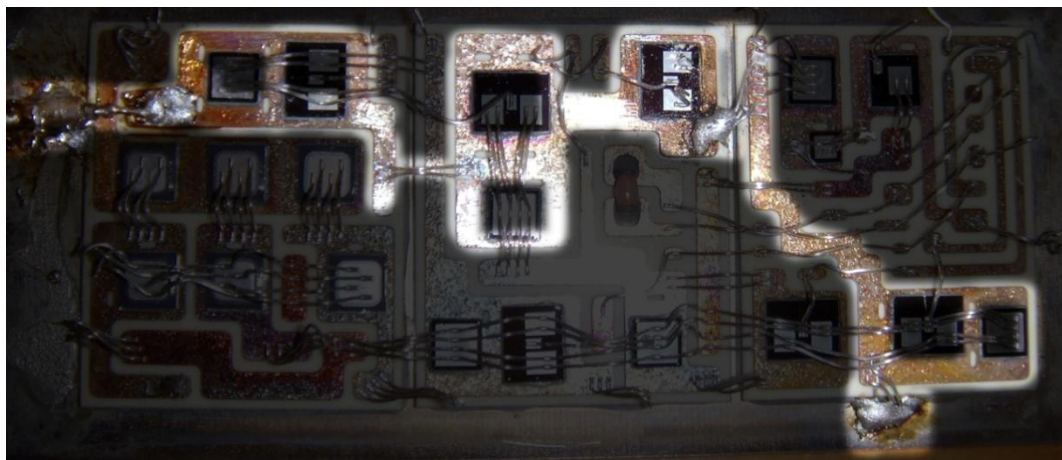


Figure 12 - Image of Phase Leg 1: RHIT Setup



Figure 13 - Image of Phase Leg 2: Missouri S&T Setup

Before the partial inductances could be extracted, it was necessary to measure the entire phase leg. First, the entire phase leg impedance was obtained in order to know the total inductance and its corresponding impedance curve. A probe was placed on the positive DC rail input and the output (at the location of the bond wires leading to the corresponding output pin) was shorted to the heat sink. Three-dimensional models of each phase leg, consisting of area fills and the bond wires connecting them, were constructed in CST Microwave Studio. In a similar manner to the capacitance simulations, each inductance value was extracted from the +20 dB/decade impedance curve (see Table 3).

Once again, the simulations were validated against measurements, taken with the same impedance analyzers as before. Two distinct methods were used to measure the total impedance of the phase leg. The RHIT team used the original bond wires of the IGBT module, while removing all connected bond wires not associated with the phase being measured. They bypassed the transistor by soldering its bond wires to the area fill (See Figure 12). The Missouri S&T team removed all bond wires and reattached copper bond wires in the place of the originals. Then, the transistor in the phase leg was removed and shorted (see Figure 13). The RHIT approach had the advantage of using the original setup with accurate bond wire dimensions. The Missouri S&T approach had the advantage of having cleaner solder joints, accurate location of bond wires, and the certainty that any unexpected current paths (from additional bond wires) were removed. However, the

Missouri S&T team had difficulty reproducing the geometry of phase 2 due to the jumping pairs of bond wires from transistor to diode found on area fill G. It was observed that the results were greatly dependent on the bond wire geometry. It was also observed that variations in the solder connection from the probe produced a non-negligible effect on the results. Both methods produced the same total inductance, and all three phase legs agreed to within 6% of the simulated value (see Table 3). These results were sufficient to give confidence that the simulated inductances accurately reflect the actual inductances.

Table 4 – Phase Leg Inductances

Phase Leg	Measured (nH)	Simulated (nH)	% Difference
1	13.3	13.1	1.3
2	12.1	12.8	5.6
3	9.1	8.7	4.5

In order to develop an equivalent circuit model, it was necessary to find the contribution of each area fill and bond wire to the total common-mode inductance. Each area fill and bond wire was modeled as its own small loop, and shorted to the heat sink. The sum of the partial inductances in each phase leg should be equal to the total self-inductance of that phase leg. After working with several circuit topologies for our measurement of Phase 1 and using several different methods of simulation (CST 2006b with discrete ports, CST 2008 with discrete face ports, and Ansoft Q3D), the most accurate model was developed (See Figure 14). Ansoft Q3D Extractor was used to extract partial inductance values and simulated the topology shown in Figure 14 using Agilent Advanced Design System (ADS) software. It was found that the result matched well with the measured impedance curve, as shown in Figure 15. The extracted data is included in Table 4.

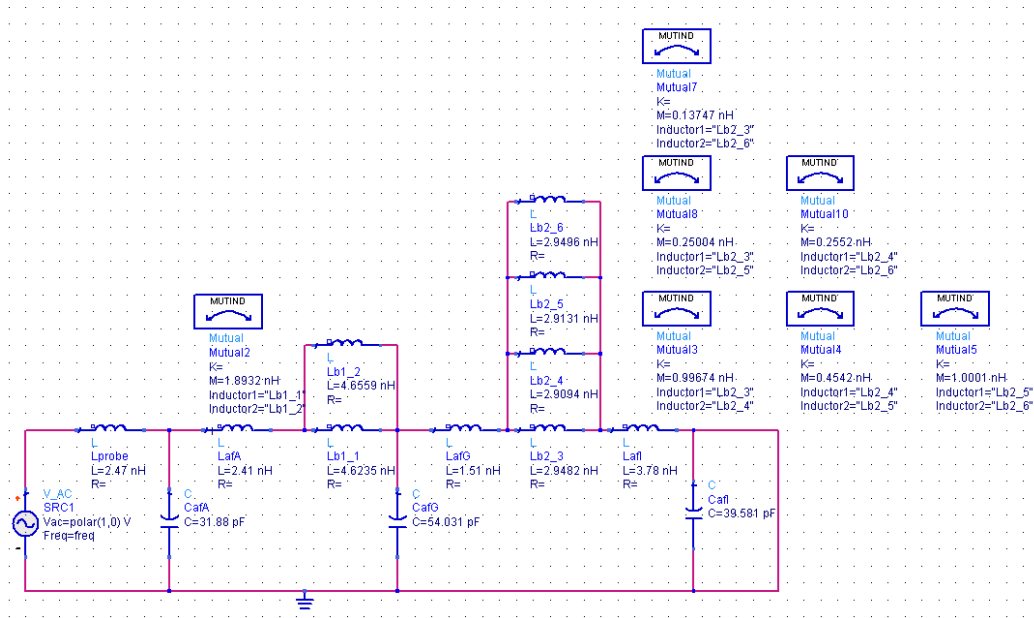


Figure 14 - Phase Leg 1 Schematic

Table 5 - Phase Leg 1 Parasitic Values

Phase Leg 1			
Probe	Inductance	2.47	nH
Area Fill A	Capacitance	31.88	pF
	Inductance	2.41	nH
Bond Wires	Wire 1 ind.	4.62	nH
	Wire 2 ind.	4.66	nH
	Mutual ind.	1.89	nH
Area Fill G	Inductance	1.51	nH
	Capacitance	54.03	pF
Bond Wires	Wire 1 ind.	2.95	nH
	Wire 2 ind.	2.91	nH
	Wire 3 ind.	2.91	nH
	Wire 4 ind.	2.95	nH
	Mutual ind. (1-2)	1.00	nH
	Mutual ind. (2-3)	0.45	nH
	Mutual ind. (3-4)	1.00	nH
	Mutual ind. (1-3)	0.25	nH
	Mutual ind. (2-4)	0.26	nH
Area Fill I	Mutual ind. (1-4)	0.14	nH
	Inductance	3.78	nH
	Capacitance	39.58	pF

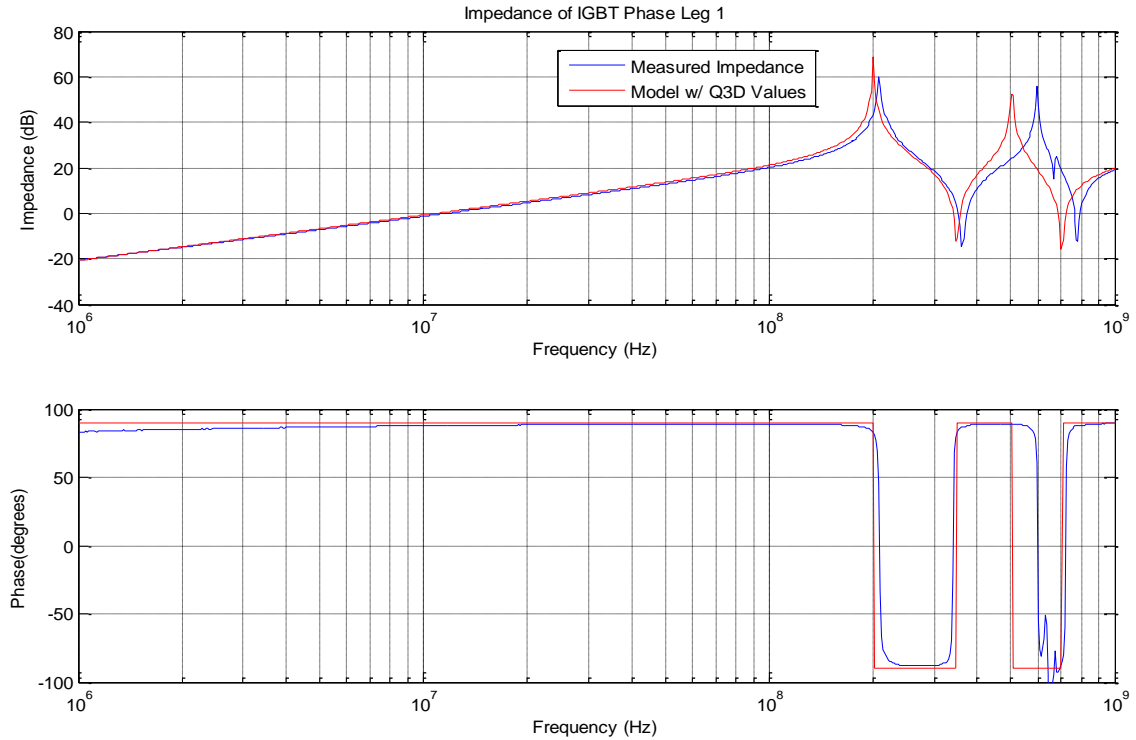


Figure 15 - Phase 1 Impedance: Modeled vs. Measured Impedance

After Phase 1 was successfully modeled, Phases 2 and 3 were modeled using the same method. In order to reduce the complexity of the final model, the individual bond wires and their corresponding mutual inductances were modeled as a single inductor. The models and results are shown in Figures 16-19. The data is included in Tables 5 and 6.

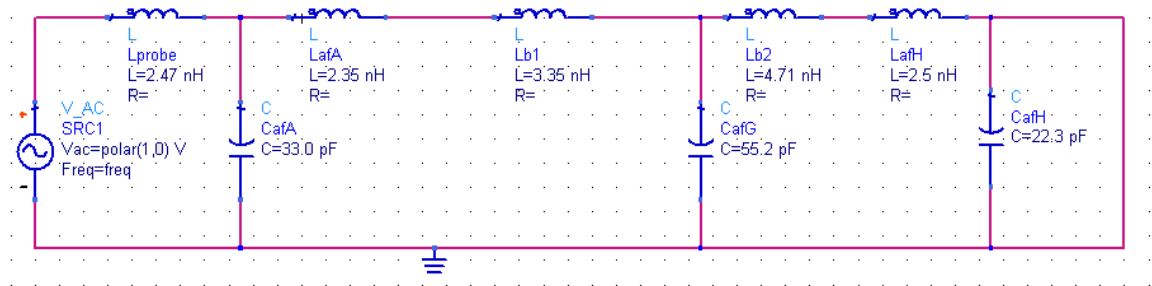


Figure 16 - Phase 2 Model

Table 6 - Phase Leg 2 Parasitic Values

Phase Leg 2			
Probe	Inductance	2.47	nH
Area Fill A	Capacitance	33.00	pF
	Inductance	2.35	nH
Bond Wires	Inductance	3.35	nH
Area Fill G	Inductance	4.71	nH
	Capacitance	55.20	pF
Bond Wires	Inductance	4.71	nH
Area Fill H	Inductance	2.50	nH
	Capacitance	22.30	pF

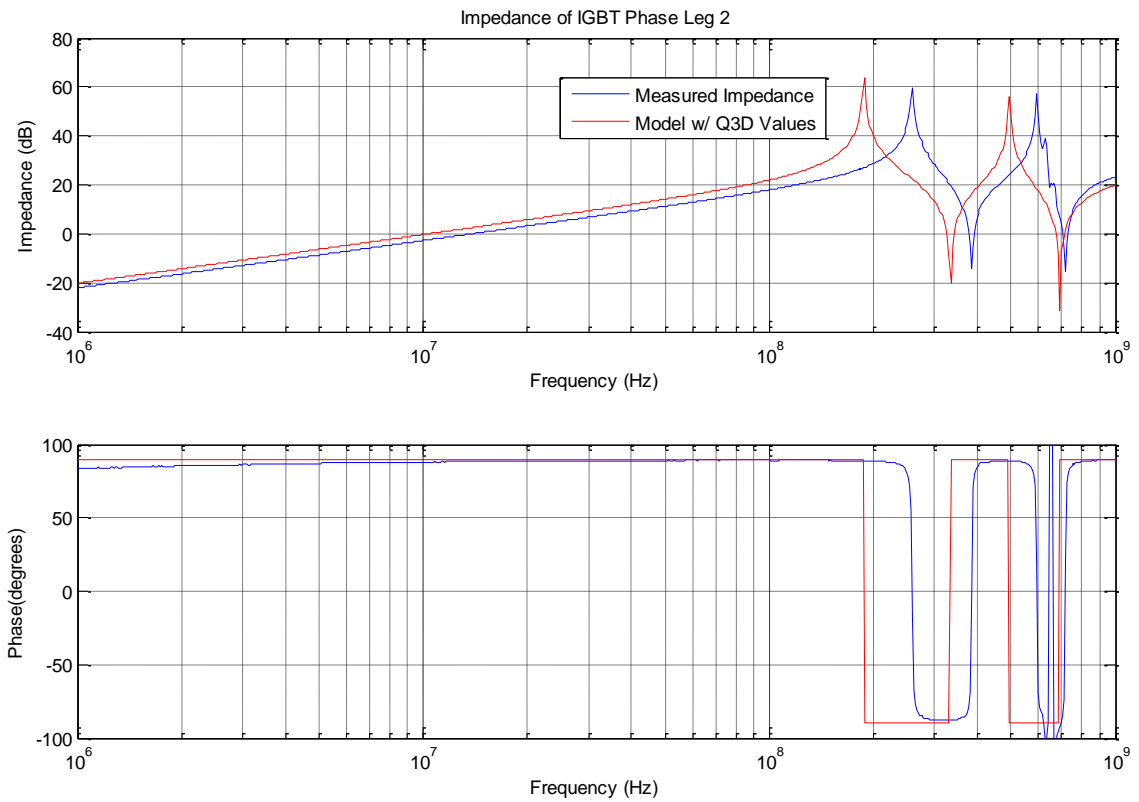


Figure 17 - Phase 2 Modeled vs. Measured Impedance

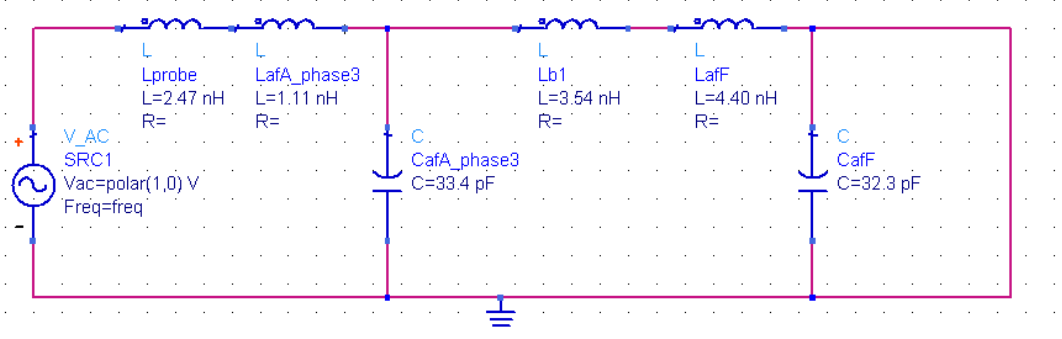


Figure 18 - Phase 3 Model

Table 7 - Phase Leg 3 Parasitic Values

Phase Leg 3			
Probe	Inductance	2.47	nH
Area Fill A	Capacitance	33.40	pF
	Inductance	1.11	nH
Bond Wires	Inductance	3.54	nH
Area Fill F	Inductance	4.40	nH
	Capacitance	32.30	pF

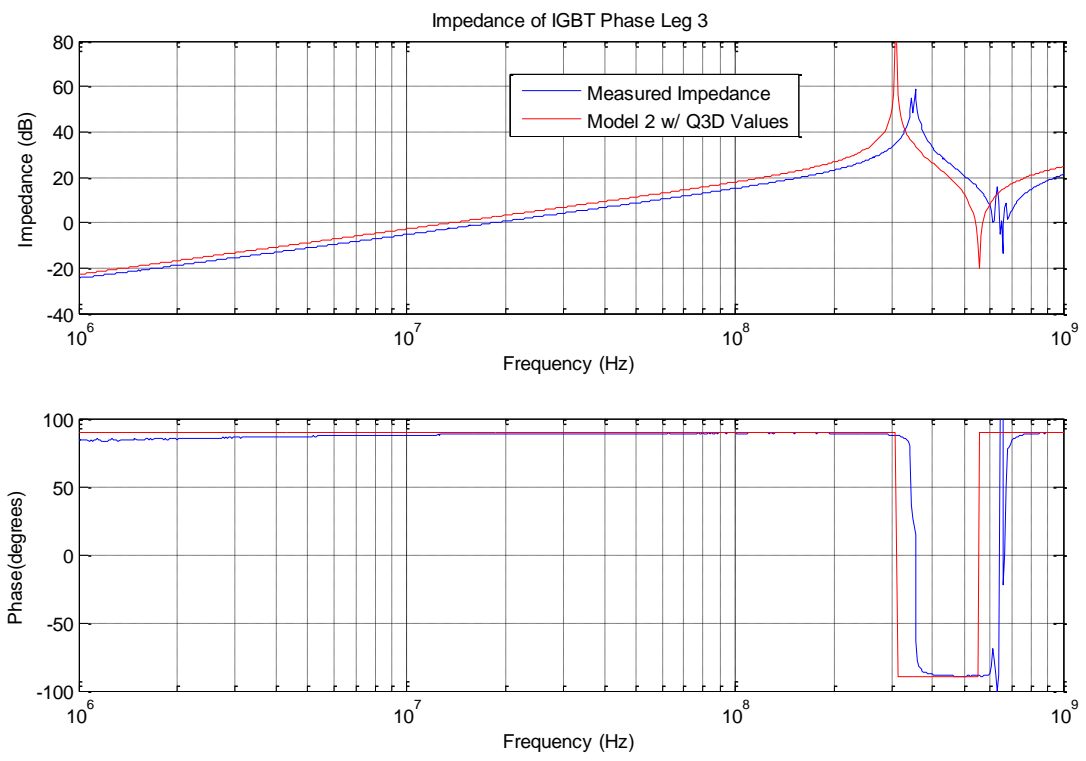


Figure 19 - Phase 3 Modeled vs. Measured Impedance

With the rush to obtain a final equivalent circuit model for initial testing, the simulations and models were not refined to obtain a closer match because efforts were diverted to extracting the parasitic values for the intentional current paths. Part of the mismatch in Phase 2 may be because the jumping bond wires across the transistor and diode on area fill G were extremely hard to reproduce in the Missouri S&T measurement setup (compare Figures 12 and 13)

The intentional current paths included at least 8 different loops for each phase leg. Four (two complete loops per schematic, shown in red) of these loops are shown in Figure 20.

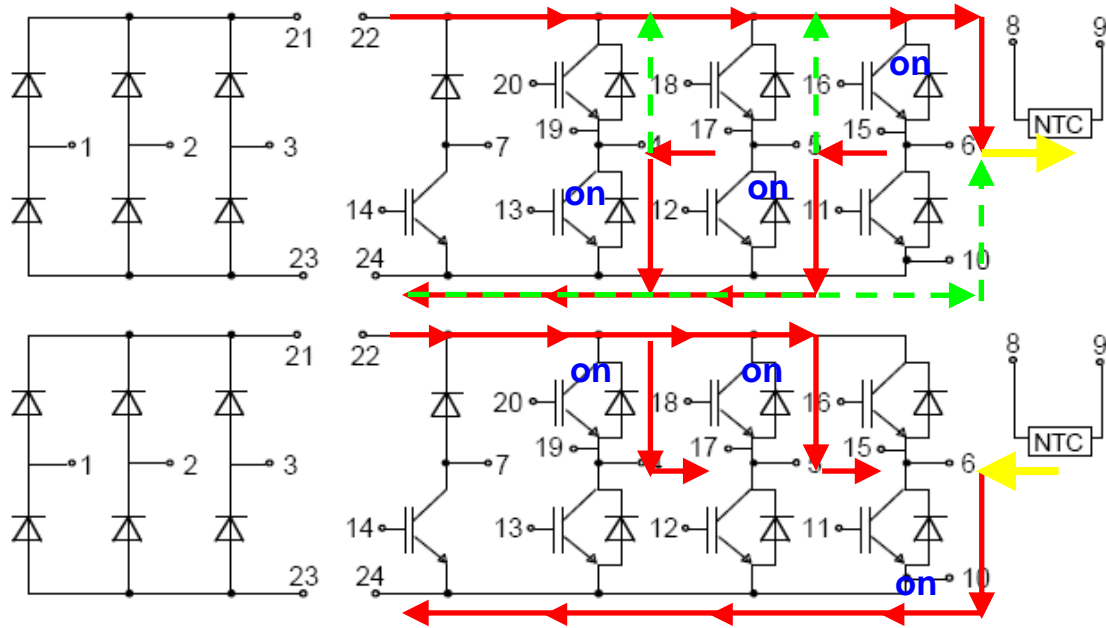


Figure 20 - Several Phase 1 Intentional Current Paths

The third set of current paths (shown in green in Figure 20) includes the current path through the flyback diodes. The last two current paths are not shown but represent the case when all the upper transistors are on or when all the lower transistors are on.

A model of the entire IGBT was put together. First, Solidworks was used to model the area fill geometry. An image of the IGBT was overlaid on the model and the area fill geometry was traced and extruded. This file was imported into CST, the bond wires were created, and the final model (see Figure 21) was imported into Q3D for simulation. As Q3D allows the user to exclude objects from the simulation, the entire model will be the base for future simulations.

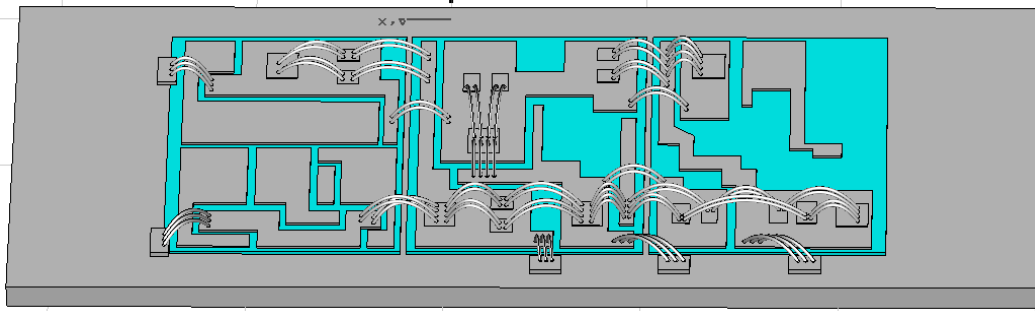


Figure 21 - Entire IGBT Model

As this modeling is beyond the scope of our work, the results are not currently included. When the simulations are completed for both the negative DC rail common-mode partial inductances and the intentional current path partial inductances, these will be placed in the final PSpice model for testing.

Motor and Cables

The main goal of the motor and cables team was to formulate and test methods for suppressing electromagnetic interference that emerges from an AC motor drive at the motor and cables. To achieve this goal, we began constructing various test setups as a means to develop a model for the motor and cables. From this model, we can simulate suppression methods, and verify their effectiveness.

One of the first important parameters to characterize the motor and cables was to find the input impedance. A drawing of the test setup that was used to find this for the unshielded cables is shown in Fig. 22, where pictures of the actual test setup are included in Figures

23 - 25. The test setup had an aluminum plane that formed the base of the setup and also served as a return plane for the common mode current. In addition to the aluminum return plane, there was an aluminum block beneath the motor to keep the motor securely mounted. The motor was wired for high voltage and the wires rested on insulation foam to separate them from the grounding plane by 10cm as specified by the CISPR standards. In addition, the insulation foam was used to keep the return plane level. At the opposite end of the return plane, approximately 8.5 feet away from the motor, was an 'L' shaped aluminum plate fastened to the return plane with copper tape. An N-type bulkhead connector was mounted to the plate, and all three phase wires were soldered to the inner conductor of the connector; copper tape was used to reinforce and ensure a good connection to the return plane. The opposite end of the N-type bulkhead connector allowed a connection for one port measurements.

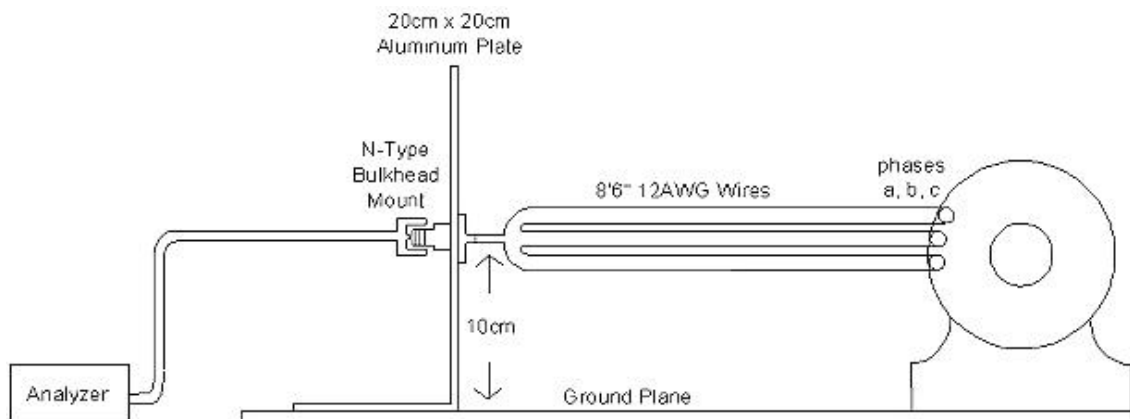


Figure 22 - Motor and Cable Test Setup



Figure 23 - Motor and Cable Test Setup: Full View

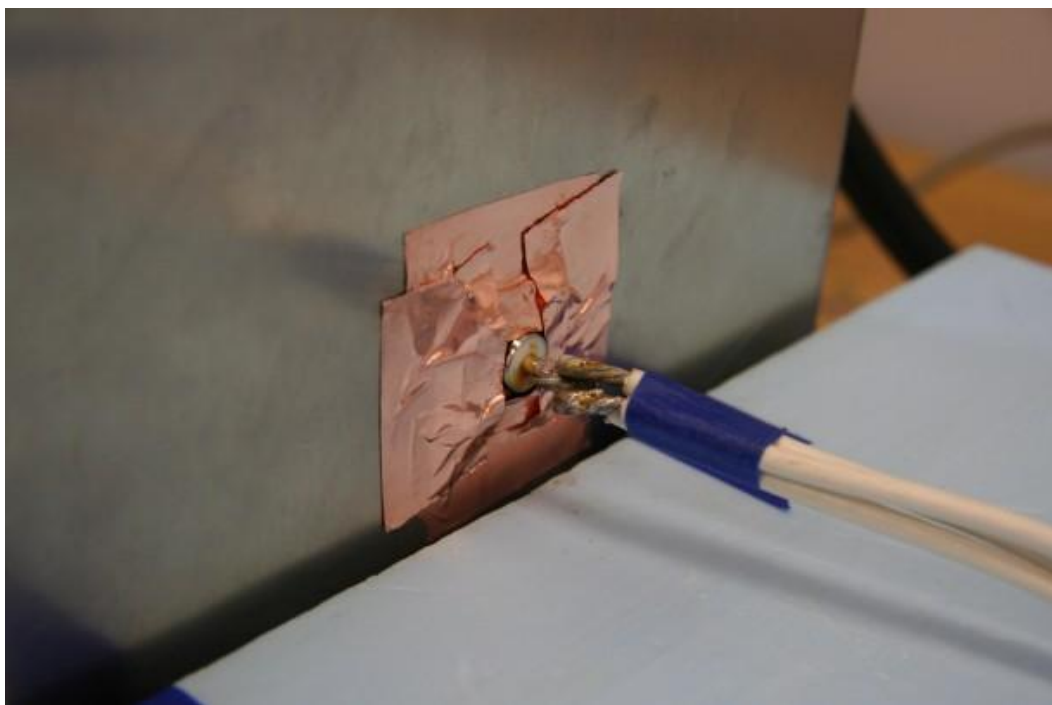


Figure 24 - Motor and Cable Setup: N-Type Bulkhead Connector

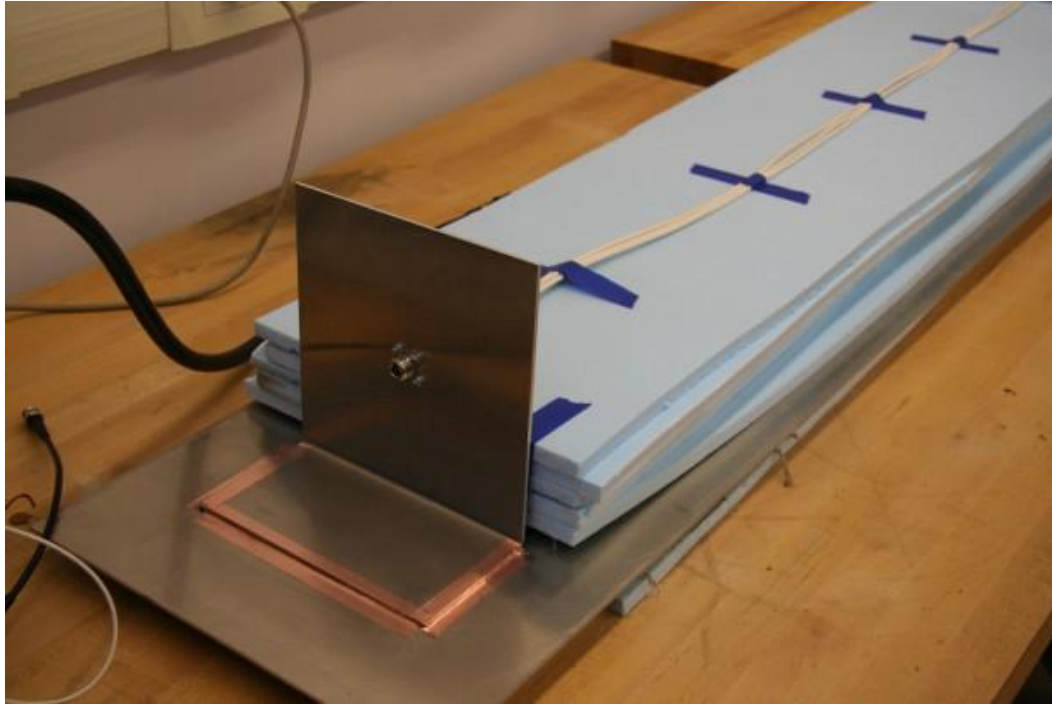


Figure 25 - Motor and Cable Test Setup: Port Interface

A similar setup was also developed for a shielded cable. To ensure a good shielded connection, 360 degree connectors were used for all shielded cable measurements. The test setup consisted of a miniature version of the 'L' shaped metal plate resting on the heat sink of the motor drive. The front metal face of the motor drive provided a secure place to connect the shield. Some pictures of this test configuration are shown in Figures 26-28.



Figure 26 - Shielded Motor and Cable Test Setup: Full View

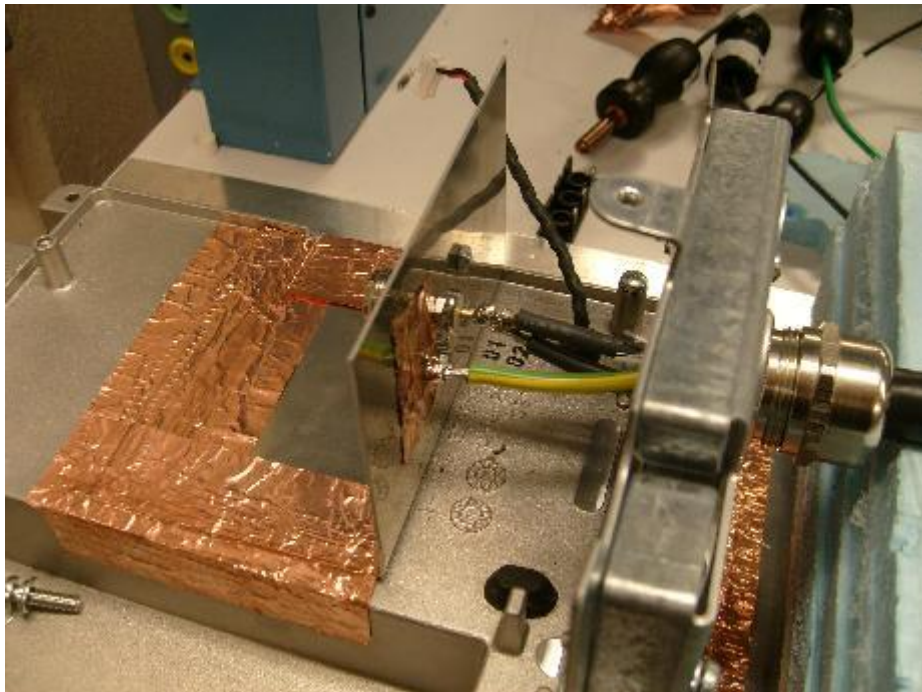


Figure 27 - Shielded Motor and Cable Test Setup: One Port Interface



Figure 28 - Shielded Motor and Cable Test Setup: Motor Wiring

The input impedance of the motor and cables was found with an Agilent 8753ES network analyzer at Missouri S&T and an HP4294A impedance analyzer at RHIT. Figure 29 shows the shielded and unshielded input impedance as a function of frequency. As can be seen by the data, at low frequencies the motor and cables are capacitive, whereas in the higher frequencies the motor and cables switch between being inductive and capacitive. It is in the higher frequencies that the characteristics of the cables dominate. One observation from the input impedance data in Figure 29 is that the capacitance of the shielded cable is much higher than the unshielded cable. At 300 kHz, the capacitance of the shielded cable is 10.61nF compared to .71nF for the unshielded cable. The increased capacitance in the shielded motor and cable setup makes sense since a possible return path (the shield) is much closer to the three phase wires than the single return plane in the unshielded setup.

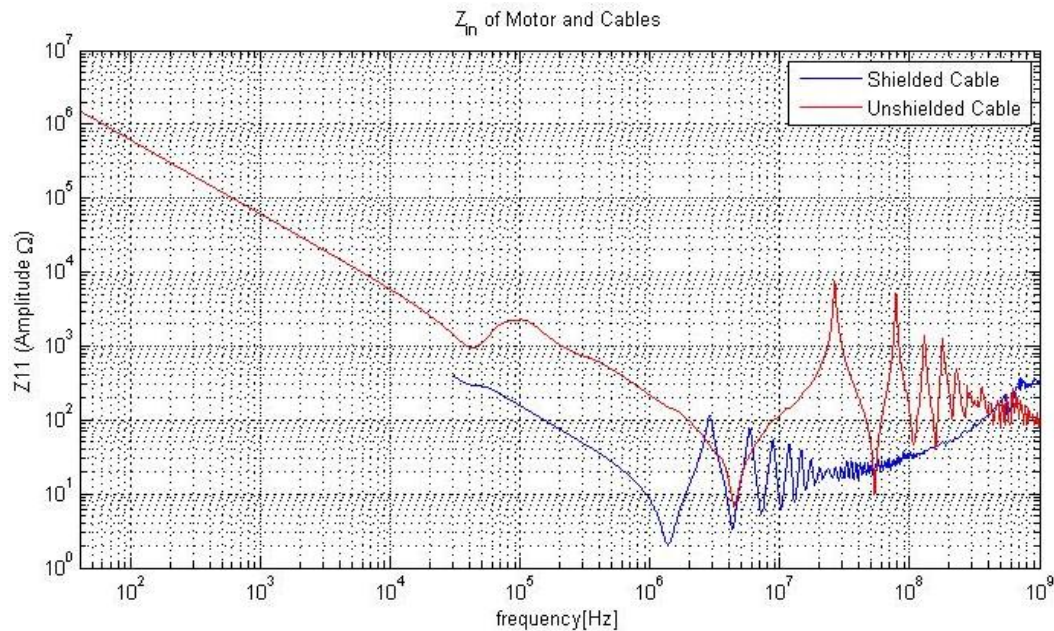


Figure 29 - Motor and Cables Input Impedance

Another parameter that was studied to see its impact on various measurement results was the addition of a ground wire in the unshielded cable measurements. To be consistent with measurements, the impact of the ground wire was studied with the same setup as the shielded cable. Pictures of this setup can be seen in Figures 30-31.



Figure 30 - Unshielded Motor and Cables Ground Wire Study Setup: Full View

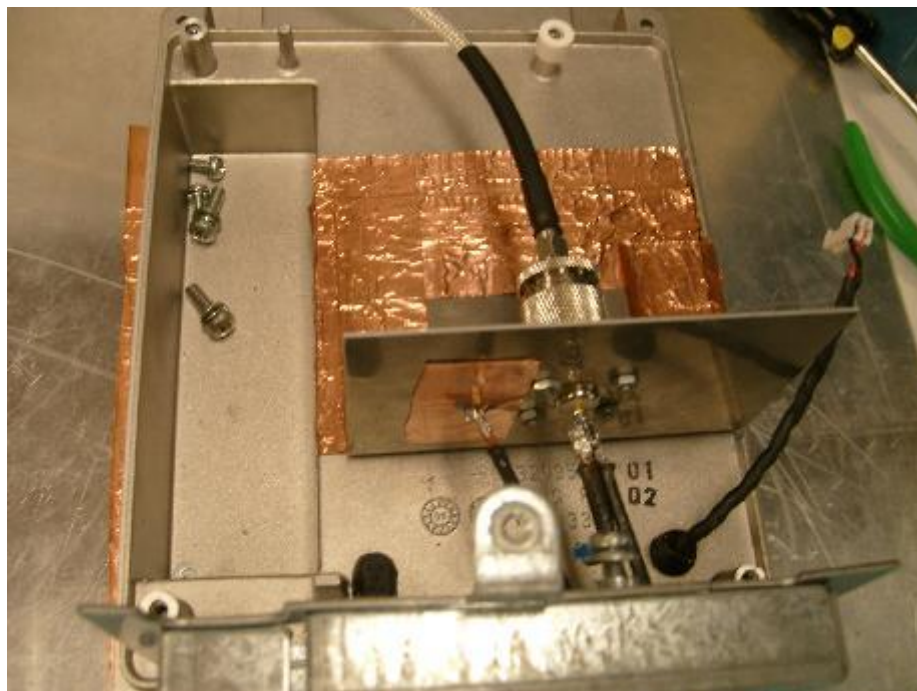


Figure 31 - Unshielded Motor and Cables Ground Wire Study Setup: One Port Interface

To see the effect of changing setups for the unshielded cable measurements, a comparison of the results without the ground wire can be seen in Figure 32. It was found that changing setups had a negligible impact on the results.

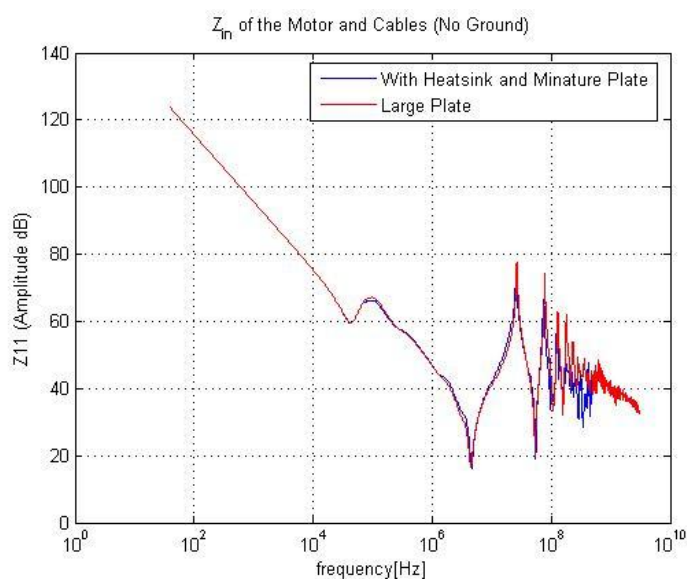


Figure 32 - Unshielded Motor and Cables Laboratory Setup Change Study

The results of the ground wire input impedance study can also be found in Figure 33. The most noticeable impacts that adding a ground wire appeared to have is moving the first resonant frequency higher by a few megahertz and creating more resonance above 40 MHz.

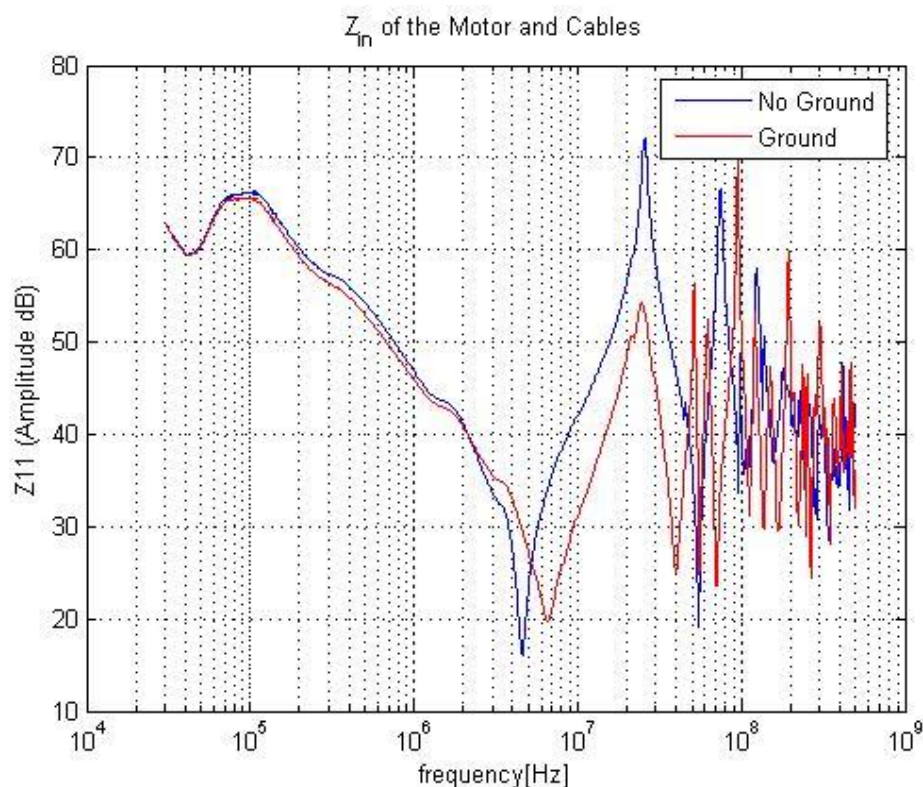


Figure 33 - Unshielded Motor and Cables Ground Wire Study

With the input impedance of the motor and cables identified, the emissions from the motor drive were next studied. The motor drive was connected to 480V and to the motor and cables. We used a Rohde&Schwarz 1066.3010.30 spectrum analyzer in conjunction with an F-62 current probe to capture the emissions through a common mode current measurement. Pictures of the test setup are included in Figures 34-36.

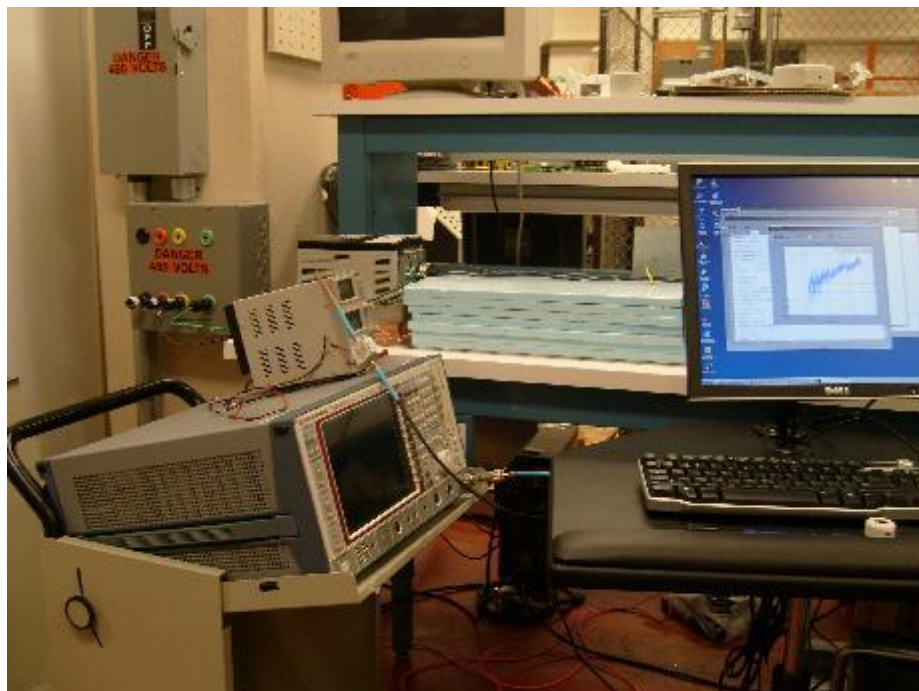


Figure 34 - Emissions Test Setup: Motor Drive, Spectrum Analyzer, Amplifier, and Current Probe

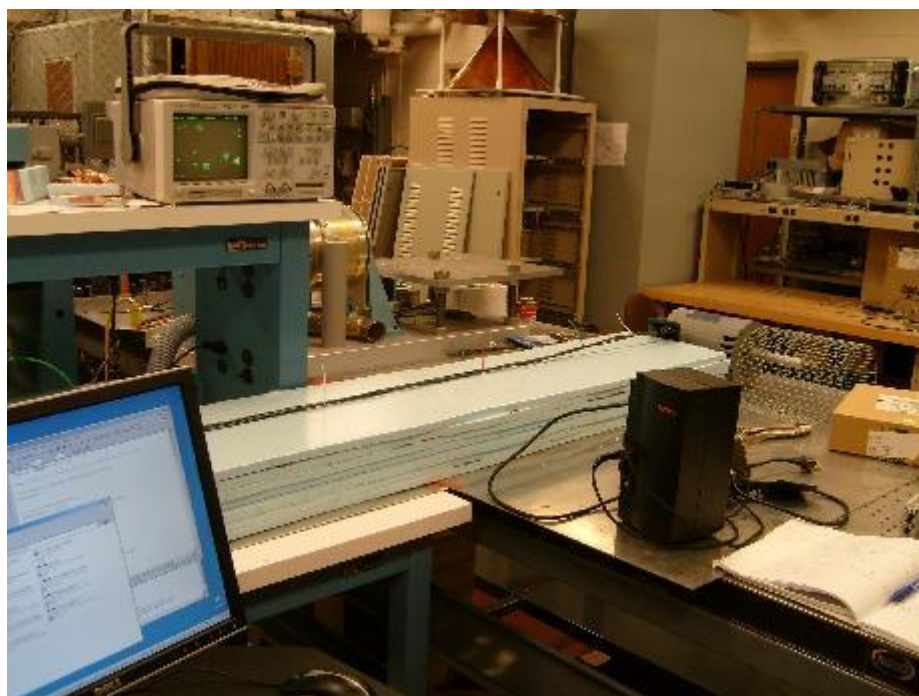


Figure 35 - Emissions Test Setup: Motor and Cables



Figure 36 - Emissions Test Setup: Close-up

Emissions measurements were taken with various ferrites attached to the cables as shown in the Fig. 37.



Figure 37 - Ferrite Placement

A critical aspect to making the common mode current measurement was placing an amplifier between the current probe and the spectrum analyzer. The role of the amplifier was to serve as a means of protection for the spectrum analyzer. In the case of an accidental short at the motor drive, the amplifier would act as a fuse, destroying the amplifier instead of the spectrum analyzer. The amplifier started to saturate around -20dBm. A plot of the amplifier gain and phase versus frequency are shown below in Figures 38-39.

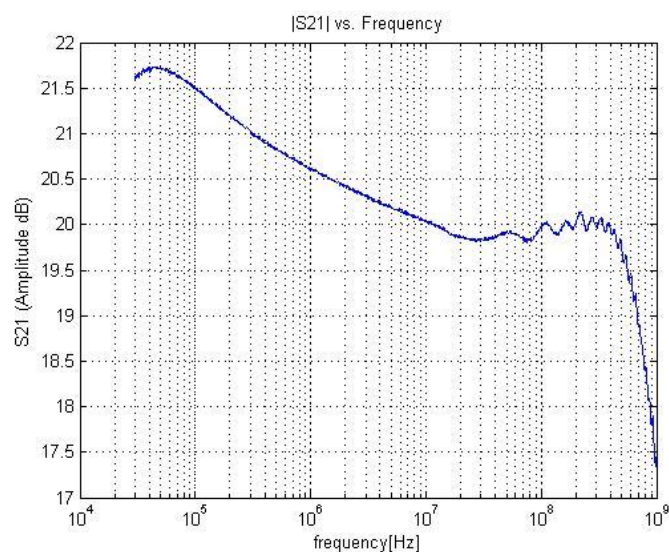


Figure 38 - Amplifier Gain vs. Frequency

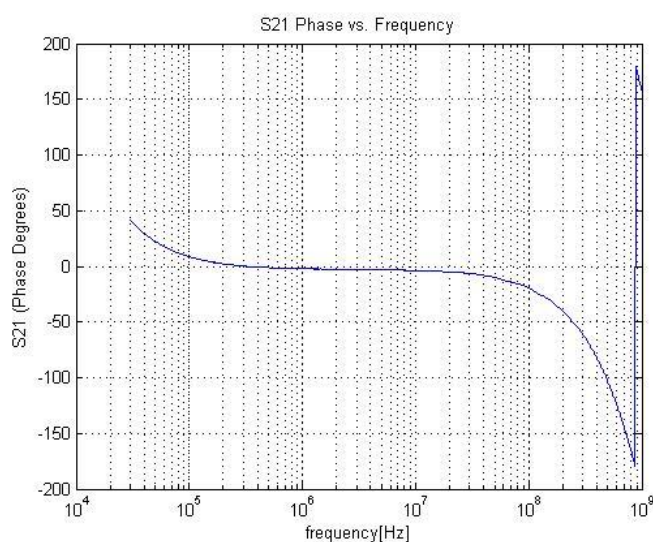


Figure 39 - Amplifier Phase vs. Frequency

We noticed that there were a significant amount of emissions when the motor was not running and power was applied to the motor drive. With this in mind the power readings from the spectrum analyzer when the motor was running are compared to the trace when power was applied to the motor drive, but with the motor not running. The common mode current measurements have the units of dBm since the current probe impedance is not factored out of the data. In addition to this, effects from the amplifier are not factored out of the data. The common mode current measurements are shown in Figures 40-45.

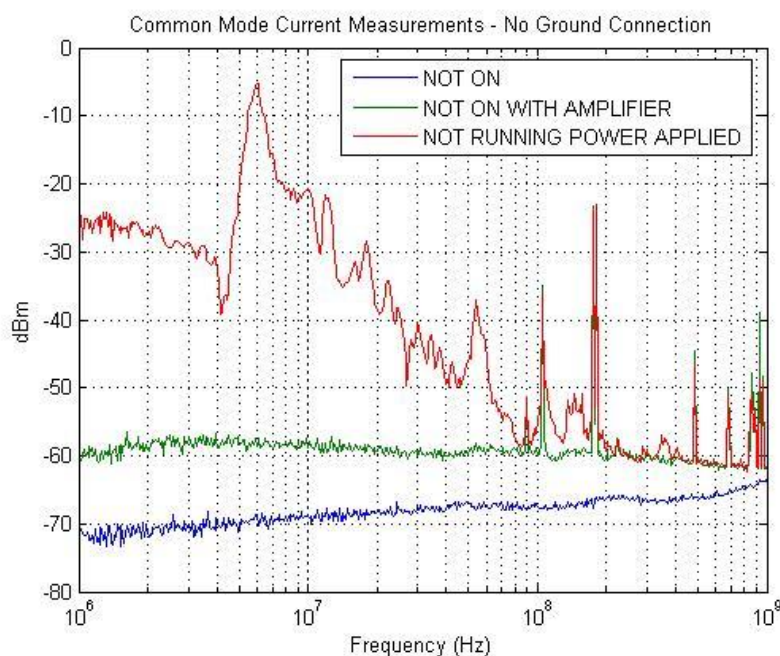


Figure 40 - Unshielded Common Mode Current Measurements: Noise Level Identification

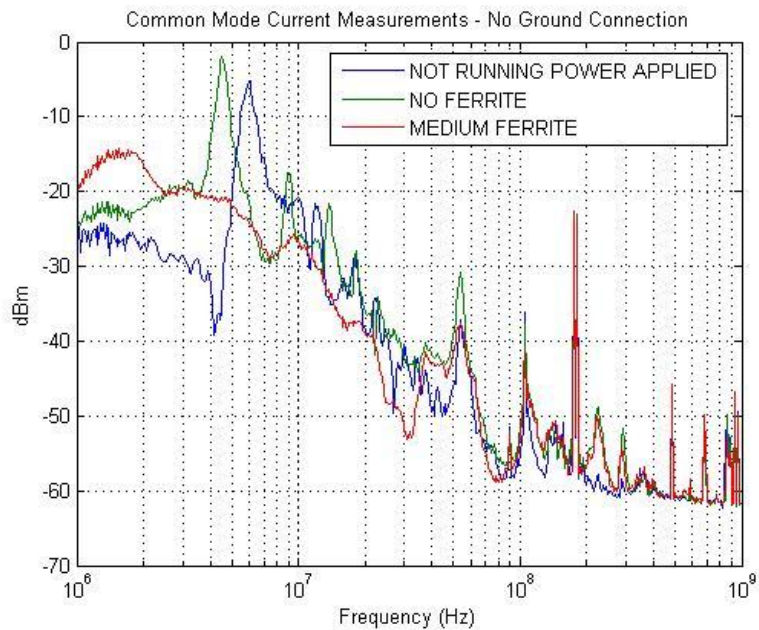


Figure 41 - Unshielded Common Mode Current Measurements (No Ground Wire)

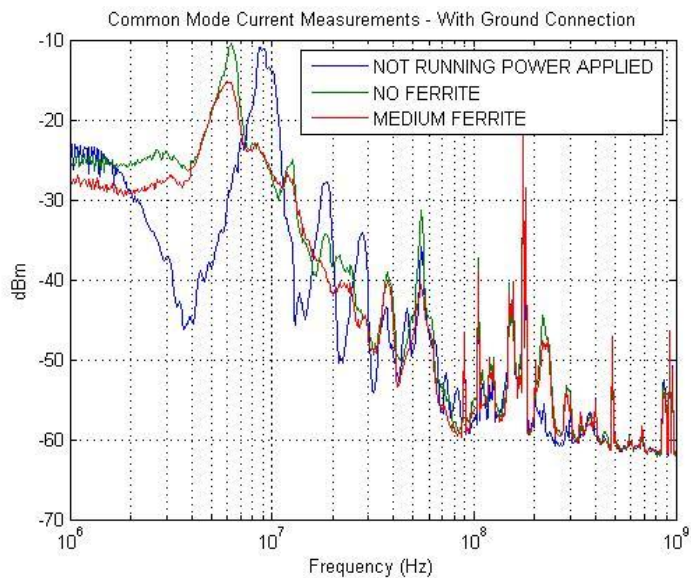


Figure 42 - Unshielded Common Mode Current Measurements (With Ground Wire)

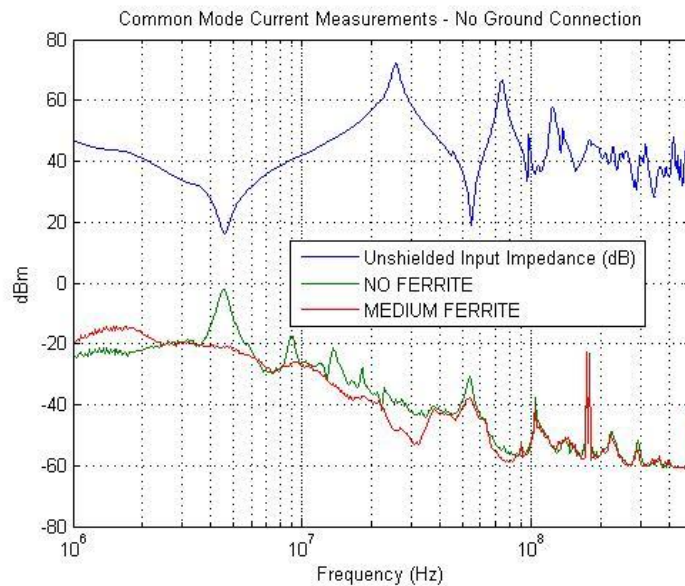


Figure 43 - Unshielded Common Mode Current Measurements (No Ground Wire): Impedance/Emissions Comparison

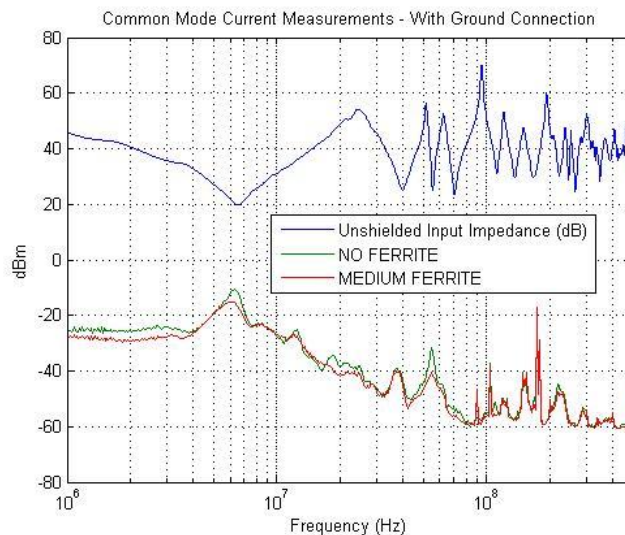


Figure 44 - Unshielded Common Mode Current Measurements (With Ground Wire): Impedance/Emissions Comparison

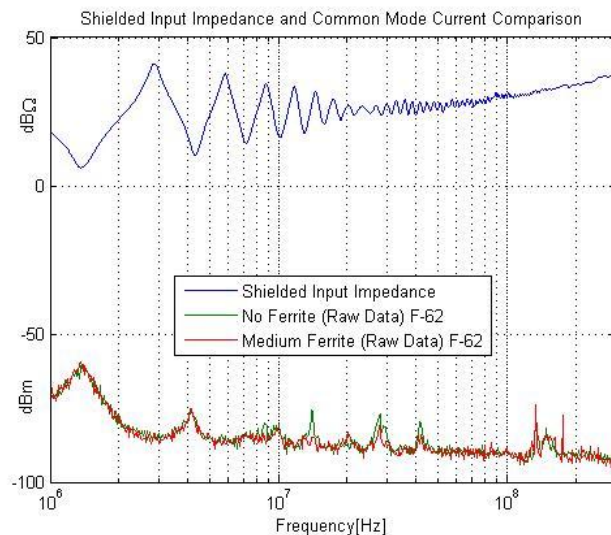


Figure 45 - Shielded Common Mode Current Measurements: Impedance/Emissions Comparison

In the common mode current measurements, the main ferrite that was tested was the Ferrishield CS33B2000. Although other ferrites were tested with the unshielded cable, the CS33B2000 was one of the few that could fit around both sets of cables. To better understand how ferrites helped reduce the common mode current, the input impedance of the motor and cables were studied with various ferrites attached. With the setup shown in Fig. 23, the input impedance was determined with the network analyzer at Missouri S&T and an impedance analyzer at RHIT. The effects of the ferrites placed at different points on the cables are shown in Figures 46-49. We mainly cared about ferrites placed in close proximity to the plate. The results obtained in Figures 48-49 were mainly done out of curiosity. The data in Figures 46-47 shows that the ferrites increased the impedance in specific frequency bands. Fig. 50 is a specification sheet from Ferrishield showing the impedance characteristics of the CS33B2000 ferrite.

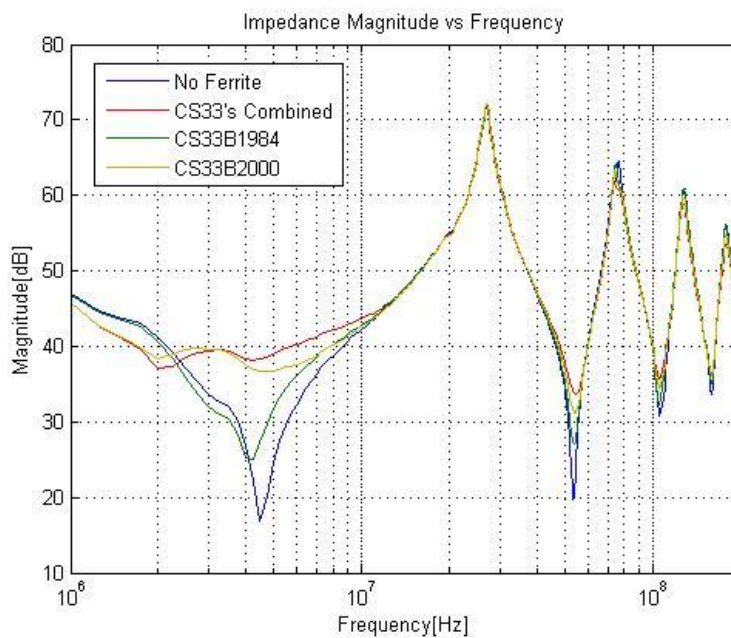


Figure 46 - Effects of Ferrites 1 inch from Plate

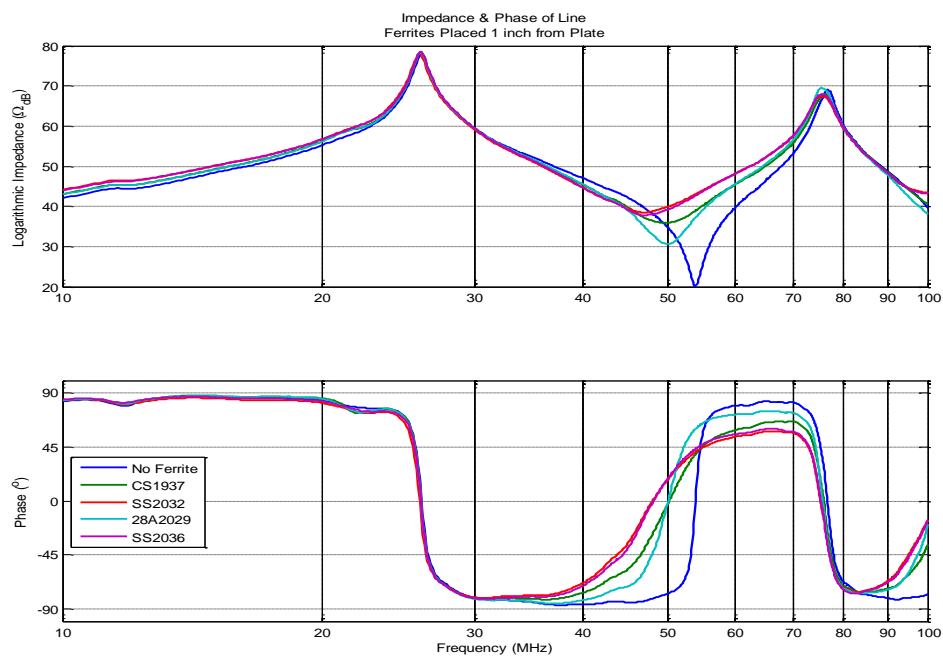


Figure 47 - Effects of Ferrites 1 inch from Plate

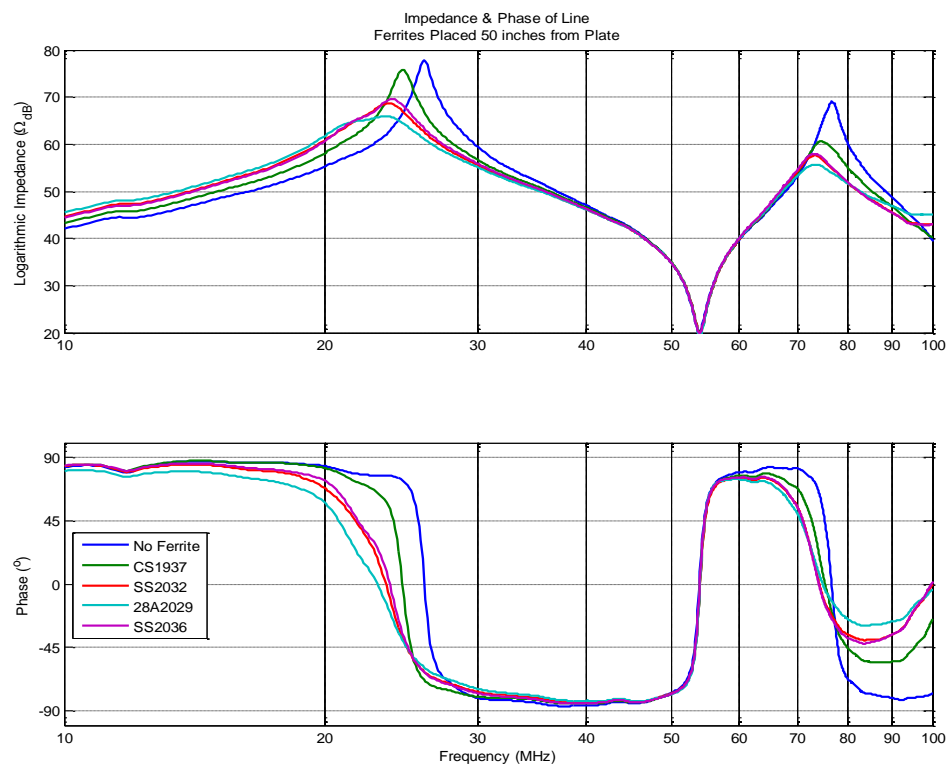


Figure 48 - Effects of Ferrites 50 inches from Plate

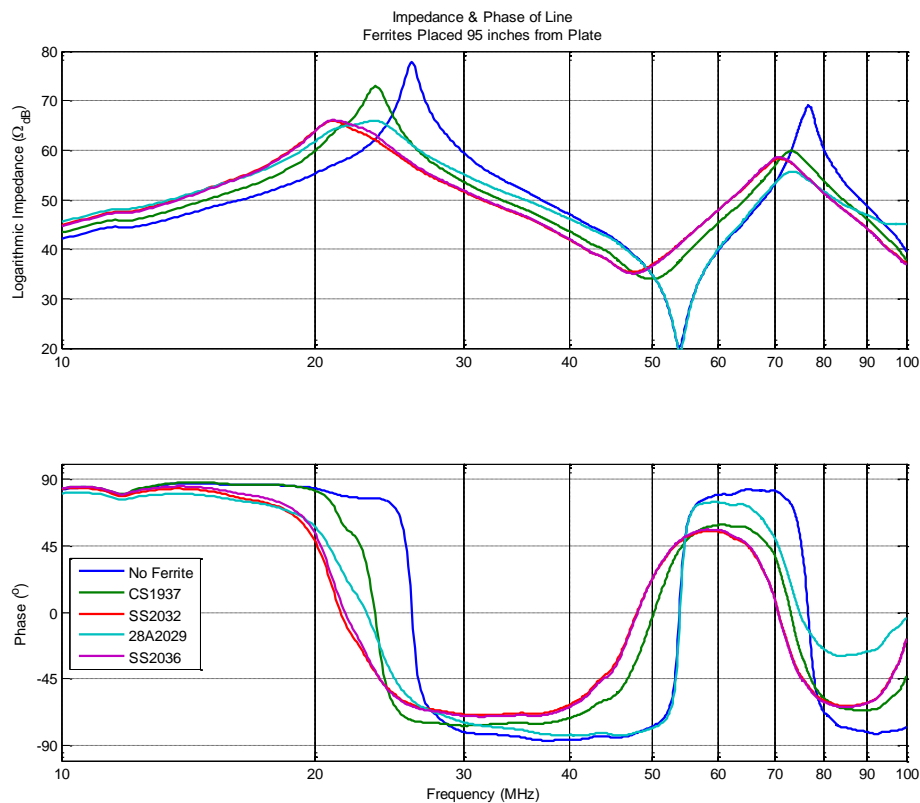


Figure 49 - Effects of Ferrites 95 inches from Plate

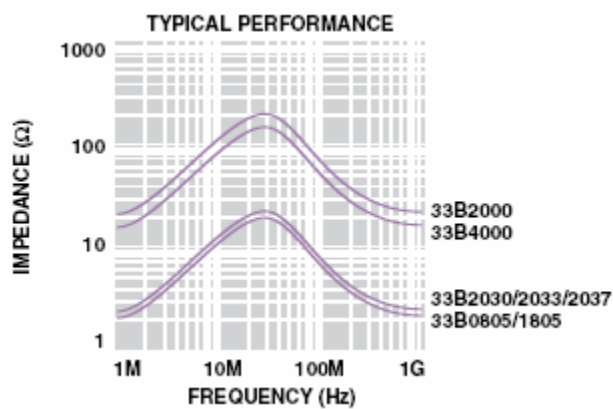


Figure 50 - CS33 Series Ferrishield Ferrite Impedance Characteristics

As can be seen by the input impedance plots, ferrites can help reduce common mode current because they increase the impedance over a frequency range. For this reason, it is

important to look at the data sheets similar to Fig. 50 before using ferrites. Ferrites are the most effective when they add impedance to frequencies where the input impedance of the motor and cables are low. Wherever the ferrites increase the impedance of the line, they will reduce the emissions as well as Figures 41-45 show. These figures illustrate only a small decrease in common mode current, and this can be explained by the fact that the ferrite used does not add much impedance. Referring to Fig. 50, at its peak value the CS33B2000 ferrite only adds 200Ω which is small compared to the peak impedances which are above $1k\Omega$.

To better evaluate possible EMI mitigation strategies, a model for the motor and cables was developed. To model the motor, the IEEE paper, “Efficient HF Modeling and Model Parameterization of Induction Machines for Time and Frequency Domain Simulations” was referenced. This paper outlines a method for the creation of a high frequency model for an induction motor. A complete model for the induction motor was generated from the data from two types of impedance measurements: common-mode and differential-mode. Pictures showing the setup for both the common-mode and differential-mode measurements are shown in Figures 51-55.



Figure 51 - Common Mode Setup: Full View A

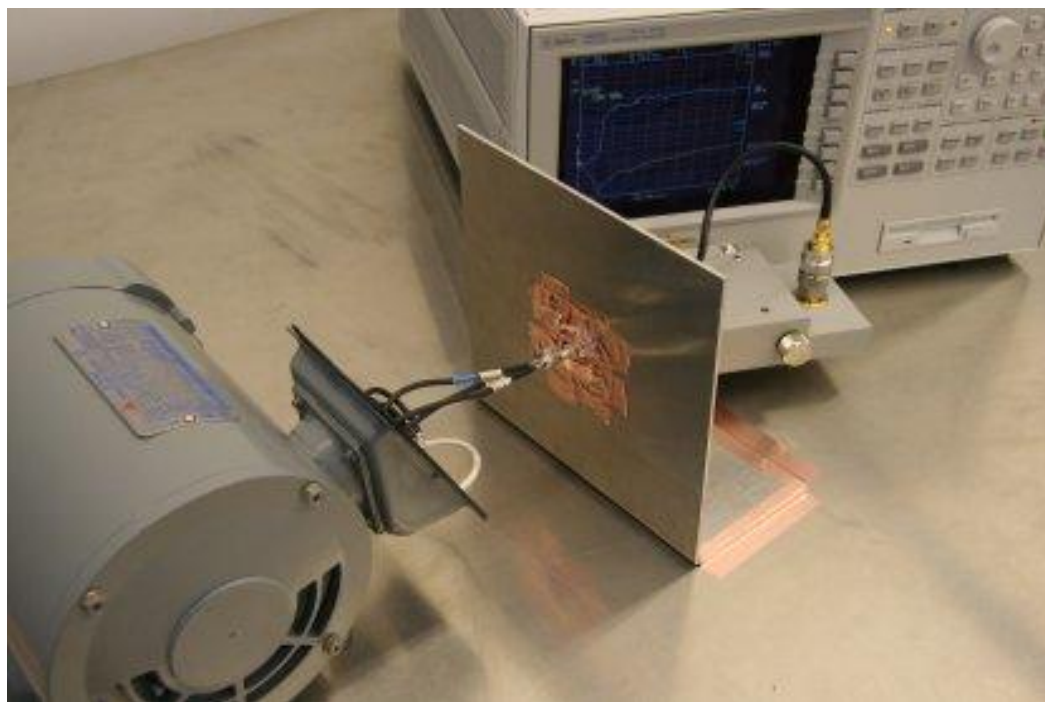


Figure 52 - Common Mode Setup: Full View B

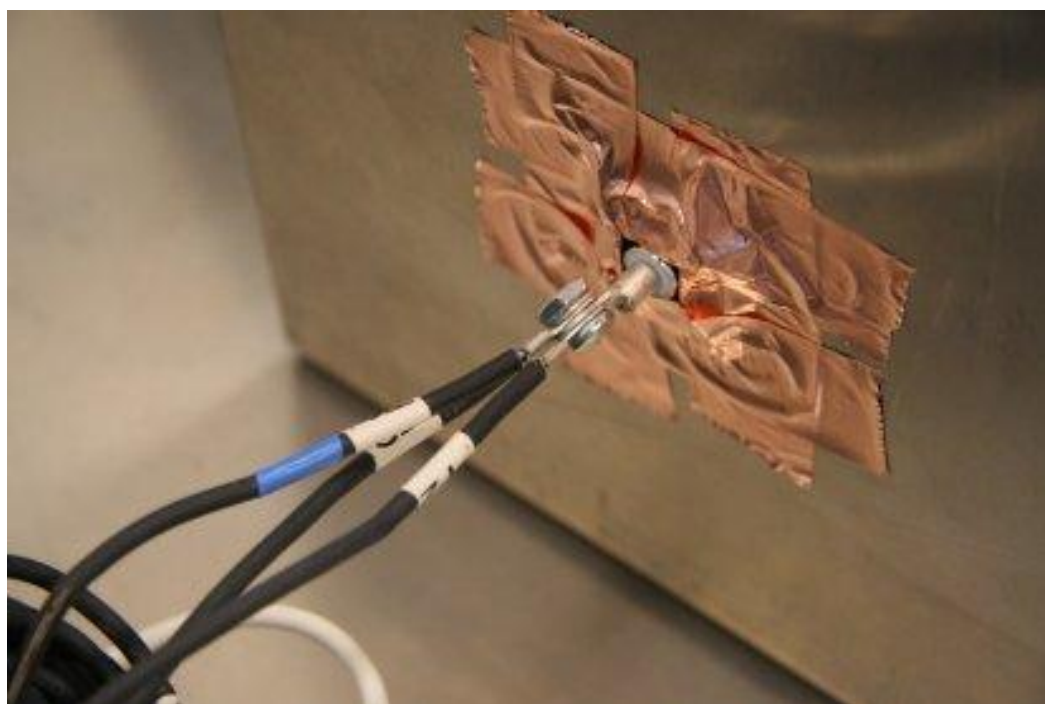


Figure 53 - Common Mode Setup: Common Mode Connection

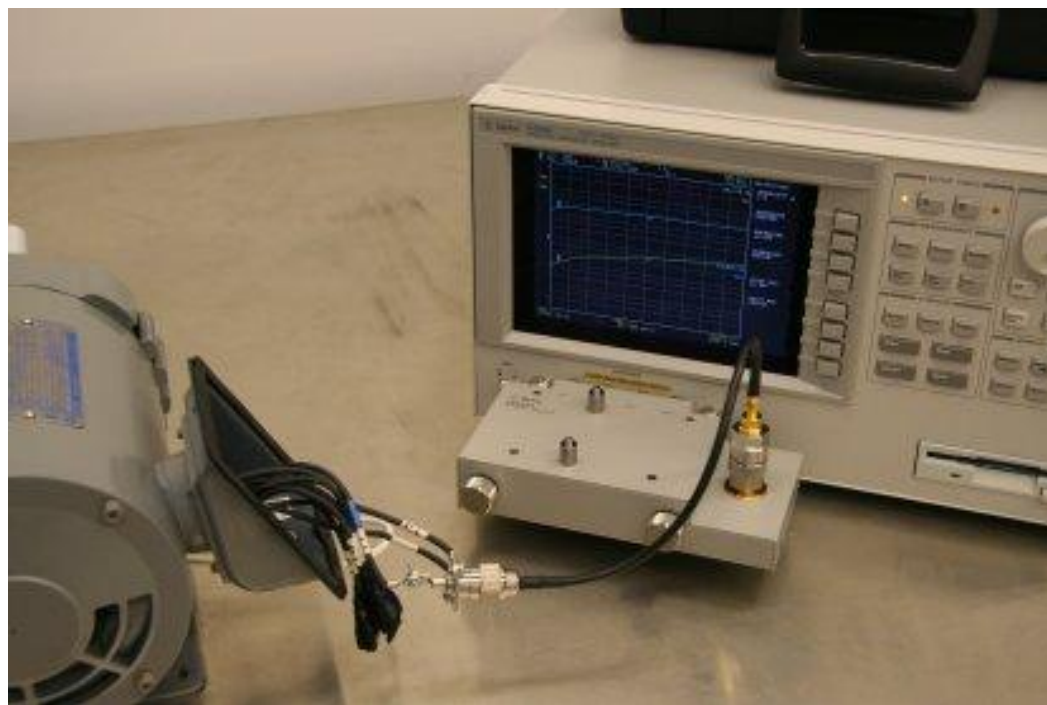


Figure 54 - Differential Mode Setup: Full View



Figure 55 - Differential Mode Setup: Differential Mode Connection

The impedance measurements for each setup are shown in Figures 56-57.

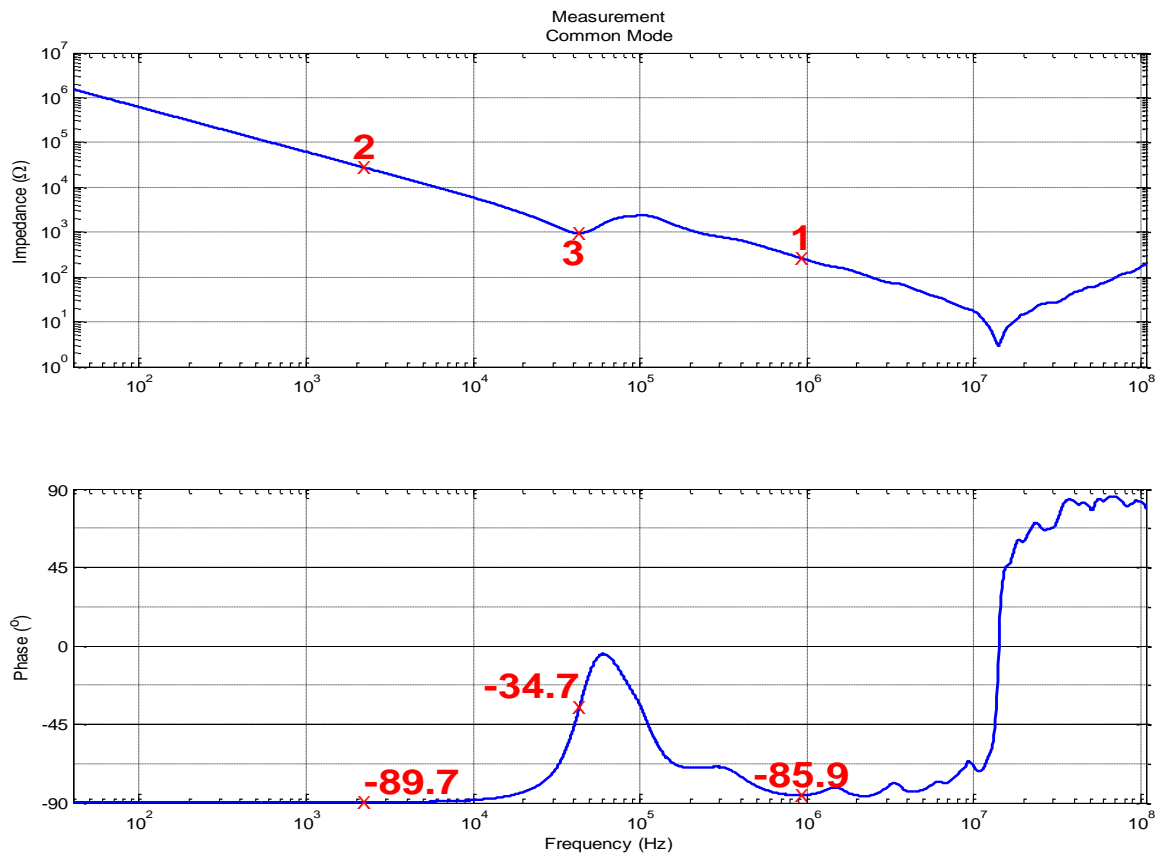


Figure 56 - Common Mode Measurement: Impedance and Phase

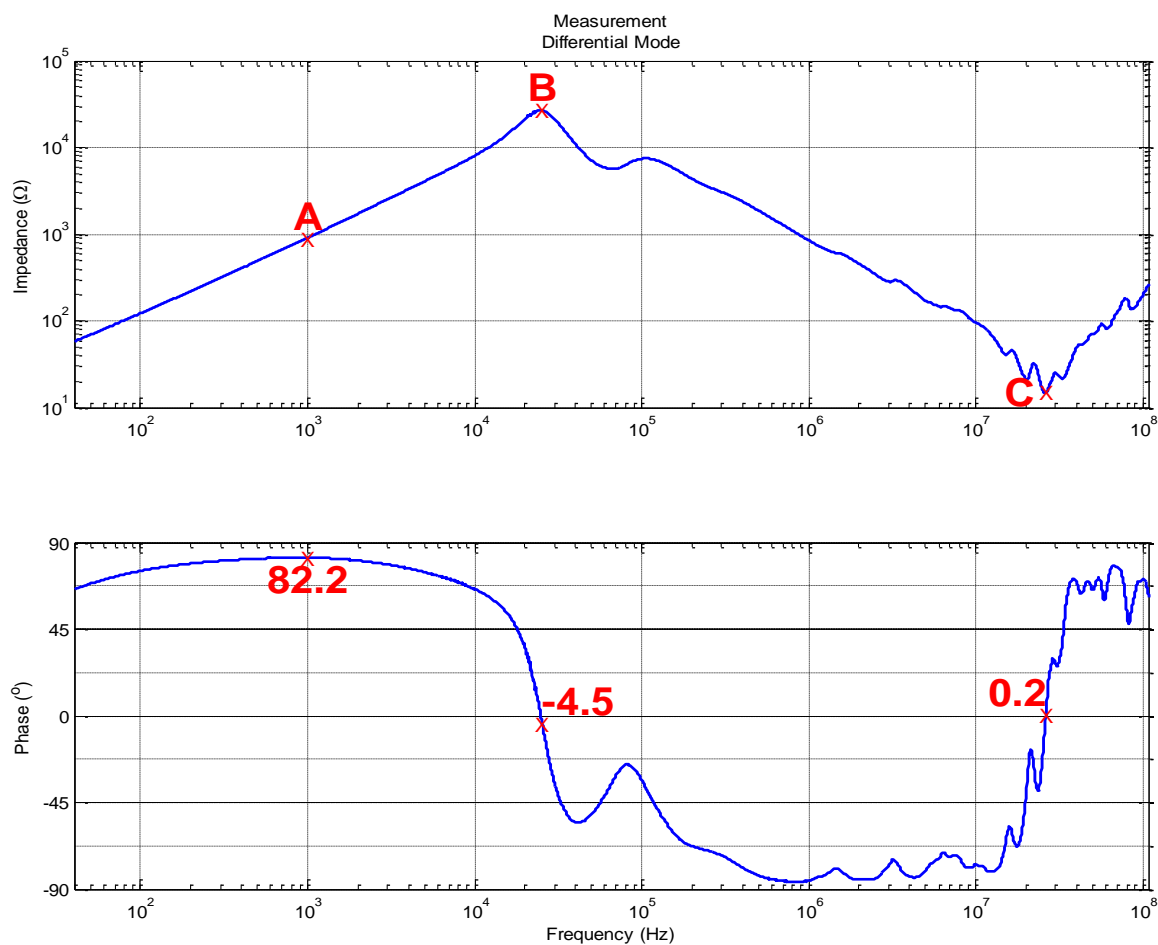


Figure 57 - Differential Mode Measurement: Impedance and Phase

As instructed by the paper, data points from both sets of measurements are used to calculate component values for the motor model. Using the formulas given in the paper, motor model as shown in Fig. 58, was created.

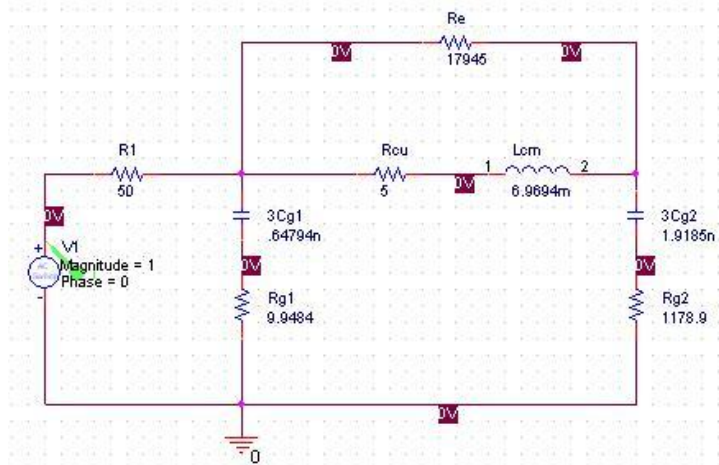


Figure 58 - Common Mode Motor Model

Next, the unshielded and shielded cables were modeled using a time-domain reflectometer (TDR). Using the setups shown in Fig. 23 and Fig. 26 for the unshielded and shielded cables, respectively, a TDR was connected to the aluminum plate. For the unshielded cable, a ground wire was not used. A screen capture of the TDR and the 50Ω test cable is shown in the Fig. 59. A screen capture of the TDR connected to the unshielded motor and cables is shown in Fig. 60. A screen capture of the TDR connected to the shielded motor and cables is shown in Figures 61-62.

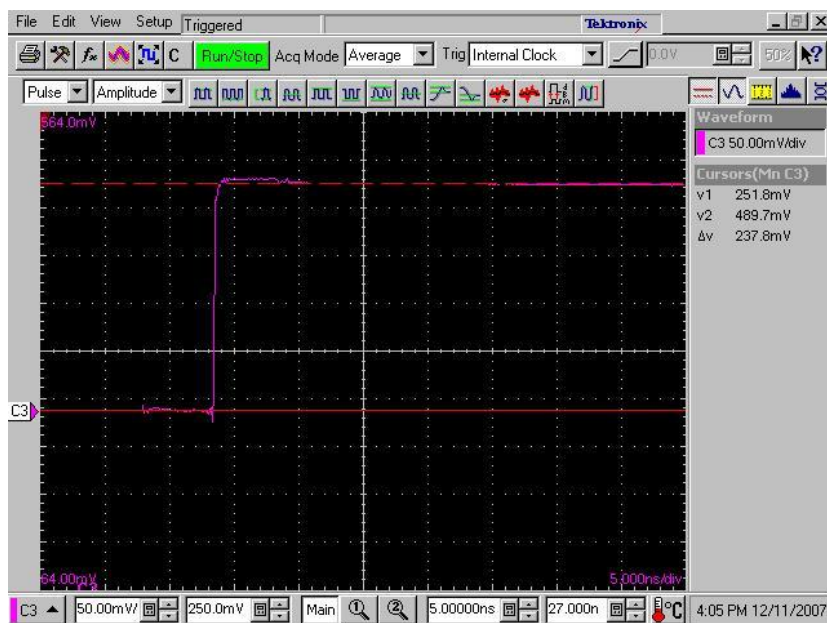


Figure 59 - TDR Measurement of the Test Plate and Test Cable

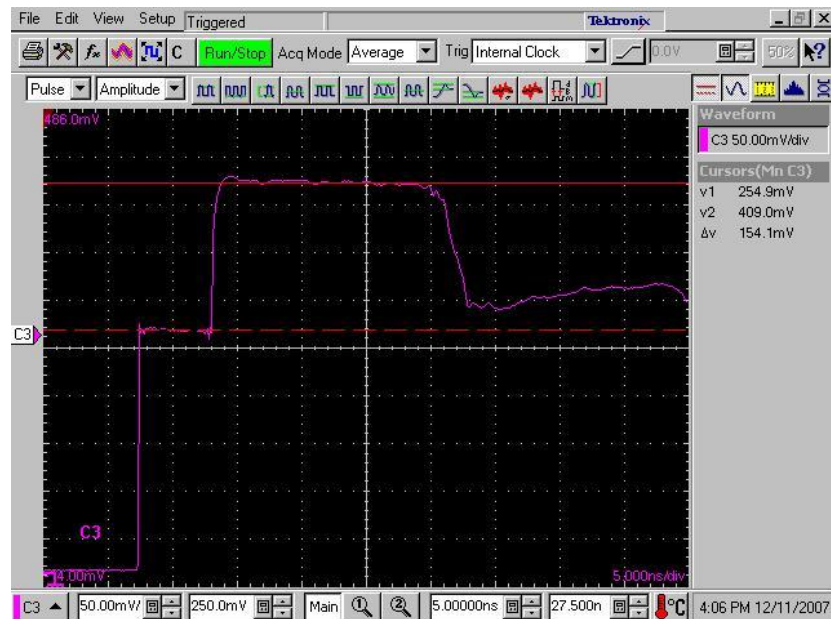


Figure 60 - TDR Measurement of the Motor and Cables

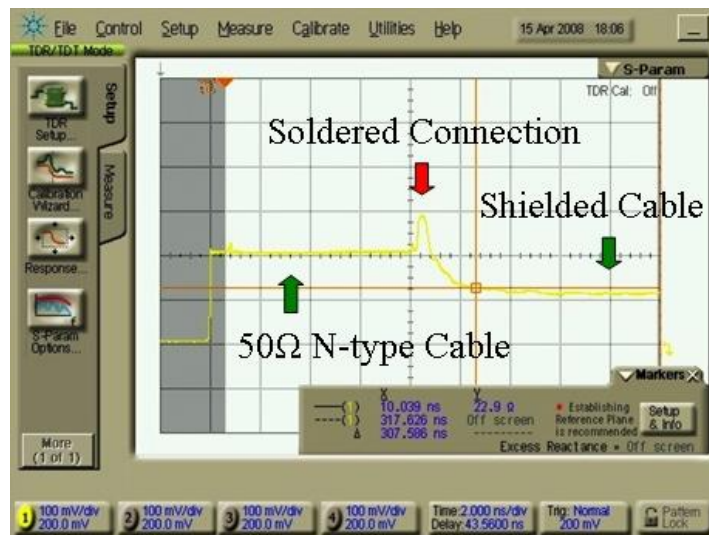


Figure 61 - Shielded Cable TDR Measurement

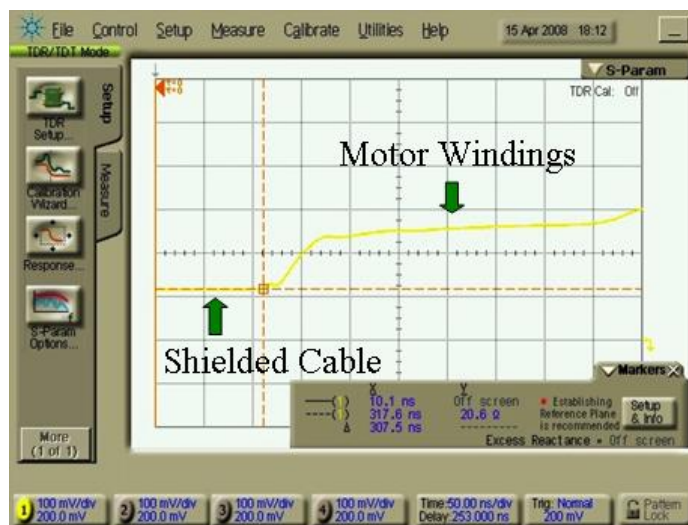


Figure 62 - Shielded Cable TDR Measurement

Using these screen captures the RHIT team approximated the characteristic impedance of the unshielded line to be 234Ω . With some theory, assuming that all three phase wires acted as one conductor over a return plane, the characteristic impedance was calculated as 263Ω . This results in a percent error of about 12% which is acceptable for the given assumptions in the calculation. In the same experiment as Missouri S&T, the characteristic impedance shown by the TDR was approximately 250Ω . Using the same theory, the theoretical value for the characteristic impedance was found to be 274Ω , approximately resulting in a 10% error. The difference in measurement results can be attributed to variations in the test setup, instrumentation, and the instrument calibration. A summary of the test results found by Missouri S&T are given below in Table 7.

Table 7 – Summary of TDR Results

Cable Type	Z_0 (Ω)	TD (ns)	Cable Length (ft)
Shielded	19.5	153.793	99.5
Unshielded	250	8.841	8.35

The TDR was also used in calculating the relative permittivity of the surrounding non-homogenous media which mostly consists of air and the insulation foam. The screen

capture in Fig. 63 shows a closer view of the reflected waves on the motor and cable setup during the test. The dip in the voltage at the far right of the scope represents a ferrous bar placed on the line. The two vertical red lines represent the N-type bulkhead mount and the ferrous bar. With the markers the amount of time for a wave to travel (time delay) on the line from the plate to the bar is known. By knowing the length of the line we can calculate the velocity of propagation and then the relative permittivity. For this method of calculation, the relative permittivity was found to be about 1.03 and supports initial suspicions that it would be close to 1 because most of the surrounding media is air as well as the insulation foam material used to support the cables is comprised mostly of air.

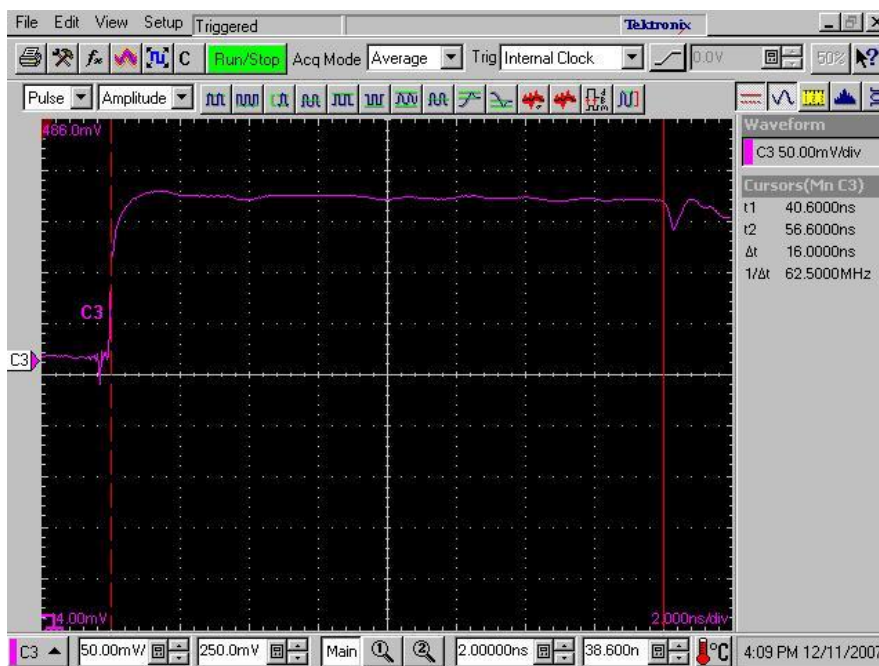


Figure 63 - TDR Measurements for Permittivity Calculation

Although the TDR can be used to calculate the relative permittivity of the surrounding environment, it is not necessarily the most accurate. Because there can be some ambiguity as to the starting and ending points of the cables on the TDR, the time delay can be thrown off by fractions of a nanosecond causing significant errors in the relative permittivity calculation. Another way to calculate this parameter is by performing a

resonance analysis of the input impedance of the motor and cables from Fig. 33. In transmission line theory, it is known that one of the resonant points represents the frequency in which the transmission line is one quarter wavelength long. Assuming the wave velocity was approximately equal to the speed of light in air and calculating the quarter wavelength for a few resonant frequencies, it was found that the second resonant point located at 26.3 MHz was most nearly the frequency that made the cables a quarter wavelength long. Assuming the environment acted as a loss-less dielectric and from knowing the fact that the wavelength of a wave in a loss-less dielectric is equal to the free space wavelength over the square root of the relative permeability and permittivity, the relative permittivity was calculated. The result of this calculation showed the relative permittivity as 1.25.

Given the transmission line model parameters in Table 7 and the motor model in Fig. 58, both sets of information were combined to form a motor and cable model. The unshielded common mode motor and cable model is shown in Fig. 64. The shielded motor and cable model is similar to the unshielded model, except the time delay and characteristic impedance of the transmission line are different.

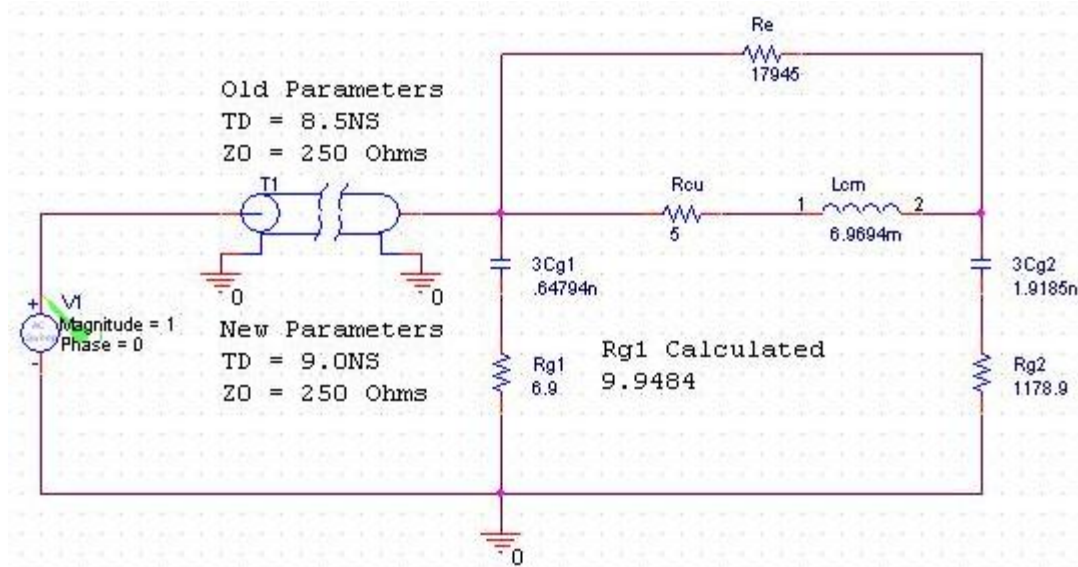


Figure 64 - PSpice Model of Motor and Cable

Using the common mode motor and cable model the measured impedance was compared to the simulated impedance for both the unshielded and shielded models. The results are in Figures 65-66.

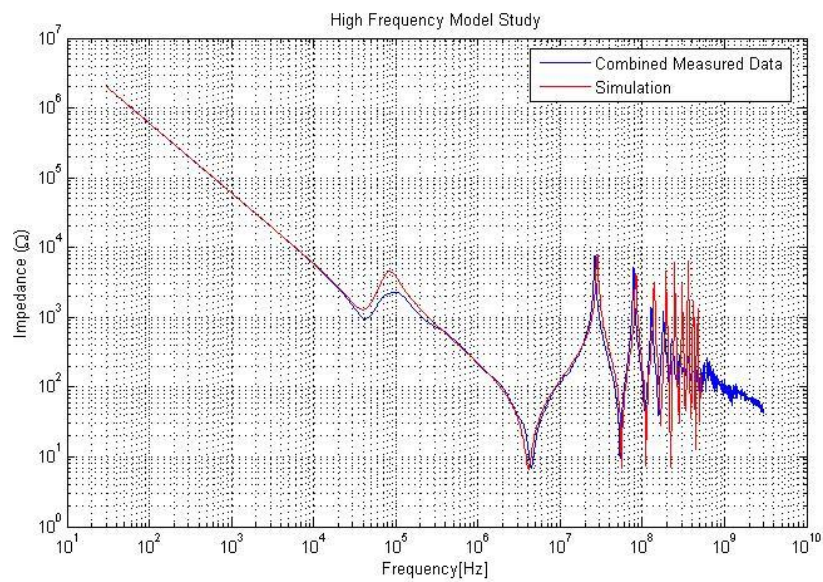


Figure 65 - Comparison of Unshielded Motor and Cables Input Impedance

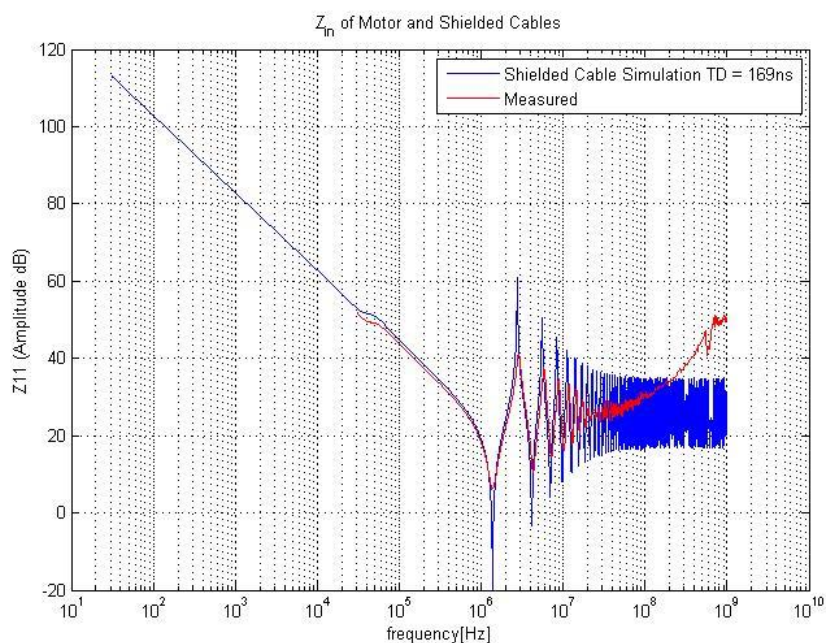


Figure 66 - Comparison of Shielded Motor and Cables Input Impedance

Deliverables

- A PSPICE model of the EMI coupling paths in the PowerFlex70 together with
 - Computer simulations
 - Laboratory measurements
- A technical report including
 - Documentation and demonstration of EMC model creation
 - Documentation and demonstration of developing computer simulations
 - Documentation and demonstration of laboratory measurements
 - Potential EMI mitigation techniques

Recommendations

IGBT Module

In the next few weeks, the teams will work to finalize the parasitic model and hand this portion of the project over to the client. At this point we will discuss with the client future improvements upon both the design of similar IGBT modules, as well as EMC modeling practices and mitigation techniques.

The results of this investigation will significantly aid the client in preventing EMC problems in the future. A starting example is that identical phase legs should have very similar geometry. Because each of the phase legs is to perform the same duty, the impedance should be the same, which directly correlates to its geometry. Next, noisy currents need to have their return paths very close as to cancel out the magnetic field.

Motor and Cables

After modeling the setup and analyzing the collected data we have formulated several ideas for mitigating emissions. In the case of unshielded cable, a simple remedy is to attach a ferrite to the cable closest to the motor drive. The ferrites should have the highest spectral impedance near the proper frequency. Multiple ferrites can be paired in series if necessary for multiple frequencies. If it is possible, the best option is to use a shielded cable since it significantly reduces emissions. Shielding is known to mitigate electric

fields by displacing charge on the conductor induced by the field. A simple method for reducing differential mode conductive emissions is to twist the wires together. This works under the assumption that the returning signal is out of phase with the departing signal and they cancel each other.

For groups looking to further investigate this project, we believe the current model is sufficient for simulation purposes and does not warrant further refinement. However, there is much unexplored research on mitigation techniques. We recommend that future groups investigate research and develop efficient, cost effective solutions.

Conclusion

EMC modeling is essential for government compliance and robust design. Engineers can utilize models and augmented schematics to design device layout and geometry in order to minimize EMI. As an example, we have modeled an AC motor drive. An EMC model including parasitic capacitances and inductances for an IGBT package has been developed and validated with simulation and laboratory measurements. In addition a high frequency model for the motor and a transmission line model for the cables has also been developed and verified. If used correctly, these models of a Rockwell Automation AC motor drive and the processes used to generate them will give Rockwell Automation engineers the necessary tools to solve future EMI problems in their products.

Appendix A: References

[1] Allen-Bradley, "Drives," [Online document], 2007 Aug 1, [cited 2007 Aug 1], Available HTTP: <http://www.ab.com/drives/>

Rockwell Automation's Allen-Bradley product line of motor drives is described here in detail. Applications, specifications, as well as product support and literature is included on this website.

[2] FCC Part 15, Radio Frequency Devices.

This dictates the FCC regulations on electronic devices and emission levels. It breaks devices into categories, discusses types of emissions, as well as where the device will operate. It goes into great detail on the size, power level, and measurement techniques of various electronic devices.

[3] IEC CISPR, Electromagnetic Compatibility: Including Radio Interference.

The International Engineering Consortium requirements for the radiation emissions for electronic devices to be used internationally are included in the body of this report. In addition, immunity and other aspects to EMC are included in this document.

[4] Mohan, Undeland, and Robbins, Power Electronics: Converters, Applications and Design, New York Wiley, 1989.

This article details the basics of IGBTs and how they are applicable to power systems as a semiconductor package. In addition, it discusses the functioning of the device assuming a previous knowledge of MOSFETs and BJTs.

[5] Paul, Clayton R., Introduction to Electromagnetic Compatibility, 2d ed. New Jersey: John Wiley & Sons, 2006, pp. 50-58, 377-557.

Dr. Clayton Paul is an expert in electromagnetic interference and compatibility. He is the 2005 IEEE Electromagnetics Award winner. This book provides a supreme reference for EMC situations and problems, and provides background information for a complete understanding of the fundamentals.

[6] "Rose-Hulman Institute of Technology," [Online document], 2007 Aug 1, [cited 2007 Aug 2], Available HTTP: <http://www.rose-hulman.edu/>

Rose-Hulman Institute of Technology is a private, engineering school in Terre Haute, IN. Their website includes information on its students, programs, faculty, etc.

[7] "The University of Missouri-Rolla Electromagnetic Compatibility Consortium," [Online document], 2007 Aug 1, [cited 2007 Aug 1], Available HTTP: <http://www.emclab.umr.edu/>

The University of Missouri-Rolla's Electrical and Computer Engineering Departments electromagnetic compatibility group has their work, purpose, and contacts listed on this page.

[8] Wheeler, Ed. "Instructional Materials on Electromagnetic Compatibility, Signal Integrity, and High Speed Design," NSF Grant 0618494, 9/2006-8/2010.

This NSF Proposal discusses how Drs. Wheeler and Drewniak, et. al. are attempting to improve the understanding of electromagnetism at an undergraduate, graduate, and industrial level.

BIBLIOGRAPHY

- [1] D. M. Pozar, *Microwave Engineering*, Ch. 2, 4, John Wiley & Sons Inc., – 3rd edition.
- [2] Paul, Clayton R., *Introduction to Electromagnetic Compatibility*, 2d ed. New Jersey: John Wiley & Sons, 2006, pp. 50-58, 377-557.
- [3] "The University of Missouri-Rolla Electromagnetic Compatibility Consortium," [Online document], 2007 Aug 1, [cited 2007 Aug 1], Available HTTP: <http://www.emclab.umn.edu/>
- [4] <http://www.sce.carleton.ca/faculty/chinneck/thesis.html>. Organizing Your Thesis, June 2004 (date mentioned here is the date on which the website was last visited).

VITA

Clint Matthew Patton was born in Sedalia, MO on February 14, 1984. He completed his general education at State Fair Community College in Sedalia, MO, from August 2002 to May 2004. In August 2004, he transferred to the University of Missouri in Rolla, MO where he completed his Bachelor of Science Degree in Electrical Engineering in May 2007. He started working with the University of Missouri-Rolla Electromagnetic Compatibility Laboratory in August 2006 performing undergraduate research dealing with constructing antennas for measuring the shielding effectiveness of a system. May 2007 he joined the EMC Laboratory at Missouri University of Science and Technology in Rolla, MO, and started his Master of Science Degree in Electrical Engineering with an emphasis in Electromagnetic Compatibility. August 2009 he attained his Master of Science Degree and took a position with BAE Systems in Nashua, New Hampshire, as an EMC Engineer. The research completed gave him an understanding of how to model and extract parasitic elements that influence a circuit. He achieved a deep understanding of full-wave modeling tools and learned how they worked along with their limitations. For the later part his time with the EMC Laboratory, he explored factors which play a role in the performance of devices that impose strong magnetic fields into other systems.

